

UNIVERSITÉ DE MONTRÉAL

HIGH DATA-RATE, BATTERY-FREE, ACTIVE MILLIMETER-WAVE IDENTIFICATION
TECHNOLOGIES FOR FUTURE INTEGRATED SENSING, TRACKING, AND
COMMUNICATING SYSTEMS-ON-CHIP

PASCAL BURASA
DÉPARTEMENT DE GÉNIE ÉLECTRIQUE
ÉCOLE POLYTECHNIQUE DE MONTRÉAL

THÈSE PRÉSENTÉE EN VUE DE L'OBTENTION
DU DIPLÔME DE PHILOSOPHIAE DOCTOR
(GÉNIE ÉLECTRIQUE)
DÉCEMBRE 2016

UNIVERSITÉ DE MONTRÉAL

ÉCOLE POLYTECHNIQUE DE MONTRÉAL

Cette thèse intitulée:

HIGH DATA-RATE, BATTERY-FREE, ACTIVE MILLIMETER-WAVE IDENTIFICATION
TECHNOLOGIES FOR FUTURE INTEGRATED SENSING, TRACKING, AND
COMMUNICATING SYSTEMS-ON-CHIP

présentée par : BURASA Pascal

en vue de l'obtention du diplôme de : Philosophiae Doctor

a été dûment acceptée par le jury d'examen constitué de :

M. LAURIN Jean-Jacques, Ph.D., président

M. WU Ke, Ph.D., membre et directeur de recherche

M. CONSTANTIN Nicolas, Ph.D., membre et codirecteur de recherche

M. FRIGON Jean-François, Ph.D., membre

M. NABKI Frédéric, Ph.D., membre externe

DEDICATION

To my parents, my sisters, my brothers, my aunts, my uncles, my cousins, and all my loved ones

“It is much more humbling to imagine this little step shining your faces and giving you a smile”

ACKNOWLEDGEMENTS

First and foremost, I would like to take this opportunity to express my utmost gratitude to my supervisor, Professor Ke Wu, for having given me the opportunity to join his research team. I am deeply indebted to him for his inspiring guidance, patience, and support throughout my Ph.D. studies.

I would like to extend my thanks to my thesis co-supervisor Professor Nicolas Constantin, for his help and encouragement during the long years that I have spent working on my dissertation.

I would also like to thank the members of my thesis jury, Professor Jean-Jacques Laurin, Professor Jean-François Frigon, and Professor Frédéric Nabki, for having accepted to examine this work, for the time and effort they have put forth, and for their valuable comments.

A special thanks goes to Professor Tarek Djerafi, for his willingness to help and for the contribution he made on this work.

To my Poly-Grames Research Center colleagues at the Ecole Polytechnique de Montreal, the list will be too long, thank you for creating a pleasant and stimulating environment for research.

I would like to thank all technical staffs of the Poly-Grames Research Center, Mr. Jules Gauthier, Mr. Jean-Sebastien Décarie, Mr. Traian Antonescu, Mr. Steve Dubé, and Mr. Maxime Thibault, for their professional assistance in the fabrication and the measurements. Thank you Mme. Rachel Lortie, our Poly-Grames Research Center secretary, for your enthusiastic service.

The technical support, design tools, and chip fabrication from CMC Microsystems, Kingston, ON, Canada, is gratefully acknowledged.

RÉSUMÉ

Pour de nombreuses applications allant de la sécurité, le contrôle d'accès, la surveillance et la gestion de la chaîne d'approvisionnement aux applications biomédicales et d'imagerie parmi tant d'autres, l'identification par radiofréquence (RFID) a énormément influencé notre quotidien. Jusqu'à présent, cette technologie émergente a été la plupart du temps conçue et développée dans les basses fréquences (en dessous de 3 GHz). D'une part, pour des applications où de courtes distances (quelques centimètres) et à faible taux de communications de données sont suffisantes (même préférables dans certains cas), la technologie RFID à couplage inductif qui fonctionne à basse fréquences (LF) ou à haute fréquences (HF) fonctionne très bien et elle est largement utilisée dans de nombreuses applications commerciales. D'autre part, afin d'augmenter la distance de communication (quelques mètres), le débit de données de communication, et ainsi minimiser la taille du tag, la technologie RFID fonctionnant dans la bande d'ultra-haute fréquence (UHF) et aux fréquences micro-ondes (par exemple, 2.4 GHz) a récemment attiré beaucoup d'attention dans le milieu de la recherche et le développement. Cependant, dans ces bandes de fréquences, une bande passante disponible restreinte avec la taille du tag assez large (principalement dominée par la taille d'antenne et de la batterie dans le cas d'un tag actif) sont les principaux facteurs qui ont toujours limité l'évolution de la technologie RFID actuelle. En effet, propulser la technologie RFID dans la bande de fréquences à ondes millimétriques briserait les barrières actuelles de la technologie RFID.

La technologie d'identification aux fréquences à ondes millimétriques (MMID) offre plus de bande passante, et permet également la miniaturisation de la taille du tag, car à ces bandes de fréquences, la longueur d'onde est de l'ordre de quelques millimètres, une taille comparable à la taille d'un circuit intégré. L'antenne peut donc être soit intégrée sur la même puce (antenne sur puce) ou soit encapsulée dans le même boîtier que le circuit intégré. En dotant le tag la capacité de récolter sans fil son énergie à partir d'un signal aux fréquences à ondes millimétriques provenant du lecteur, lui fournissant ainsi l'autonomie énergétique (ainsi éliminant la nécessité d'une batterie et en même temps permettant la miniaturisation du tag), il devient alors possible d'intégrer entièrement tout le tag MMID sur une seule puce y compris les antennes, ce qui aboutira à la mise au point d'une nouvelle technologie miniature (μ RFID) fonctionnant à la bande de fréquences à ondes millimétriques. En outre, le concept d'identification aux fréquences à ondes millimétriques est

compatible avec des applications à venir de la technologie aux fréquences à ondes millimétriques dans le domaine de la communication sans fil tels que l'internet des objets "Internet of Things", la technologie 5G, etc.

Dans cette thèse, nous présentons et démontrons le concept d'identification aux fréquences à ondes millimétriques pour un système actif, mais sans batterie, entièrement intégré sur en utilisant le procédé de fabrication de circuits intégrés moins chère, standard, et commercial CMOS. La technologie MMID proposée dans cette thèse, représente la prochaine génération de la technologie RFID miniaturisée (μ RFID) opérant à des fréquences à ondes millimétriques. Les notions clés de la technologie RFID, le redresseur de l'énergie sans fil, les motivations, les contributions, et ainsi l'organisation de la thèse sont abordées aux chapitres 1 et 2. Le chapitre 3 présente l'étude et la démonstration expérimentale qui prouve que l'énergie RF peut être récoltée et efficacement convertie en énergie CC utilisable même aux fréquences à ondes millimétriques. Dans le chapitre 4, le concept d'un mélangeur auto-oscillant, approprié aux circuits intégrés à ultra-faible consommation de puissance (émetteurs-récepteurs auto-alimentés) est proposé et analytiquement et expérimentalement démontré aux fréquences à ondes millimétriques. Le chapitre 5 démontre un tag MMID miniature intégré sur un seul chip y compris les antennes intégrées dans le boîtier. Le tag est capable de recevoir sans fil (aux fréquences à ondes millimétriques) son énergie grâce au convertisseur intégré sur puce, d'alimenter son émetteur-récepteur intégré aussi sur puce, et d'échanger ses données avec le lecteur à un haut débit de communication. Le chapitre 6 aborde le concept d'antenne sur puce, un élément clé dans l'aboutissement et la mise en œuvre d'un tag MMID entièrement intégré sur puce. Une antenne à fente "slot antenna" double fréquences intégrée sur puce est proposée. Les résultats obtenus démontrent expérimentalement qu'une efficacité et un gain largement suffisants pour les applications MMID sont réalisables. Le chapitre 7 présente les applications potentielles du concept MMID proposé dans cette thèse. Enfin, une conclusion et les travaux futurs sont présentés au chapitre 8.

ABSTRACT

For countless applications ranging from security, access control, monitoring, and supply chain management to biomedical and imaging applications among many others, radio frequency identification (RFID) technology has tremendously impacted our daily life. So far, this ever-needed and emerging technology has been mostly designed and developed at low RF frequencies (below 3-GHz). For many practical applications where short-range (few centimeters) and low data-rate communications are sufficient and in some cases even preferable, inductively coupled RFID systems that operate over either low-frequency (LF) or high-frequency (HF) bands have performed quite well and have been widely used for practical and commercial applications. On the other hand, in the quest for a longer communication range (few meters), relatively high data-rate and smaller antenna size RFID systems operating over ultra-high frequency (UHF) and microwave frequency bands (e.g., 2.4-GHz) have recently attracted much attention in the research and development community. However, over these RF bands, a restricted available bandwidth together with an undesired tag size (mainly dominated by its off-chip antenna size and battery in the case of active tag) are the main factors that have been limiting the evolution of today's RFID technology. Indeed, propelling RFID technology into millimeter-wave frequencies opens up new applications that cannot be made possible today.

Millimeter-wave identification (MMID) technology is set out to exploit significantly larger bandwidth and smaller antenna size. Over these frequency bands, an effective wavelength is in the order of a few millimeters, hence close to a typical semiconductor (CMOS) die size. The antenna, therefore, may either be integrated on the same chip (antenna-on-chip – AoC) or embedded in the related package (antenna-in-package – AiP). In addition, by equipping the tag with the capability to wirelessly harvest its energy from an incoming millimeter-wave signal, thereby providing energy autonomy without the need of a battery and at the same time allowing miniaturization, it becomes possible to integrate the entire MMID tag circuitry on a single chip. Furthermore, the timely MMID concept is fully compatible with upcoming and future applications of millimeter-wave technology in wireless communications which are being discussed and developed worldwide in research and development communities, such as the internet of things (IoT), 5G, autonomous mobility, μ Smart sensors, automotive RADAR technologies, etc.

This thesis introduces and demonstrates a high data-rate, battery-free, yet active MMID concept, fully implemented on a single CMOS-die (an all-in-one solution using a commercial standard CMOS process). The proposed MMID system represents the next generation of μ RFID technology that operates at mm-wave frequencies. Key notions of RFID technology and wireless power harvesting, the motivation, the contributions and the thesis organization are discussed in Chapter 1 and 2. Chapter 3 presents the study and experimental demonstration that RF energy can still be harvested and efficiently converted into DC power even at mm-wave frequencies. In Chapter 4, a zero-IF self-oscillating mixer concept, applied as an ultra-low-power transceiver suitable for self-powered devices, is proposed and demonstrated at mm-wave frequencies. In Chapter 5, the antenna-in-package concept is exploited, and it demonstrates the realization of a miniature high data-rate MMID tag on a single-chip. The MMID tag harvests its energy from the reader (i.e. it is entirely supplied by the on-chip mm-wave/DC energy converter) and exchanges data at a high bit-rate for both communication links. Chapter 6 addresses the antenna on-chip concept, a key circuit block that renders possible the full implementation of the MMID tag (i.e. including the antenna) on a single CMOS-die. An on-chip, dual-frequency rectangular slot antenna with a DRA loading is proposed and studied, and it is experimentally demonstrated that sufficient radiation efficiency and antenna gain for both bands are achievable. Chapter 7 discusses potential applications of the proposed MMID concept in this thesis. Finally, a conclusion and future works are presented in Chapter 8.

TABLE OF CONTENTS

DEDICATION	III
ACKNOWLEDGEMENTS	IV
RÉSUMÉ.....	V
ABSTRACT	VII
TABLE OF CONTENTS	IX
LIST OF TABLES	XII
LIST OF FIGURES.....	XIII
LIST OF SYMBOLS AND ABBREVIATIONS.....	XVIII
LIST OF APPENDICES	XX
CHAPTER 1 INTRODUCTION.....	1
1.1 Motivation and Objectives	2
1.2 Contribution and Organization of the Thesis	3
CHAPTER 2 LITERATURE REVIEW	6
2.1 RFID Technology.....	6
2.1.1 Different types of RFID	7
2.1.2 RFID Operating Frequency Bands	13
2.1.3 RFID Tags Implemented Using CMOS Technology	14
2.2 Wireless Power Harvesting with CMOS-based Rectifier Circuits.....	16
2.2.1 Conventional Diode-Connected Transistor	16
2.2.2 Power-Matching and Voltage Gain-Boosting Network	17
2.2.3 External Threshold Voltage Cancellation	18
2.2.4 Zero-Threshold Voltage Transistors (native transistors)	19

2.2.5	Cross-Coupled Differential-Drive Topology	20
2.3	Millimeter-Wave Identification (MMID) Technology	21
2.3.1	Chipless MMID tag.....	21
2.3.2	MMID tag with integrated chip.....	22
CHAPTER 3	ARTICLE 1: HIGH-EFFICIENCY WIDEBAND RECTIFIER FOR SINGLE-CHIP BATTERYLESS ACTIVE MILLIMETER-WAVE IDENTIFICATION (MMID) TAG IN 65-NM BULK CMOS TECHNOLOGY	23
3.1	Introduction	24
3.2	Proposed MMID System with Batteryless Tag.....	25
3.3	Millimeter-Wave-to-DC Rectifier.....	27
3.4	Design and Measurement Results	31
3.4.1	Chip Design and Measurement Setup	31
3.4.2	Millimeter-Wave-to-DC Rectifier Performances.....	32
3.5	Conclusion.....	38
CHAPTER 4	ARTICLE 2: LOW-POWER INJECTION-LOCKED ZERO-IF SELF-OSCILLATING MIXER FOR HIGH GBIT/S DATA-RATE BATTERY-FREE ACTIVE μ Rfid TAG AT MILLIMETER-WAVE FREQUENCIES IN 65-NM CMOS	39
4.1	Introduction	40
4.2	Operating Principles of the Proposed Zero-IF SOM Circuit.....	42
4.3	Analytical Expressions for Zero-IF SOM Operation	44
4.3.1	Conversion Gain of SOM: Reader-to-Tag Communication	46
4.3.2	Up-Converted Sideband Power of SOM: Tag-to-Reader Communication.....	56
4.4	Circuit Design and Experimental Results	58
4.4.1	Chip Design and Measurement Setup	58
4.4.2	Zero-IF SOM Performances.....	60

4.5	Conclusion.....	67
CHAPTER 5 ARTICLE 3: HIGH-DATA-RATE SINGLE-CHIP BATTERY-FREE ACTIVE MILLIMETER-WAVE IDENTIFICATION TAG IN 65-NM CMOS TECHNOLOGY		
		68
5.1	Introduction	70
5.2	Proposed MMID system with battery-free active tag on single-chip.....	72
5.3	Self-powered zero-IF self-oscillating mixer circuit	73
5.4	A small footprint high-gain 24-GHz differential and 40-GHz dual-polarized antenna ..	79
5.5	Measurement setup and experimental results.....	83
5.6	Conclusion.....	92
CHAPTER 6 ARTICLE 4: ON-CHIP DUAL-BAND RECTANGULAR SLOT ANTENNA FOR SINGLE-DIE MILLIMETER-WAVE IDENTIFICATION TAG IN STANDARD CMOS TECHNOLOGY		
		93
6.1	Introduction	95
6.2	Antenna Design Considerations	98
6.2.1	Slot Antenna.....	99
6.2.2	Dual-Frequency Co-centered Slot Antenna	104
6.3	DRA-Loaded, Dual-Frequency, Co-centered Slot Antenna.....	107
6.4	Antenna Measurements	111
6.5	Conclusion.....	116
CHAPTER 7 GENERAL DISCUSSION.....		
		117
CHAPTER 8 CONCLUSION AND FUTURE WORKS		
		120
8.1	Conclusion.....	120
8.2	Future works.....	122
REFERENCES.....		
		124

LIST OF TABLES

Table 2.1: Performance summary of UHF/microwave passive RFID tags in CMOS technology.	15
Table 2.2: Performance summary of CMOS rectifiers using different rectification techniques....	21
Table 3.1: Possible link budget and dc operation condition of the proposed MMID tag.	37
Table 4.1: Performance summary and comparison of SOMs.	66
Table 5.1: Performance summary and comparison of millimeter-wave identification (MMID) tags	91

LIST OF FIGURES

Figure 2.1: Illustration of an RFID system.	6
Figure 2.2: A general representation of a typical active RFID system.	7
Figure 2.3: A general representation of a typical passive RFID system.	8
Figure 2.4: Link power-budget for a typical passive RFID system [4].....	10
Figure 2.5: Realistic environment of a passive RFID system [4].	11
Figure 2.6: A general representation of a typical semi-passive RFID system.	12
Figure 2.7: RFID frequency bands [4].	13
Figure 2.8: Wireless power harvesting using a CMOS-based voltage multiplier [12].	16
Figure 2.9: Passive voltage-boosting network: (a) using an LC-resonator, (b) using a step-up transformer [13].....	17
Figure 2.10: Diode-connected transistor rectification mechanism: (a) without external bias, (b) with external bias [14].	18
Figure 2.11: I-V curve of a diode-connected transistor with/without external bias [15].	19
Figure 2.12: Circuit schematic of a cross-coupled differential-drive rectifier: (a) conventional topology [15], (b) improved topology [16].	20
Figure 3.1: Illustration of a reader-tag RFID system using backscattering.	24
Figure 3.2: Block diagram of the proposed MMID system with a batteryless active tag on single-chip.	26
Figure 3.3: Cross-coupled bridge configuration CMOS rectifier used in this paper. (a) Differential-drive circuit schematic, (b) Equivalent capacitor model.	27
Figure 3.4: Micrograph of the fabricated rectifier. (a) Narrow rectifier version, (b) De-embedding bloc, (c) Wider rectifier version.	31
Figure 3.5: Measured and simulated results at 24 GHz. (a) PCE versus P_{av} , (b) dc voltage versus P_{av}	33

Figure 3.6: Measured and simulated results at 35 GHz. (a) PCE versus P_{av} , (b) dc voltage versus P_{av} .	34
Figure 3.7: Measured and simulated results at 60 GHz. (a) PCE versus P_{av} , (b) dc voltage versus P_{av} .	35
Figure 3.8: Measured PCE results in connection with the transistor and capacitor sizing.	38
Figure 4.1: Block diagram of a recently proposed MMID system with a battery-free active tag on single-chip.	41
Figure 4.2: Operation principles of the proposed zero-IF SOM.	43
Figure 4.3: (a) Zero-IF SOM simplified model, (b) spectrum of the injected $RFinj$ signal during reader-to-tag communication, (c) spectrum of $RFinj$ signal during tag-to-reader communication.	44
Figure 4.4: Operating condition of cross-coupled pair transistors when biased close to their threshold voltage and their respective parasitic capacitors.	46
Figure 4.5: Zero-IF current and loading condition.	51
Figure 4.6: Simulated results that demonstrate the operating conditions of the SOM with and without $RFinj$ signal.	54
Figure 4.7: Simulated results of the recovered (down-converted) baseband signal at zero-IF output pad, when an AM signal, modulated by a random signal, is injected into the SOM.	55
Figure 4.8: Die microphotograph of the fabricated SOM.	58
Figure 4.9: (a) measurement setup, (b) photograph of measurement setup and the probe station.	59
Figure 4.10: SOM phase noise measured at $RFout$ pad for different power levels of the injected $RFinj$ signal.	60
Figure 4.11: (a) Spectrum of AM signal, modulated by a 10-kHz square wave signal, and injected into the SOM at $RFinj$ pad (Res BW 4.7 kHz, VBW 4.7 kHz), (b) recovered down-converted baseband signal measured at zero-IF pad.	61
Figure 4.12: Measured conversion loss versus injected power for different modulation index.	62

Figure 4.13: Measured and simulated conversion loss versus carrier-to-sideband power ratio of the injected RFinj signal.....	63
Figure 4.14: Measured and simulated conversion loss versus frequency of modulating signal $a(t)$	64
Figure 4.15: Spectrum of SOM measured at the RFout pad, when a 1-MHz sinus wave emulating the tag's data to be transmitted is injected into the SOM (Res BW 39 kHz, VBW 39 kHz). 64	
Figure 4.16: Power link-budget of the proposed MMID tag-reader system.	65
Figure 5.1: Illustration of the proposed battery-free active MMID tag in a single-chip with antenna-in-package: (a) top view, (b) exploded view.	69
Figure 5.2: Block diagram of the proposed millimeter-wave identification (MMID) system with a battery-free active tag on single-chip.	72
Figure 5.3: Circuit schematic of the power unit management, comprising of a mm-wave/dc rectifier and a low-power voltage regulator.	74
Figure 5.4: Circuit schematic of the proposed zero-IF self-oscillating mixer as an MMID tag transceiver.	76
Figure 5.5: Simulated results of the power unit management circuit (powering RF signal = 24 GHz @ 10 dBm): (a) start-up and regulated phases as a function of time, (b) rectified and regulated voltage ripples.	78
Figure 5.6: Proposed antenna: (a) U-folded coplanar folded dipole, (b) ring slot backed SIW cavity fed by GCPW.	79
Figure 5.7: Reflection coefficient $ S_{11} $ (dB) of the U-folded antenna and ring slot antenna and the isolation between two ring antennas in a perpendicular configuration. $L_a = 9.5$ mm, $L_b = 6.84$ mm, $L_f = 1.16$ mm, $R_s = 0.58$ mm, $R_c = 1.065$ mm, $W_s = 0.025$ mm.	81
Figure 5.8: Simulated radiation patterns: (a) U-folded dipole antenna, (b) ring slot backed SIW cavity.	82
Figure 5.9: The proposed MMID tag with the CMOS die microphotograph.	83
Figure 5.10: (a) Measurement setup, (b) photograph of the measurement setup.	84

Figure 5.11: Rectified and regulated voltages as a function of RF input power (RF powering signal = 24 GHz) measured at the output of the tag.	85
Figure 5.12: Measured spectrum from the tag: (a) when the tag is unlocked (free-running), (b) when the tag is injection-locked by the reader ($RFinj \approx -30$ dBm @ 40 GHz).	87
Figure 5.13: Measured phase noise from a free-running and an injection-locked ($RFinj \approx -30$ dBm @ 40 GHz) tag.	87
Figure 5.14: (a) Data sent to the tag by the reader @ 100 kbps, by modulating a 40 GHz carrier signal transmitted to the tag, (b) received and demodulated data measured at the output of the tag.	89
Figure 5.15: Eye diagram of the recovered data (demodulated by the tag) when the reader sends data at 500 kbps.	89
Figure 5.16: (a) Data sent to the reader by the tag @ 10 Mbps, by modulating the injection-locked SOM's natural oscillation frequency, (b) measured spectrum of the transmitted data from the tag.	90
Figure 6.1: Illustration of the proposed single CMOS-die active MMID tag that uses a harvested energy from an incoming mm-wave signal from the reader.	95
Figure 6.2: Two MMID system design platforms of choice: (a) AiP-based MMID system reported in [62]; (b) AoC-based MMID system proposed in this work.	96
Figure 6.3: Illustration of the proposed rectangular slot antenna on CMOS process.	100
Figure 6.4: Illustration of E-field field distributions in the slot region of a rectangular -ring slot antenna: (a) the first resonant mode; and (b) the second resonant mode.	101
Figure 6.5: Reflection coefficient $ S_{11} $ (dB) of the rectangular slot antennas at 24 GHz ($L_a=1.78$ mm, $L_b=0.89$ mm, $S=0.04$ mm, $W_{CPW}=0.05$ mm, $S_{CPW}=0.02$ mm, $L_{CPW}=0.16$ mm) and 40 GHz ($L_a=1.32$ mm, $L_b=0.43$ mm, $S=0.04$ mm, $W_{CPW}=0.05$ mm, $S_{CPW}=0.02$ mm, $L_{CPW}=0.39$ mm).	102
Figure 6.6: Simulated 3D radiation patterns of the dual-band rectangular slot antenna: (a) 24 GHz, (b) 40 GHz.	103
Figure 6.7: Illustration of the proposed dual-band rectangular slot antenna on CMOS process.	104

Figure 6.8: Transmission from the common input port to the 40 GHz rectangular slot.	104
Figure 6.9: E-field field distributions in the slot region of a rectangular slot antenna: (a) the first resonant mode; and (b) the second resonant mode.	105
Figure 6.10: Reflection coefficient $ S_{11} $ (dB) of the dual-band rectangular slot antenna ($L_{a1}=1.78$ mm, $L_{b1}=0.89$ mm, $L_{a2}=1.32$ mm, $L_{b2}=0.43$ mm, $S=0.04$ mm, $W_{CPW}=0.05$ mm, $S_{CPW}=0.02$ mm, $L_{CPW1}=0.16$ mm, $L_{CPW2}=0.19$ mm).	106
Figure 6.11: Simulated 3D radiation patterns of the dual-band rectangular slot antenna: (a) 24 GHz, (b) 40 GHz.	107
Figure 6.12: Geometry of the proposed DRA.	108
Figure 6.13: Gain .vs. DR thickness D_h	109
Figure 6.14: Gain .vs. DR dimension D_x	109
Figure 6.15: Electric field distribution of the proposed antenna: (a) 24 GHz, (b) 40 GHz.	110
Figure 6.16: Simulated 3D radiation patterns of the dual-band rectangular slot antenna with DRA: (a) 24 GHz, (b) 40 GHz.	110
Figure 6.17: Radiation measurement setup of the fabricated on-chip dual-band slot antenna ($L_a=1.78$ mm, $L_b=0.89$ mm, $S=0.04$ mm, $W_{CPW}=0.05$ mm, $S_{CPW}=0.02$ mm, $L_{CPW}=0.16$ mm) and 40 GHz ($L_a=1.32$ mm, $L_b=0.43$ mm, $S=0.04$ mm, $W_{CPW}=0.05$ mm, $S_{CPW}=0.02$ mm, $L_{CPW}=0.39$ m) (a) block diagram; (b) die microphotograph of the fabricated antenna without DR; (c) antenna with DR.	112
Figure 6.18: Reflection coefficient $ S_{11} $ (dB) of the antenna (simulated and measured).	113
Figure 6.19: Measured and simulated radiation patterns (a) H-plane 24 GHz, (b) H-plane 40 GHz, (c) E-plane 24 GHz, (d) E-plane 40 GHz.	115

LIST OF SYMBOLS AND ABBREVIATIONS

AiP	Antenna-in-Package
AM	Amplitude Modulation
AoC	Antenna-on-Chip
ASK	Amplitude Shift Keying
BW	Bandwidth
CMOS	Complementary Metal Oxide Semiconductor
CPW	Coplanar Waveguide
CW	Continuous Wave
DC	Direct Current
DRA	Dielectric Resonator Antenna
EIRP	Effective Isotropic Radiated Power
FCC	Federal Communications Commission
GCPW	Grounded Coplanar Waveguide
HF	High Frequency
HFSS	High Frequency Structural Simulator
IC	Integrated Circuit
IF	Intermediate Frequency
IoT	Internet of Things
LF	Low Frequency
LiR	Line Regulation
LO	Local Oscillator
LoR	Load Regulation

MMID	Millimeter-Wave Identification
PCE	Power Conversion Efficiency
RF	Radio Frequency
RFID	Radio Frequency Identification
Rx	Receiver
SIW	Substrate Integrated Waveguide
SOM	Self-Oscillating Mixer
Tx	Transmitter
UHF	Ultra-High Frequency
VBW	Video Bandwidth
VCO	Voltage Controlled Oscillator

LIST OF APPENDICES

Appendix A – list of publications	132
---	-----

CHAPTER 1 INTRODUCTION

The earliest RFID systems were based on quasi-static magnetic flux coupling among the reader's and tag's coils, such as those using low frequencies (from 100 kHz to 2 MHz) or high frequencies (at 13.56 MHz). Later on, radiative (or far-field coupling) RFID systems which permit longer communication links (ultra-high frequencies from 850 MHz to 950 MHz), and microwave frequencies (at 2.45 GHz and 5.8 GHz) were adopted. Recently, RFID technology has been propelled into the millimeter-wave era, to alleviate restrictions that have been limiting the evolution of low-frequency RFID technology [1]. The emerging MMID technology is poised to clearly exploit advantages from operating in this frequency band, therefore circumvents limitations of low-frequency RFID technology. The emerging MMID technology presents several advantages, namely:

- ◆ At millimeter-wave frequencies, the small effective wavelength makes it possible for a reader to implement a directive and high-gain antenna array [2], and with a beam steering capability, the reader can localize and identify tags one-by-one among a densely deployed MMID tags or sensors with a quasi-laser precision (pinpoint localization). This cannot be made possible with today's commonly used UHF RFID technology. Besides, at millimeter-wave frequencies, circuit components become smaller, thereby allowing a smaller tag and smaller handheld reader that could even be integrated into our mobile phone [3].
- ◆ The larger available bandwidth at millimeter-wave frequency and the line of sight communication (a very directive antenna for both reader and tag) enable a highly-secured data exchange between a reader and a tag at a high bit-rate, regardless of the type of modulation and coding. Besides, the losses inherent to millimeter-wave propagation confines the personal data indoor, therefore resolving the primordial issue of security and ethic.

In addition, the still-emerging MMID concept is fully compatible with future applications of millimeter-wave technology in wireless communications and which are being discussed and developed worldwide, such as 5G and IoT (Internet of Things).

1.1 Motivation and Objectives

In addition to the aforementioned advantages of an MMID system, over these millimeter-wave frequency bands the effective wavelength is close to a typical CMOS die size. Therefore, if antennas could either be integrated on the same chip (antenna-on-chip –AoC) or embedded in the associated package (antenna-in-package –AiP), and assuming that energy could be wirelessly and efficiently harvested at millimeter-wave frequencies so as to allow a tag transmit its data to a reader at millimeter-wave frequencies, it becomes possible then to envisage a complete MMID tag that is fully integrated on a single CMOS die. The development of this new generation of high data-rate, battery-free, yet active μ RFID technology with full on-chip integration operating at mm-wave frequencies has been the motivation for this Ph.D. thesis work. Accordingly, the main goal of this thesis is fourfold:

- ✓ Propose and analyze an architecture of an MMID system (reader-tag) that addresses the underlying technical challenges and fully benefits from the advantages of operating at millimeter-wave frequencies.
- ✓ Propose, analyze, and develop techniques to efficiently convert an RF energy (at millimeter-wave frequencies) into a DC energy.
- ✓ Propose, analyze, and develop ultra-low-power millimeter-wave transceivers that could only rely on a harvested energy to operate.
- ✓ Develop and demonstrate a high data-rate, single-chip, battery-free, yet active MMID tag, exploring two major solutions (antenna-in-package and antenna-on-chip) for highly integrated millimeter-wave systems.

Since the tag cost represents the main factor that limits a widespread adoption of a new technology, a standard, low-cost, and commercially available CMOS process with a high integration capability is the process of choice, regardless of the significant design challenges in achieving the desired performances, especially in the scope of millimeter-wave integrated circuits design.

1.2 Contribution and Organization of the Thesis

This thesis is written in articles-based format, and all the chapters are organized as follow:

Chapter 1: Introduction

This chapter introduces the millimeter-wave identification technology and its potential advantages, and highlights the thesis work's motivation, objectives, contribution, and its organization.

Chapter 2: Literature review

This chapter reviews the key notions of RFID technology, wireless power harvesting techniques using CMOS circuits, and the millimeter-wave identification (MMID) technology.

Chapter 3 Article 1: High-Efficiency Wideband Rectifier for Single-Chip Batteryless Active Millimeter-Wave Identification (MMID) Tag in 65-nm Bulk CMOS Technology

This chapter demonstrates that RF energy at millimeter-wave frequencies can be wirelessly harvested and converted into DC energy, with power conversion efficiencies that were never demonstrated before at such frequencies. Starting from a differential-driven cross-coupled rectifier topology that was demonstrated to work at UHF frequencies only, we have investigated its characteristics and performances at 24 GHz, 35 GHz and 60 GHz. In order to achieve high conversion efficiency, we have then redesigned and optimized its circuit parameters and the chip layout specifically for these millimeter-wave bands. This has been demonstrated through an implementation using a standard commercially available CMOS technology. This chapter also proposes a new MMID reader-tag system architecture that addresses and solves the underlying technical challenges associated to commonly used passive RFID systems.

Chapter 4 Article 2: Low-Power Injection-Locked Zero-IF Self-Oscillating Mixer for High Gbit/s Data-Rate Battery-Free Active μ Rfid Tag at Millimeter-Wave Frequencies in 65-nm CMOS

In this chapter, an extremely low-power millimeter-wave transceiver that relies only on harvested energy for its power supply, is proposed and demonstrated in 65-nm standard CMOS technology. The transceiver is based on a self-oscillating mixer architecture, which we have improved through key circuit topology modifications and design considerations. Our transceiver is capable, on one hand (during reader-to-tag communication) to receive an AM-modulated signal at mm-wave frequency and to down-convert to baseband signal without any external local oscillator nor an IF stage, which results in minimal current consumption. On the other hand (during tag-to-reader communication), the same self-oscillating mixer directly up-converts a high-data-rate binary signal into the millimeter-wave band.

Chapter 5 Article 3: High-Data-Rate Single-Chip Battery-Free Active Millimeter-Wave Identification Tag in 65-nm CMOS Technology

This chapter demonstrates a miniaturized ($10 \times 10 \text{ mm}^2$) high-data-rate, self-powered, yet active MMID tag on a single-chip. The tag wirelessly harvests its energy at millimeter-wave frequency, receives an interrogator signal at millimeter-wave carrier frequency (and it is assumed that in the intended application data is then written in the tag), and transmits back its data at high-bit-rate to a reader on a millimeter-wave carrier frequency as well. The tag's antennas are embedded in the package (antenna-in-package).

Chapter 6 Article 4: On-Chip Dual-Band Rectangular Slot Antenna for Single-Die Millimeter-Wave Identification Tag in Standard CMOS Technology

In this chapter, we address and tackle the well-known drawbacks of silicon-based integrated antennas, which are the antenna's radiation efficiency and silicon required surface. A dual-band and high-efficiency rectangular slot antenna is demonstrated using a standard bulk CMOS process. The demonstrated antenna supports the feasibility of a fully integrated MMID tag on a single CMOS-die (a CMOS-only MMID tag), with no external components whatsoever.

Chapter 7: General Discussion

This chapter provides a general discussion on potential applications and novel opportunities enabled by our research in this thesis.

Chapter 8: Conclusion and Future Works

This chapter concludes the thesis with a brief highlight of the achieved results and suggests some areas in which future extensions of this work could be targeted.

CHAPTER 2 LITERATURE REVIEW

This chapter reviews the key notions of RFID technology, wireless power harvesting techniques using CMOS circuit platforms, and the millimeter-wave identification (MMID) technology.

2.1 RFID Technology

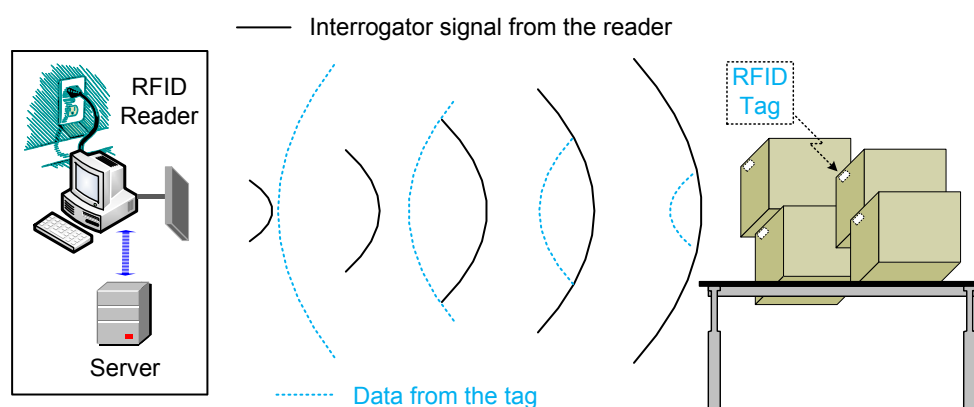


Figure 2.1: Illustration of an RFID system.

Among many other identification technologies, RFID, which has widely impacted our everyday life in many areas, is a technology that uses radio communications to wirelessly and automatically identify objects or people. A typical RFID system is generally a two-way communication system (figure 2.1), where a base station (called a reader or an interrogator), wirelessly exchanges data with a device (called a tag or a transponder) which is attached to the object or the people to be identified [4]. Readers are generally complex and connected to a host computer or a network, whereas transponders target simplicity, low-price, and small size (generally use integrated circuits) for a widespread adoption and a massive-use of the technology.

2.1.1 Different types of RFID

RFID systems are essentially categorized by the way power is supplied to the tag, by the protocols used for communication between the tag and the reader, and by the operating frequency as well. The choice of frequency, power source, and protocol greatly affects the cost, communication range, tag size, data security and features available to the user, etc., which generally influence how the RFID technology is adopted and spread into the market.

2.1.1.1 Active RFID

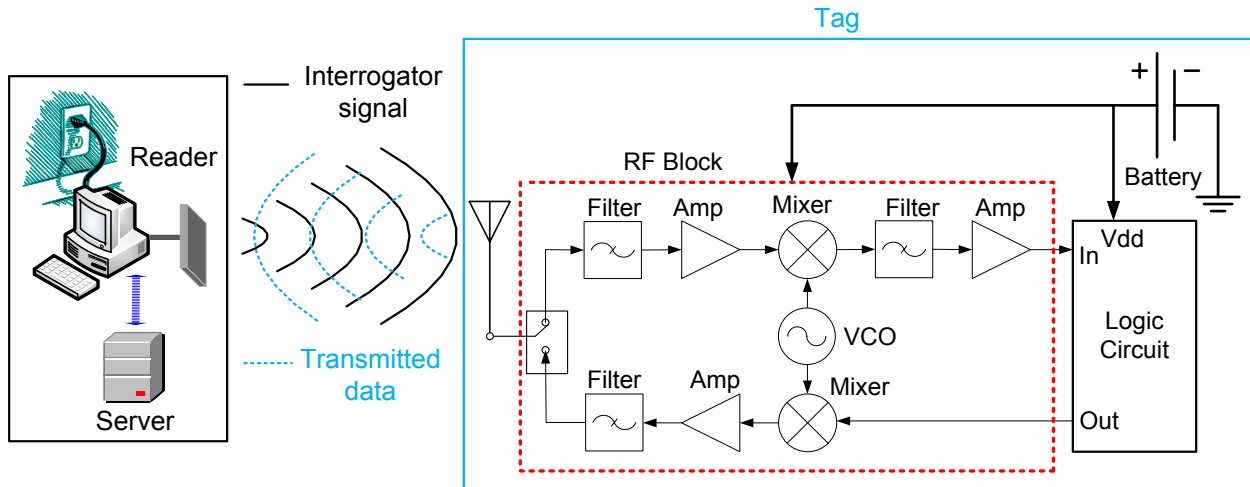


Figure 2.2: A general representation of a typical active RFID system.

As illustrated in Fig. 2.2, which depicts a general representation of a typical active RFID system, an active RFID tag is nothing else than a conventional bidirectional radio communication device, with its own power source, conventional transceiver, sensors, memory, a digital processing block, etc. Active tags are the most expensive and are often used for specialized applications where tracking or locating objects requires a long range of communication (tens or hundreds of meters), a high security data-exchange, and an environment where the reader-tag path is obstructed (no line of sight from a reader to tag). They are, for example, commonly used for tracking shipping

containers, and they are able to discriminate one container from another even when containers are in close proximity to one another.

2.1.1.2 Passive RFID

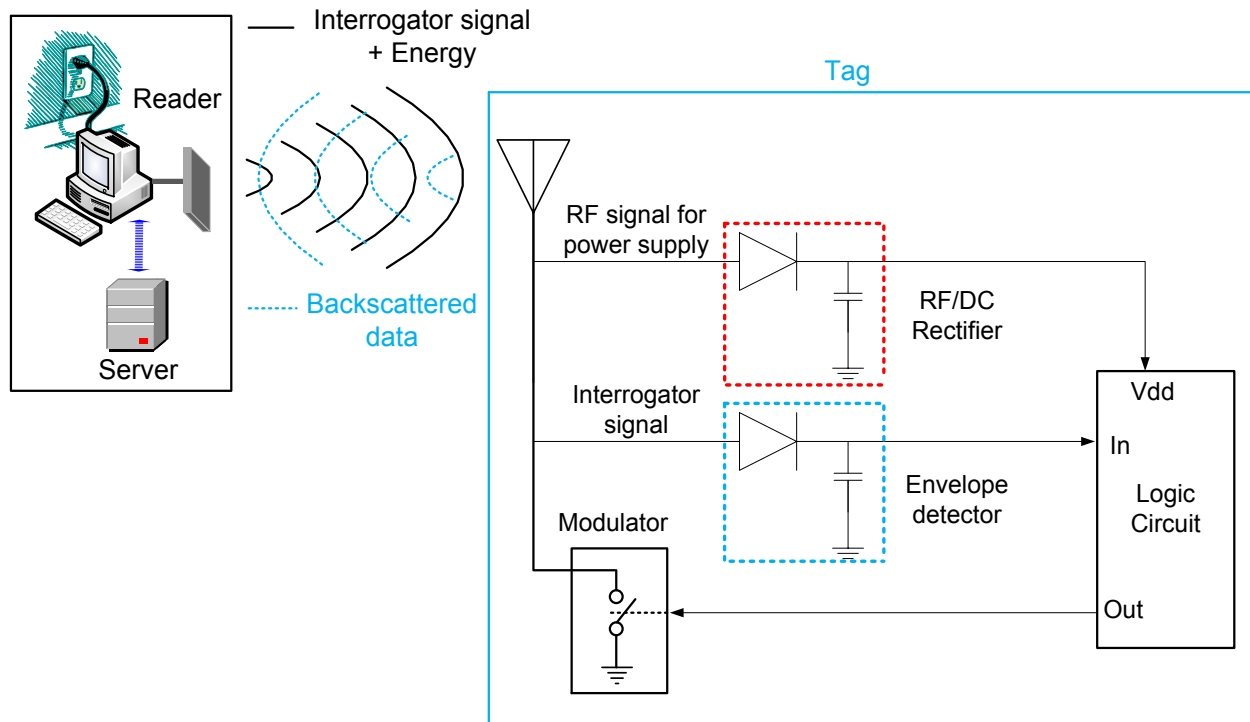


Figure 2.3: A general representation of a typical passive RFID system.

Figure 2.3 illustrates a simplified representation of a typical passive RFID system (in reality, a passive RFID tag could be more sophisticated than this representation). Unlike the active RFID tag, a passive RFID tag does not have an independent power source nor a dedicated radio transceiver. The tag rectifies the RF signal received from the reader to recuperate its energy and power up its logic and non-volatile memory circuitries. The tag responds back to the reader (sending its data to the reader) by modifying its antenna's impedance seen by the reader (backscattering modulation technique). In figure 2.3, the modulator is conceptually represented by a simple switch. By switching on/off the modulator as a function of the digital data to be sent, it

changes the electrical characteristics of the antenna in a way that the reflected signal from the antenna is analogously an AM-modulated signal.

Since passive RFID tags have neither radio transceiver nor any dedicated power source, they are relatively simple in terms of manufacturing cost and complexity, they are small, and therefore are low cost devices without any related maintenance fees (they could be deployed in a hostile or less accessible environment). However, their simplicity comes with some disadvantages:

- a) Communication range is greatly limited by the capability of the tag to harvest sufficient energy for its logic and memory circuitries (the sensitivity of the rectifier circuit). This limitation is particularly proportional to the operating frequency since propagation losses increase with frequency.
- b) Since the tag relies on the rectified power, computational power must be minimized and the tag must be designed in a way to use very little of the rectified power. Therefore, integration of sensors and functionalities are limited by the limited power budget and the reader uses very simple protocols to communicate with the tag.
- c) Limited energy resources (limited computational power) greatly affects security and privacy as well, since it limits the capability to implement different coding techniques in order to improve the security of the exchanged data between the reader and the tag.

➤ **Link power-budget for a typical passive RFID system**

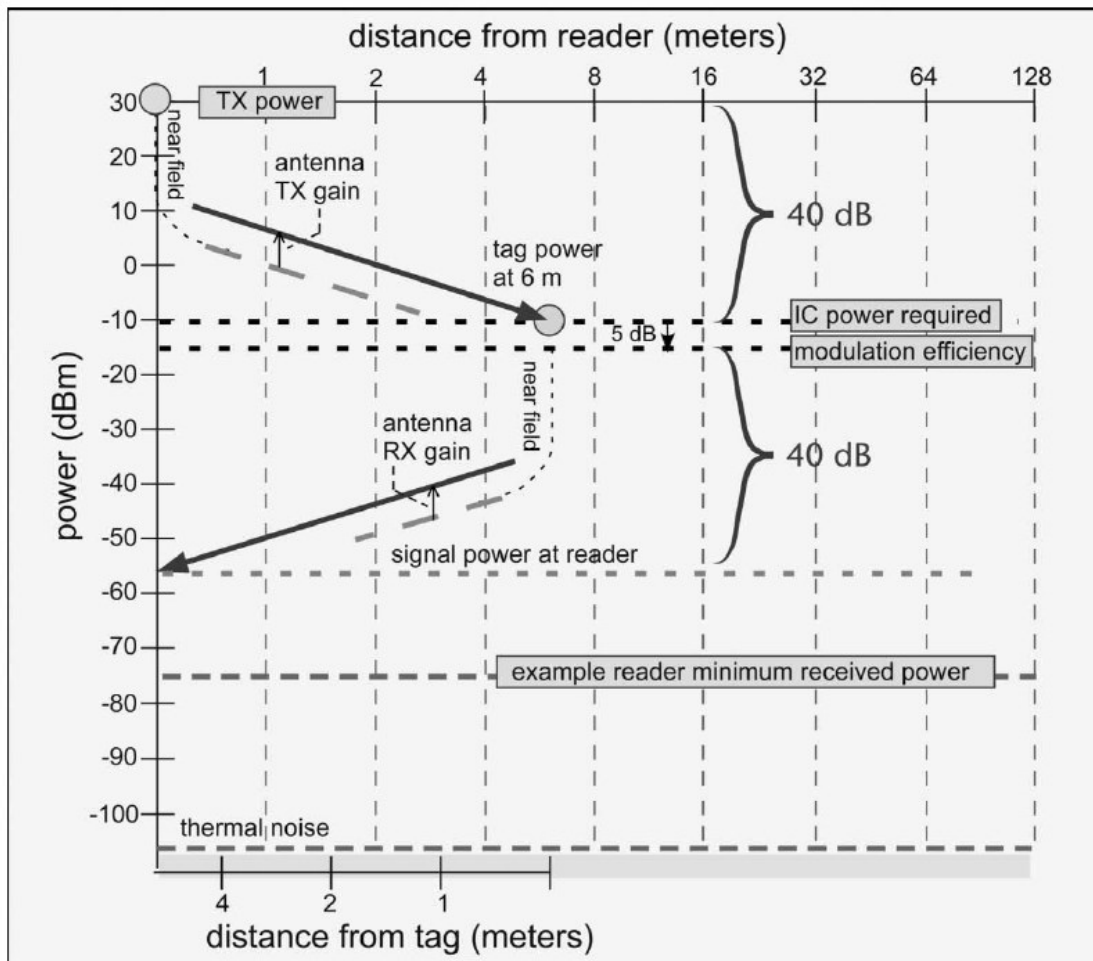


Figure 2.4: Link power-budget for a typical passive RFID system [4].

Figure 2.4 provides a more detailed communication range analysis. A passive RFID system has two principal constraints limiting its operation: the power transferred to the transponder and the power received by the reader. The system has two critical power levels, the transponder sensitivity and the reader sensitivity (the minimum power levels required by the transporter and the reader). As illustrated in figure 2.4, the operating range is a smaller range between uplink (tag-to-reader) and downlink (reader-to-tag) communication range. It is in fact set up by the downlink communication range, because for a wirelessly powered tag (passive RFID system), the operating

range is limited by the capacity of a tag to harvest sufficient energy for its circuitry (downlink), rather than the reader's sensitivity (uplink) which is generally very good (low power level).

➤ **Limitations of a real free-space communication environment**

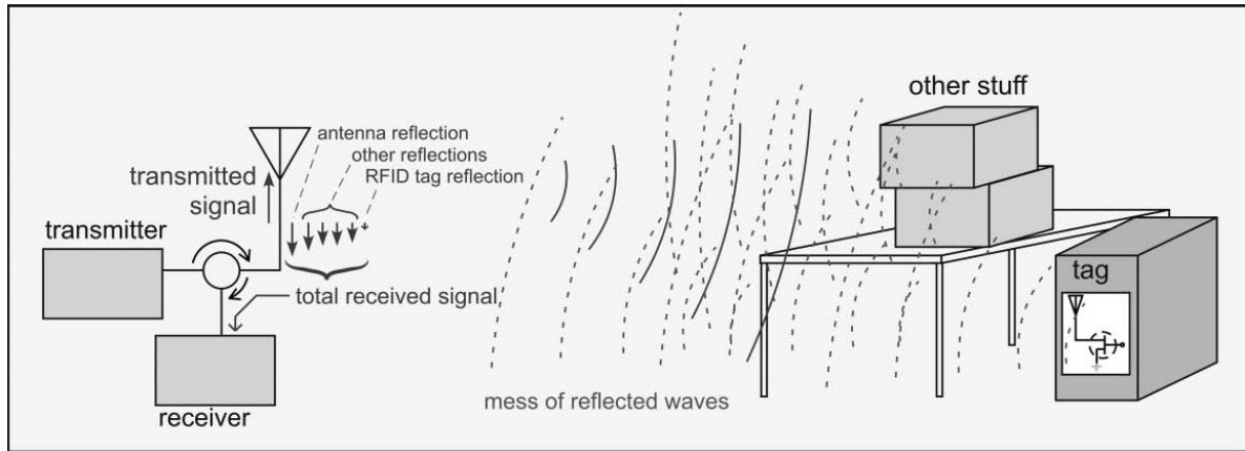


Figure 2.5: Realistic environment of a passive RFID system [4].

As discussed above, in a backscattering passive RFID system, a reader continuously sends a high power signal to power up the tag, while listening to a very weak reflected signal, sent by the tag as a result of the impedance-switching of its own antenna. However, as depicted in figure 2.5 where a real environment is full of reflectors, the total received signal by the reader consists not only of the wanted signal that carries the tag information, but also the reader's transmitter leaked signal (self-jamming), the signal reflected by the transmitter's own antenna, and other reflected signals from surrounding objects. The signal that comes from the leakage (coupling between the reader's transmitter and the reader's receiver) dominates the overall noise at the receiver side. This negatively impacts the reader sensitivity, and the phenomenon is more severe for higher operating frequency (the higher the operating frequency goes, the worse the isolation between the reader's transmitter and the reader's receiver becomes).

2.1.1.3 Semi-Passive RFID

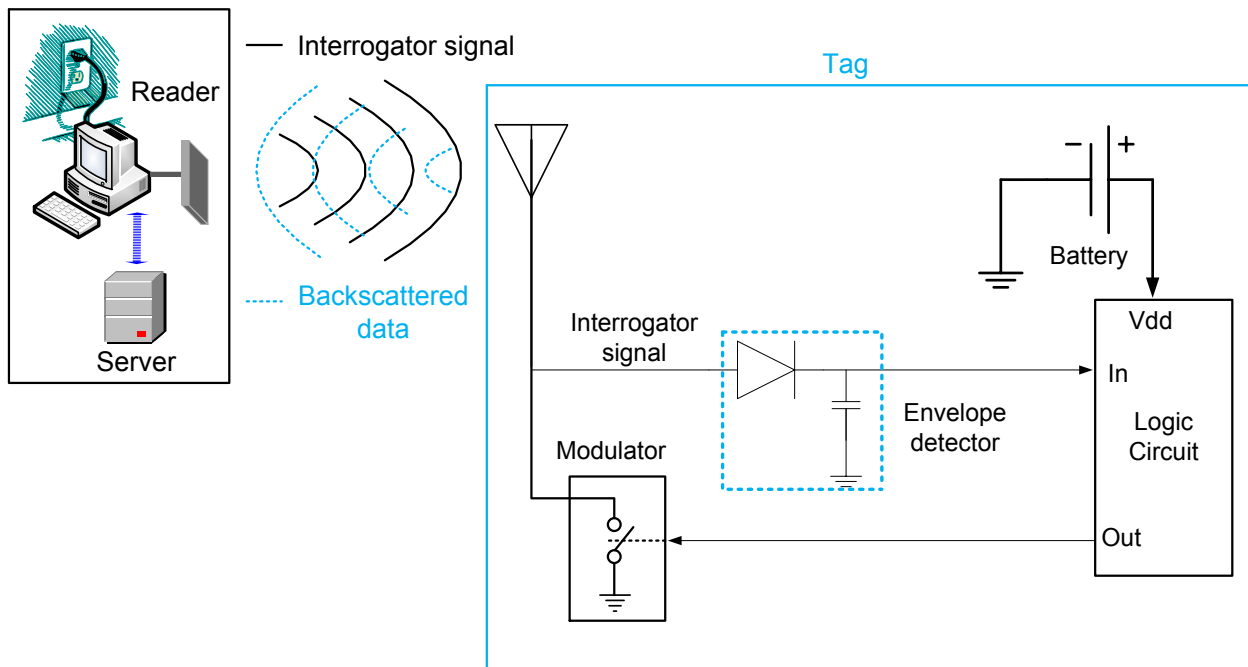


Figure 2.6: A general representation of a typical semi-passive RFID system.

As illustrated in figure 2.6, a semi-passive tag is a battery-assisted passive tag. It has a dedicated battery to power up the tag's circuitry, but, like passive tag, it still uses backscattering modulation technique for uplink communication (tag-to-reader communication). It also does not have a radio transmitter. Since it incorporates a power source, a semi-passive tag could integrate more functions and extend the communication range (a communication distance of about 100 meters is feasible). It is more likely to respond at such distances, compared to its passive tag counterpart which relies on the rectified energy. Therefore, semi-passive tags are used in dedicated applications such as tracking high-value assets where missing a tag (a tag does not respond) cannot be tolerated. Reliability is privileged over an increase in tag size due to battery or the maintenance related cost.

2.1.1.4 Chipless RFID

Unlike the commonly used RFID tags, chipless RFID technology does not incorporate a digital logic circuit, therefore suffering from the inability to write data to the tag. In some chipless RFID applications, surface-acoustic wave (SAW) devices and electromagnetic resonant techniques are used. However, it is worth noting that the cost of printing technologies is considerably higher than that of silicon manufacturing, for the same complexity. In high volume production, it is cheaper to fabricate a circuit on silicon than to print it directly onto a PCB substrate. Besides to the lack of flexibility of the kind that exists with a digital logic circuit (a CMOS IC), manufacturing cost seems to be the main factor that limits the evolution and a wide-spread adoption of the chipless RFID technology. It is now limited to some specialized applications.

2.1.2 RFID Operating Frequency Bands

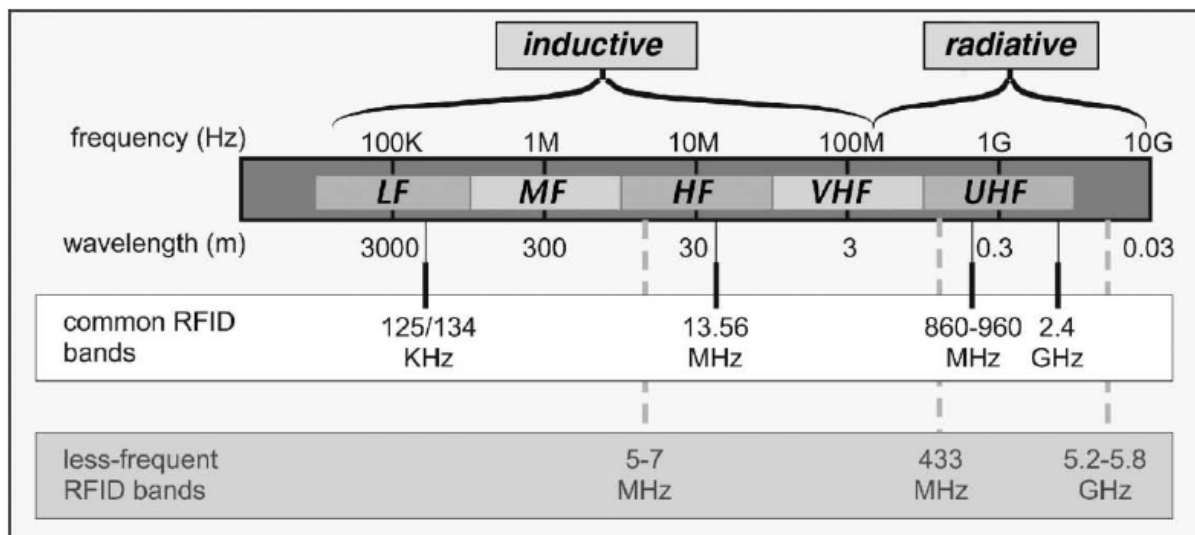


Figure 2.7: RFID frequency bands [4].

With today's wireless communication explosion, RFID technology should fairly cohabit with other wireless systems without interference. Note, for example, in the 860-960 MHz band an RFID system should directly cohabit with cellular telephony and other popular wireless systems

operating in this crowded band. As illustrated in figure 2.7, the most commonly used frequency bands which have been made available by regulatory agencies (FCC for USA, CRTC for Canada) are the 125/134 kHz (low-frequency: LF), 13.56 MHz (high-frequency: HF), 860–960 MHz (ultra-high-frequency: UHF), 2.4–2.45 GHz (UHF or microwave), and 5.2–5.8 GHz (microwave band). These restricted narrow bands have mostly been made available for unlicensed ISM (industrial, Scientific and Medical) activities. Low-frequency RFID systems are generally inductively coupled and limited to low data rate with a short communication range, whereas UHF RFIDs are radiative and provide a higher data rate, longer communication range, and smaller tag size.

2.1.3 RFID Tags Implemented Using CMOS Technology

With the extensive use of RFID technology together with a relentlessly declining DC power consumption in the novel integrated circuits, integrating micro- or nano-sensors that implement novel functionalities and decisional algorithms (digital signal processing) prompts new classes of RFID technology. To deploy a large number of those sensors or tags, however, requires a cost- and integrability-effective fabrication process. A standard, low-cost, and commercially available CMOS process with a high integration capability is the process of choice for a widespread adoption and massive applications of RFID technology. Recently published work's performances are summarized in Table 2.1.

Table 2.1: Performance summary of UHF/microwave passive RFID tags in CMOS technology.

Frequency	Data Rate	Communication Range	Power Consumption	Technology	Reference
868-915 MHz	100 kbps	9.25 m	2.3 μ W	0.5 μ m CMOS	[5]
915 MHz	≥ 1 Mbps	15.7 m	600 nW	0.18 μ m CMOS	[6]
915 MHz	10 Mbps	-	63 μ W	0.5 μ m CMOS	[7]
925 MHz	107 kbps	19.6 m	3.2 μ W	0.18 μ m CMOS	[8]
2.45 GHz	100 kbps	12 m	2.7 μ W	0.5 μ m CMOS	[9]
2.45 GHz	200 kbps	15 cm	120 μ W	0.25 μ m CMOS	[10]
2.45 GHz	≥ 1 Mbps	4 m	600 nW	0.18 μ m CMOS	[6]
2.45 GHz	10 Mbps	1 mm	-	0.18 μ m CMOS	[11]
5.8 GHz	≥ 1 Mbps	1.5 m	600 nW	0.18 μ m CMOS	[6]

2.2 Wireless Power Harvesting with CMOS-based Rectifier Circuits

2.2.1 Conventional Diode-Connected Transistor

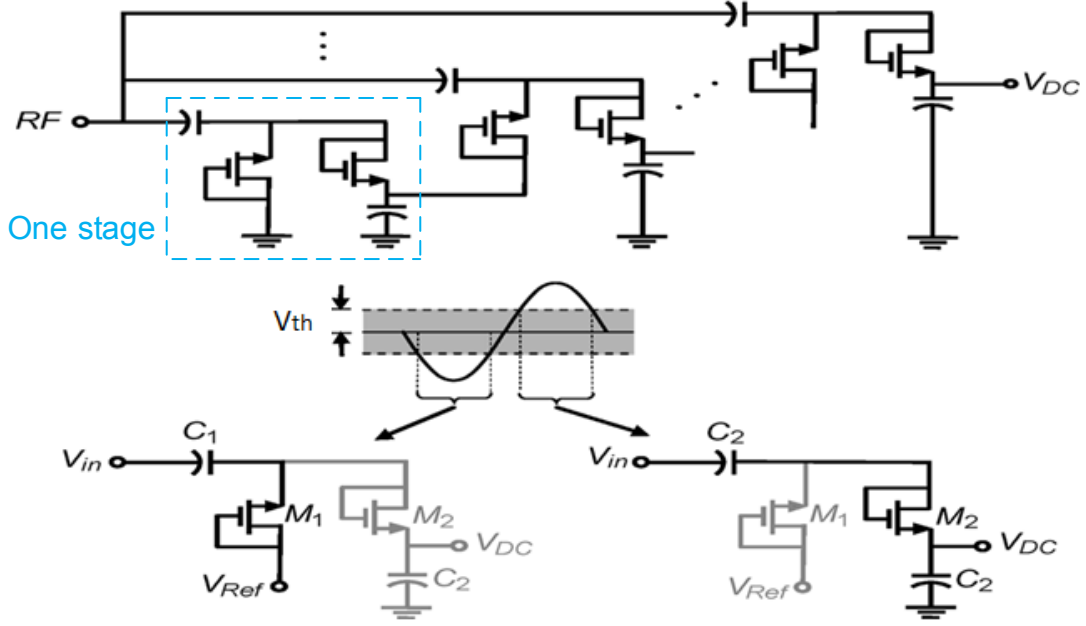


Figure 2.8: Wireless power harvesting using a CMOS-based voltage multiplier [12].

For a commercially available standard CMOS process, a conventional diode-connected transistor plays the role of the rectifying element such as its counterpart Schottky diode. As illustrated in figure 2.8, a voltage multiplier structure is the commonly used technique to boost the rectified voltage. As highlighted (figure 2.8), a one stage (a full-wave rectifier) consists of two diode-connected transistors M_1 and M_2 , and two capacitors C_1 and C_2 . In its negative phase, the incoming RF signal V_{in} swings below some reference voltage (V_{Ref}) minus the transistor's threshold voltage V_{th1} and the transistor M_1 turns on, allowing the current I_{M1} to flow from ground (or some V_{Ref}) into capacitor C_1 . In the positive phase and when $V_{in} > V_{th2}$, transistor M_2 turns on and current I_{M2} flows from C_1 to C_2 . As long as an RF source is connected to the rectifier, the diode-connected transistors will periodically charge the capacitors, and a DC voltage develops

across the output node. High threshold voltage V_{th} of diode-connected transistors significantly degrades the rectifier's sensitivity (conventional diode-connected transistors are not suitable for small RF signals or long communication range).

2.2.2 Power-Matching and Voltage Gain-Boosting Network

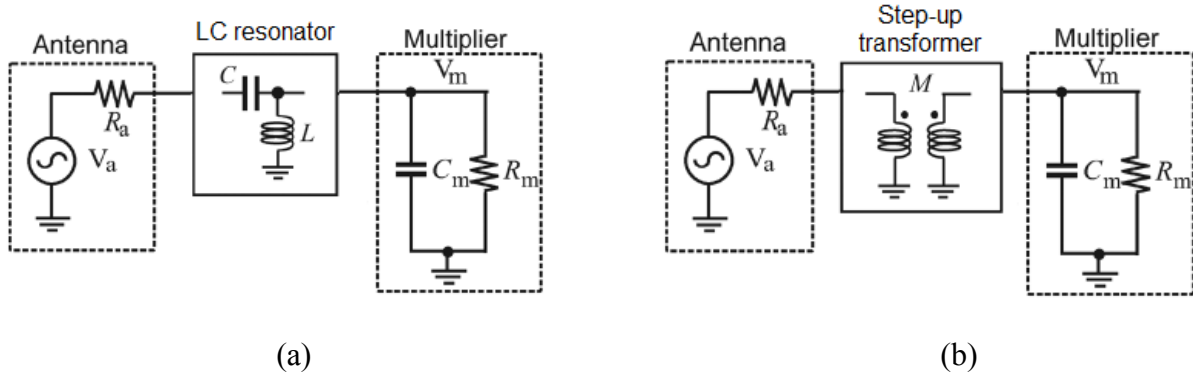


Figure 2.9: Passive voltage-boosting network: (a) using an LC-resonator, (b) using a step-up transformer [13].

It is clear that to boost the power conversion efficiency of the voltage multiplier, both the power matching (between the antenna and the voltage multiplier) must be optimized and the amplitude of the voltage from the antenna must be maximized.

As illustrated in figure 2.9 (a), an LC network impedance transformer is inserted between the antenna and the multiplier. The LC network provides a matching impedance to the antenna in order to maximize the power transmission from the antenna to the voltage multiplier. At the same time, by resonating at the carrier frequency, the voltage at the output of the LC network (the input of the multiplier) is maximized, therefore enhancing the overall power conversion efficiency. The topology in Figure 2.9 (b) takes advantages offered by a step-up transformer, to simultaneously provide a power-matching and a voltage gain-boosting. With a step-up transformer, the same power can be delivered from the primary winding to the secondary winding, but with a higher voltage at the secondary winding.

The LC -based and the step-up transformer-based impedance transformer networks are limited by the low quality factor of spiral inductors in standard CMOS technologies.

2.2.3 External Threshold Voltage Cancellation

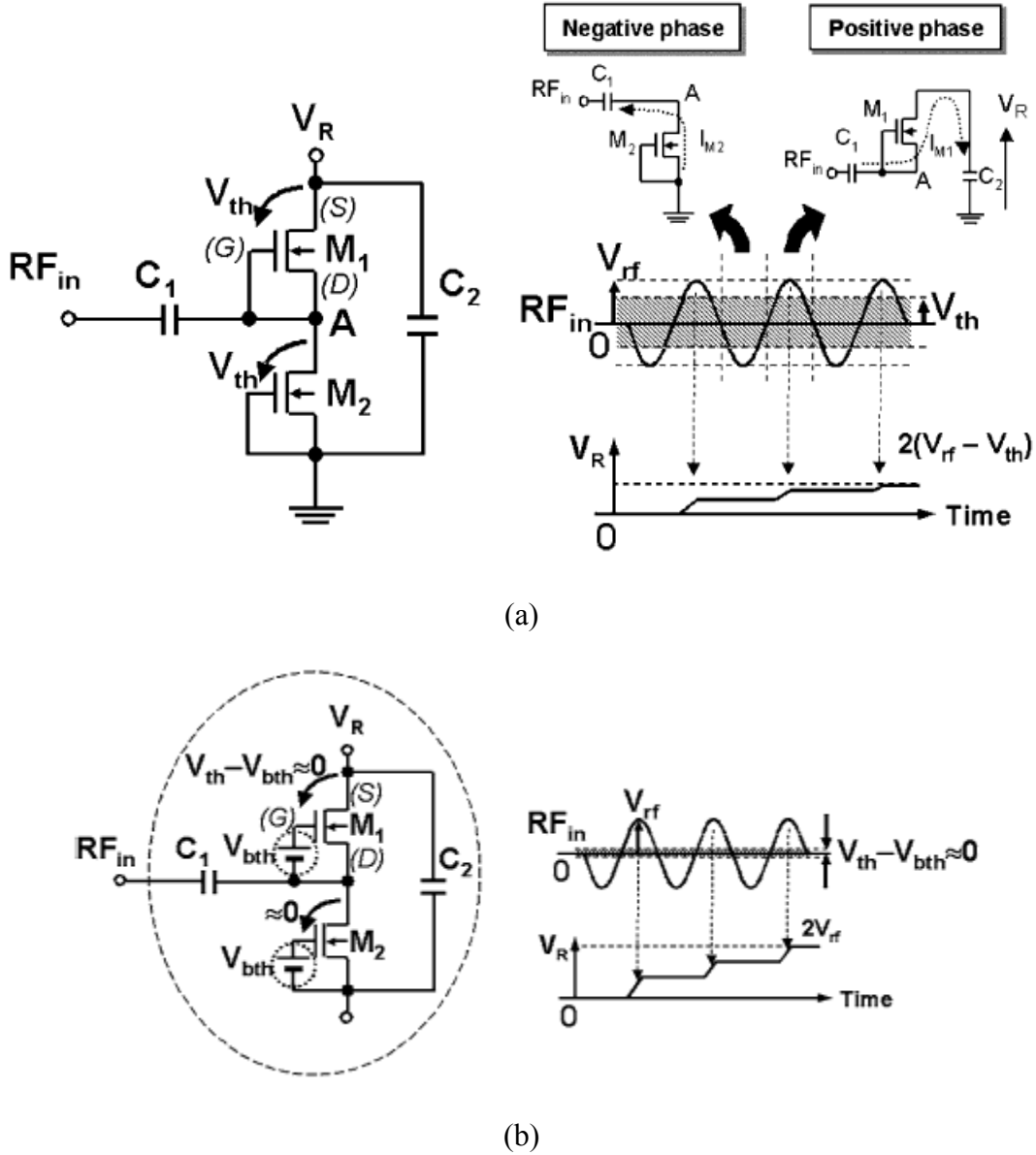


Figure 2.10: Diode-connected transistor rectification mechanism: (a) without external bias, (b) with external bias [14].

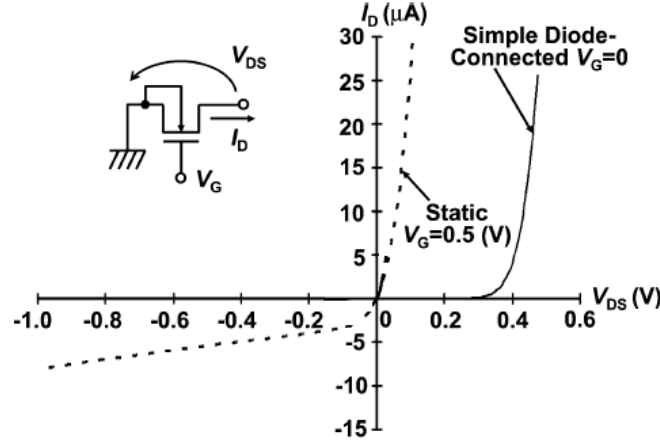


Figure 2.11: I-V curve of a diode-connected transistor with/without external bias [15].

As illustrated in figure 2.10 (b), in this approach, a bias voltage V_{bth} is connected between the gate G and drain D terminals of each transistor. Therefore, the effective threshold voltage decreases from V_{th} to $V_{th}-V_{bth}$, thereby increasing the rectifier's sensitivity (the rectifier can detect and rectify small incoming RF signals: for long-distance communication). The rectified current increases with the bias voltage. However, when the source voltage becomes greater than the drain voltage, due to the MOS transistor symmetrical structure, diode-connected transistors suffer from a reverse leakage current (figure 2.11) that discharges the output capacitor, therefore degrading the overall power conversion efficiency. Besides, this technique could only be applied in an active or a semi-passive tag, since V_{bth} itself has to be externally generated.

2.2.4 Zero-Threshold Voltage Transistors (native transistors)

Lower transistor's threshold voltage enhances power conversion efficiency, since it presents a low turn-on resistance. Therefore, some rectifiers are implemented using low-threshold or zero-threshold voltage transistors models, generally called native transistors. These models are available in some standard CMOS processes. However, leakage current increases exponentially with the decrease of the transistor's threshold voltage V_{th} , resulting in the suppression of the increase in power conversion efficiency PCE. Finally, a rectifier using very low- V_{th} or near-zero threshold voltage (native) transistors perform much better at lower RF power values (small turn-on voltage), but as the input power rises further, they perform poorly because of leakage current.

2.2.5 Cross-Coupled Differential-Drive Topology

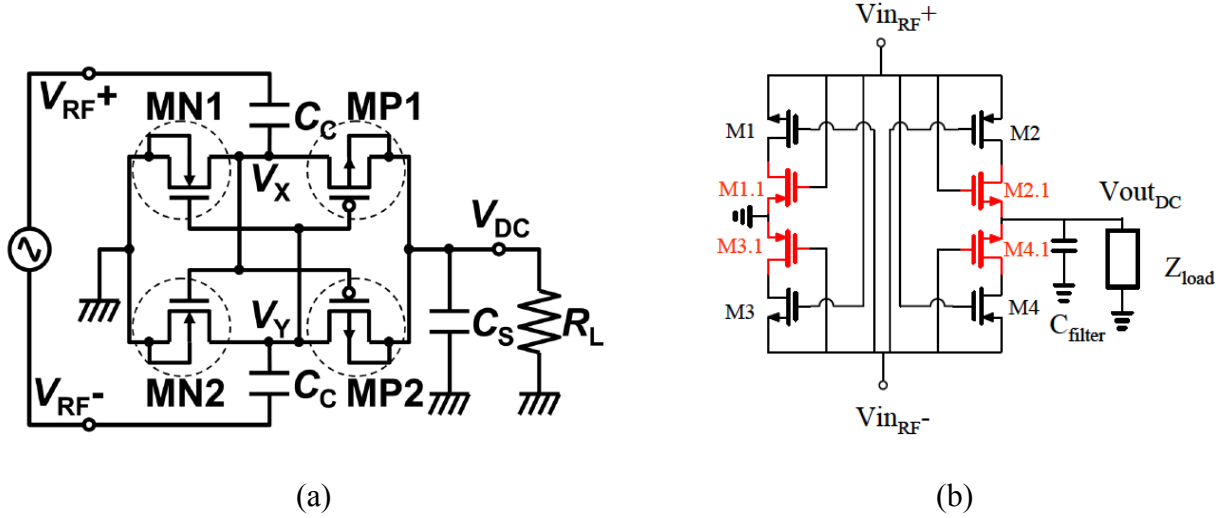


Figure 2.12: Circuit schematic of a cross-coupled differential-drive rectifier: (a) conventional topology [15], (b) improved topology [16].

As previously mentioned, a static gate bias voltage increases the rectifier's sensitivity compared to the simple diode-connected transistor without any external gate-biasing. As illustrated in figure 2.11, static biasing also increases reverse leakage current, therefore degrading the overall power conversion efficiency, especially as the received RF power increases. However, the cross-coupled topology shown in figure 2.12 addresses this on-resistance and leakage current trade-off. Since the rectifier is differentially driven, reverse leakage current is minimized by a negative gate voltage. Therefore, both smaller on-resistance and smaller reverse leakage current are simultaneously obtained. With a modified topology (figure 2.12 (b)), leakage current is greatly reduced or ideally suppressed, thereby allowing high efficiency over a wide dynamic range of input power. This relates to realistic operating conditions of the tag, where the distance between a reader and a tag may vary at any time, which automatically introduces a variation in the received power. Table 2.2 summarizes and compares performances of the previous published CMOS rectifiers using different techniques to enhance both power conversion efficiency and the rectifier's sensitivity.

Table 2.2: Performance summary of CMOS rectifiers using different rectification techniques.

Rectifier Technique	Frequency	Sensitivity	Output DC Power	Efficiency	Technology	Reference
Diode-Connected Transistors	900 MHz	-7.0 dBm	2.4 μ W (0.4 V @ 6 μ A)	1.2 %	0.25 μ m CMOS	[17]
Voltage Gain-Boosting Network	3.85 GHz	-12.0 dBm	2 μ W (1 V @ 2 μ A)	3.0 %	0.18 μ m CMOS	[13]
External Threshold Voltage Cancellation	950 MHz	-14.0 dBm	0.6 μ W (1.5 V @ 0.4 μ A)	1.5 %	0.3 μ m CMOS	[14]
Zero-Threshold Voltage Transistors	900 MHz	-11.0 dBm	5 μ W (1 V @ 5 μ A)	6.5 %	0.18 μ m CMOS	[18]
Cross-Coupled differential-drive Topology	953 MHz	-10.0 dBm	65 μ W (1.8 V @ 36 μ A)	65 %	0.18 μ m CMOS	[15]

2.3 Millimeter-Wave Identification (MMID) Technology

Recently, some works in MMID technology have been published and none of them has experimentally demonstrated a complete MMID system that fully takes advantages of operating at mm-wave band.

2.3.1 Chipless MMID tag

In [20], a chipless MMID tag at 30 GHz is presented. The chipless tag encodes data into the spectral signature using a multi-resonator. A circuit with 6 spiral resonators and two cross-polarized transmitting and receiving circular UWB monopole antennas is presented. The results shown are not supported by any experimental data and the simulation results show a large spectral use from 24 to 36 GHz (2 GHz by bit). In [21], a 6-bit mm-wave chipless tag is proposed. The tag comprises

two orthogonally polarized slot loaded circular patch antennas, which are connected by a right angle transmission line. The slot on the patch determines the individual resonant frequency signatures, hence the number of identification data bit. However, density of the coding still small (1.6 GHz by bit). In [22], an equalization method is used in order to maximize the number of encoded bits in time-domain reflectometry (TDR) tags. The designed SIW tag is comprised of 4 symmetrical iris in H-plane with integrated slot-antenna. The reader should be used to read code information from a tag with one or more modulation types (phase, polarization, frequency and time domain) in order to yield a significant enhancement of bit density.

2.3.2 MMID tag with integrated chip

In [23], for example, a standard UHF RFID chip is combined with external mixers to up-convert the transmit-UHF signal to 10 GHz and down-convert the received 10 GHz signal to the UHF, with a 40kbit/s data rate. In [24], a 60 GHz RFID tag design is published, but a low RF-to-DC power conversion efficiency (1.2% at 2dBm input power) translates into a bit-by-bit sequential communication, limiting the data rate to only 5kbit/s at a communication range of 1.3 cm.

CHAPTER 3 ARTICLE 1: HIGH-EFFICIENCY WIDEBAND RECTIFIER FOR SINGLE-CHIP BATTERYLESS ACTIVE MILLIMETER-WAVE IDENTIFICATION (MMID) TAG IN 65-NM BULK CMOS TECHNOLOGY

Pascal Burasa, Nicolas G. Constantin, and Ke Wu

Published in the *IEEE Transactions on Microwave Theory and Techniques*, vol.62, no. 4, pp.
1005-1011, Apr. 2014

This paper presents the development and demonstration of a high-efficiency rectifier for millimeter-wave (or mm-wave)-to-dc energy conversion. It is a critical circuit block that renders possible the use of a single CMOS chip die with no substrate and wiring, as the implementation of a batteryless, yet active tag for next generation high data-rate mm-wave identification (MMID) technologies. We also propose an architecture of Reader-Tag system that addresses the underlying technical challenges. The rectifier is based on a differential drive cross-coupled topology that has been shown to work at UHF frequencies only so far. In this paper, we investigate significant challenges in implementing this topology at mm-wave frequencies with good power conversion efficiency (PCE). The analyses, design and results presented in this work demonstrate the feasibility of achieving this by minimizing simultaneously the small on-resistance and the reverse leakage current in the MOS transistors, and by reducing losses and parasitic capacitances through proper transistor sizing and layout optimization. Using a standard 65-nm bulk CMOS process, a chip was designed, fabricated, and tested under different input and output loading conditions. The rectifier exhibits an overall PCE of 20% at 24 GHz, 18% at 35 GHz, and 11% at 60 GHz under RF available driving power of 6, 6, and 3 dBm, respectively, and output load resistance of 1, 1, and 2 k Ω , respectively. These PCE performances at mm-wave frequencies have never been reported in the literature.

3.1 Introduction

As an emerging technology, Radio Frequency Identification (RFID) is being increasingly used in many areas of our everyday life, such as access control, security, and supply chain management. However, the restricted standard rules, the tag size (mainly dominated by antenna), and limited data rate dictated by available bandwidths, have impeded the evolution of the UHF RFID applications. Driven by the ever-increasing needs, such as smaller size and higher data rates, RFID technology has entered into the mm-wave era to exploit the inherently smaller antenna size and larger available bandwidths [19]. Batteryless MMID becomes only possible if a tag can be powered wirelessly and it still benefits from these advantages at mm-wave frequencies. However, to the best of our knowledge, such MMID has not been reported yet. In [23], a standard UHF RFID chip is combined with external mixers to up-convert the transmit-UHF signal to 10 GHz and down-convert the received 10 GHz signal to the UHF, with a 40-kbit/s data rate. In [24], a 60 GHz RFID tag design is reported, but the low RF-to-dc PCE (1.2% at 2dBm input power) translates into a bit-by-bit sequential communication, limiting the data rate to 5 kbit/s at a range of 1.3 cm.

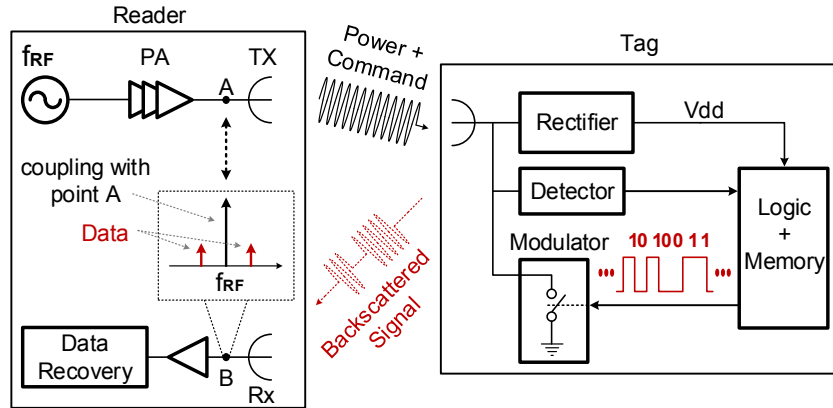


Figure 3.1: Illustration of a reader-tag RFID system using backscattering.

A major challenge in developing a passive MMID is that the backscattering modulation technique generally used in passive UHF RFIDs performs poorly at mm-wave frequencies. As depicted in Fig.3.1, in a backscattering passive RFID system, a reader continuously sends a high power signal to power up the tag, while listening to a very weak reflected signal, sent by the tag

with a form of amplitude modulation as a result of the impedance-switching of its own antenna. The signal received by the reader consists of two sidebands carrying the tag information, and a carrier tone level that is augmented by the reader's transmitter leakage signal and its associated side-band noise. This impacts negatively the reader sensitivity, but is acceptable in UHF RFIDs. However, the weaker backscattered signal at mm-wave frequencies (due to smaller tag-antenna aperture), as well as lower reader TX-RX isolation, higher phase noise in its mm-wave oscillator and low reader dynamic range [24] compromise this modulation technique at mm-wave frequencies. Therefore, batteryless "active" MMID technologies will benefit from a new reader-tag system that is free of backscattering.

In section II of this paper, a new MMID reader-tag system that is free of backscattering modulation is proposed at a conceptual level. The successful implementation of such a system, however, will require mm-wave-to-DC rectifiers with good PCE performances, e.g., $\sim 10\%$ at 35 GHz under an RF input power of 6 dBm. To the best of our knowledge, a CMOS rectifier with such performances has never been reported in the literature. Note that published papers on mm-wave rectennas (e.g., [25]-[29]) make use of Schottky diodes and are intended for operation at significantly higher power levels than what is required in our applications.

In section III, we analyze and describe the design of a rectifier that was successfully tested using a commercial standard 65-nm CMOS process, with measured PCE performances of 20%, 18%, and 11% at 24, 35, and 60 GHz, respectively. Section IV presents and discusses the measurement results.

3.2 Proposed MMID System with Batteryless Tag

The MMID reader-tag system proposed for batteryless "active" MMID tags, which does not require backscattering, is illustrated in Fig.3.2. It uses two mm-wave frequencies, freq-1 for a continuous wave (CW) dedicated to energy source for the tag, and freq-2 for down and up-link communications only. Therefore, the reader interrogates and listens to the tag at any time without interrupting the energy feed to the tag, hence without compromising the rectifier's PCE. Moreover, it eliminates the issue of charging and discharging synchronization stated in [24], as well as the

issue of a reader sensitivity degradation associated with backscattering. This leads to a more relaxed coding and modulation methods, as well as higher data rates in both communication links.

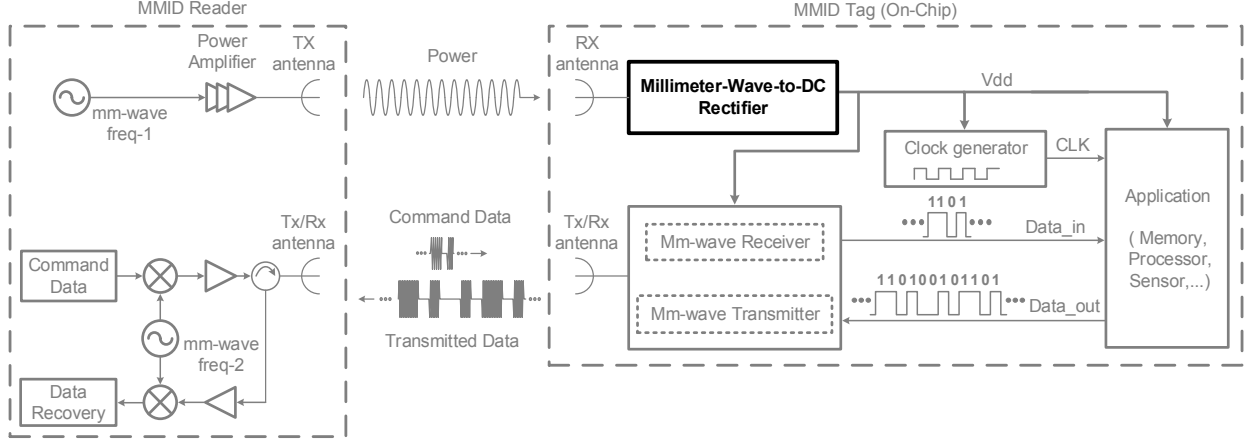


Figure 3.2: Block diagram of the proposed MMID system with a batteryless active tag on single-chip.

Previous works have reported mm-wave CMOS VCOs with power consumption of few hundreds of micro-watts despite a large tuning range [30], a dual-band on-chip antenna with 7.4 and 6.5 dBi gain at 35 and 94 GHz, respectively [31], and a clock generator consuming only 24nW at 5.12 MHz [32]. Besides, at UHF, the state-of-the art has shown fully-integrated passive RFID transponders (including control logic and memory blocs) consuming less than 3 μ W dc power [33], [34]. Assuming a 1 W effective isotropic radiation power (1 W EIRP) from a reader, a tag antenna gain of 6 dBi [31], and a conservatively high dc power of 500 μ W dissipated by the MMID tag (excluding the rectifier), then a power link budget analysis at 35 GHz using Friis equation shows that a 10% PCE is required for the rectifier to enable communication over 2 cm. With the design presented in this paper, we have measured a PCE of 18% at 35 GHz. This renders possible MMID systems as in Fig. 3.2, employing a batteryless “active” tag that is fully integrated on a single CMOS die, with no substrate, no die-attach and no wiring.

3.3 Millimeter-Wave-to-DC Rectifier

Fig.3.3 (a) shows the rectifier schematic, based on a cross-coupled bridge topology that has been investigated at UHF only so far [15]. It is driven by a differential input signal V_{RF} applied across nodes V_{in_rf+} and V_{in_rf-} . During the positive cycle of V_{RF} , and as the difference between V_{in_rf+} and V_{in_rf-} swings above transistors' threshold voltage V_{th} , pulsed currents $IM3_pos$ and $IM2_pos$ circulate through M3 and M2. The resulting current equals the fluctuating charge-current through C_{load} plus the dc current drawn by the MMID tag. In the negative cycle of V_{RF} , C_{load} is charged by $IM4_neg$ and $IM1_neg$. As long as an RF source is connected to the rectifier, transistors M1, M2, M3, and M4 will periodically charge C_{load} , and a dc voltage develops across the MMID tag.

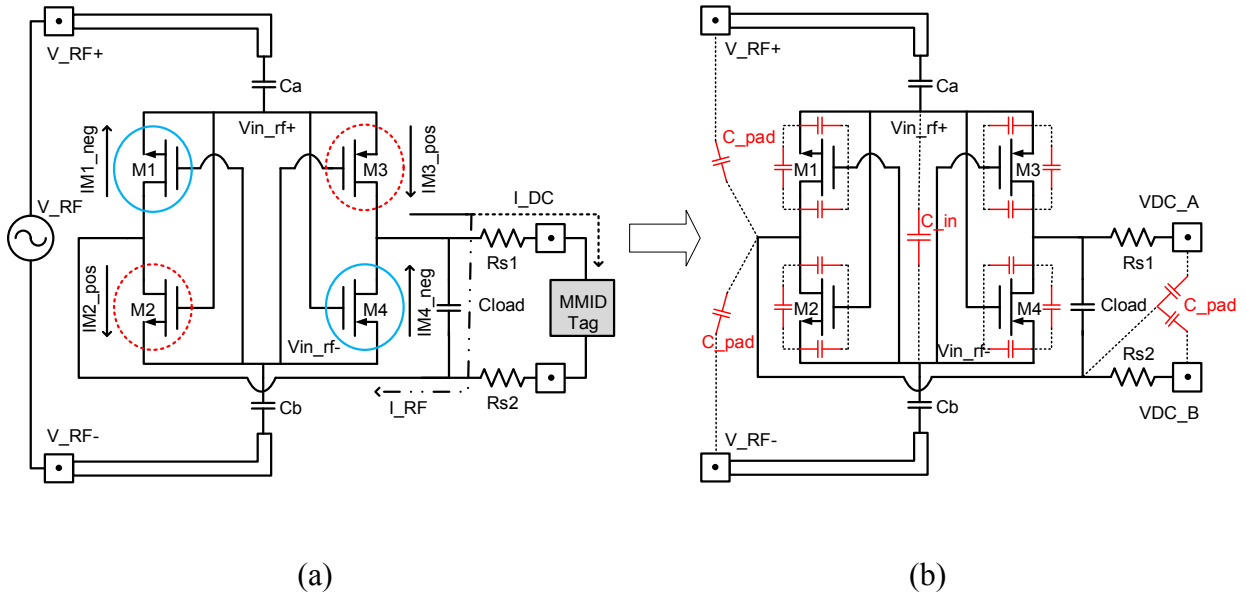


Figure 3.3: Cross-coupled bridge configuration CMOS rectifier used in this paper. (a) Differential-drive circuit schematic, (b) Equivalent capacitor model.

The cross-coupled bridge topology allows a small on-resistance by biasing the NMOS (M2) in the saturation mode, with a high gate voltage during the positive cycle of V_{RF} . It also allows reducing the unwanted Source-to-Drain reverse leakage current in M2 (due to the MOS

symmetrical structure) during the negative cycle of V_{RF} by pulling down this transistor's gate voltage.

The same mechanisms in opposite cycles of V_{RF} apply for the other NMOS and the PMOS transistors, resulting into high PCE at UHF. At mm-wave frequencies, though, parasitic capacitances and series losses associated with C_a , C_b , and C_{load} capacitors dominate and degrade significantly the PCE. This will be analyzed in the following, with the help of formulations from [18].

As shown in Fig.3.3 (b), at mm-wave frequencies, the cross-coupled bridge topology implies a large parasitic capacitor C_{in} that reduces the differential voltage, and the transistors operate in weak-inversion region (higher channel resistance), resulting in a low PCE. C_{load} is then charged by a weak sub-threshold current defined by (3.1)

$$I_{sub} = I_{so} \cdot \frac{W}{L} \cdot e^{V_{gs}/nV_T} (1 - e^{-V_{ds}/V_T}) \cdot (1 + \lambda_{sub} V_{ds}) \quad (3.1)$$

with

$$I_{so} = \mu \sqrt{\frac{q\epsilon_{si}N_{ch}}{2\phi_s}} \cdot (V_T)^2 \cdot e^{(-V_{th}-V_{off})/nV_T} \quad (3.2)$$

where q is the electron charge, ϵ_{si} is the silicon permittivity, N_{ch} is the doping concentration, ϕ_s is the surface potential, V_T is the thermal voltage, λ_{sub} is the sub-threshold region channel-length modulation parameter, V_{off} is the sub-threshold region offset voltage, V_{th} is the threshold voltage, n is the sub-threshold region swing parameter, W is the transistor width, L is the transistor length, and μ is the electron mobility.

As displayed in Fig.3.3 (b), for both cycles, C_{in} is approximated as:

$$C_{in} = \begin{cases} C_{in}(pos) = C_{gs2(on)} + C_{gs3(on)} + C_{gs1(off)} + C_{gs4(off)} \\ C_{in}(neg) = C_{gs2(off)} + C_{gs3(off)} + C_{gs1(on)} + C_{gs4(on)} \end{cases} \quad (3.3)$$

with,

$$\begin{cases} C_{gs(on)} = \frac{2}{3} \cdot \frac{\epsilon_{ox}}{t_{ox}} \cdot W \cdot L \\ C_{gs(off)} = \frac{\epsilon_{ox}}{t_{ox}} \cdot W \cdot L_{diff} \end{cases} \quad (3.4)$$

where ϵ_{ox} , t_{ox} , and L_{diff} are the oxide dielectric constant, the oxide thickness, and the channel length diffusion, respectively. To minimize C_{in} (3.4), smaller transistor width W should be used. However, smaller W also decreases saturation current I_{sat} (3.5), consequently decreasing Cload charge-current and the PCE.

$$I_{sat} = \frac{1}{2} \mu C_{ox} \left(\frac{W}{L} \right) (V_{gs} - V_{th})^2 \quad (3.5)$$

Larger transistor W enhances I_{sat} (3.5), but larger W increases both parasitic capacitances (3.4) and leakage current (3.6), thus degrading PCE (charges leak away). On the other hand, a higher loading current (500 μ A as targeted for the novel MMID tag) requires large-enough Cload and transistor widths. Larger capacitors Ca, Cb, and Cload imply higher losses, severely degrading PCE.

$$I_{leak} = I_{so} \cdot \frac{W}{L} \cdot (1 - e^{-V_{ds}/V_T}) \cdot (1 + \lambda_{sub} V_{ds}) \quad (3.6)$$

Moreover, a low V_{th} is beneficial to I_{sat} (3.5), but also implies a larger leakage current (3.6). Finally, a longer channel implies more parasitic capacitance (3.4), making the minimum usable L the best design choice.

The above-described complex design trade-offs show that a performant mm-wave rectifier design necessitates a thorough optimization. In this work, we aimed at optimizing the rectifier's PCE by simulation for best transistor and capacitor sizes, as a function of the loading current. Note however, that since a rectifier is a large-signal nonlinear circuit, a more robust optimization actually requires a much more complex procedure, such as what was proposed in [35], where source-pulling characterization is employed.

Our simulations showed that minimal transistor sizes yield an optimal design choice for our mm-wave rectifier. In addition, layout parasitic capacitances are critical for PCE. Hence, the distances between polysilicon gate, source, and drain contacts were optimized to reduce C_{gs} , C_{gd} , and C_{ds} .

In order to minimize capacitive coupling between metal traces, together with the associated losses, the transistors may be kept further apart to allow more distance between the metal traces. On the other hand, too long metal traces severely degrade the PCE because of excessive substrate losses. This aspect was taken into consideration during the layout design, through multiple iterations of post-layout simulation.

Series resistances R_{s1} and R_{s2} (Fig. 3.3) were added for test purposes, in order to isolate the small Cload capacitor from the bigger and lossy parasitic capacitors in the test pads. R_{s1} and R_{s2} ensure that the RF signal flows through Cload, rather than C_pad or being radiated by the probe cable.

3.4 Design and Measurement Results

3.4.1 Chip Design and Measurement Setup

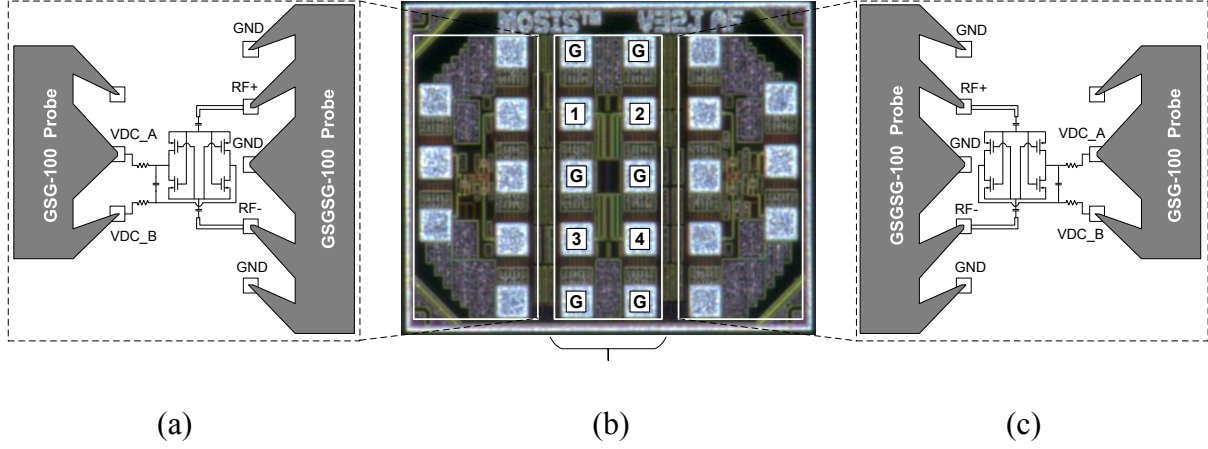


Figure 3.4: Micrograph of the fabricated rectifier. (a) Narrow rectifier version, (b) De-embedding bloc, (c) Wider rectifier version.

Fig.3.4 shows the die photograph of the fabricated test circuit with a chip area of $0.6 \text{ mm} \times 0.45 \text{ mm}$ including RF pads, but with an active area of only $50 \mu\text{m} \times 50 \mu\text{m}$. The chip contains two rectifier design variants, one with narrower transistor and capacitor sizes (Fig.3.4 (a)) and the second with wider sizes (Fig.3.4 (c)), as well as a de-embedding bloc on the middle (Fig.3.4 (b)) for characterization and loss estimation for the input pads and transmission lines. The chip was fabricated using a standard 65-nm bulk CMOS technology, with regular- V_{th} transistors, given that its RF model was the only one available in the design kit.

Transistor and capacitor sizes were optimized through simulation to obtain an approximated DC power of $500 \mu\text{W}$, as required for the active MMID tag. The narrower rectifier shown in Fig.3.4 (a) has W/L ratios of $1.2\mu\text{m}/60\text{nm}$ and $2.16\mu\text{m}/60\text{nm}$ for NMOS and PMOS transistors, respectively, and 77fF for C_a , C_b , and the C_{load} low-loss MIM capacitor. For the wider rectifier, the sizes are $1.8\mu\text{m}/60\text{nm}$ for NMOS, $3.24\mu\text{m}/60\text{nm}$ for PMOS, and 135fF for C_a , C_b , C_{load} . A ratio of 1.8 between NMOS and PMOS transistors was chosen in order to have the same charge

transferred (same on-resistance) through a NMOS transistor and a PMOS transistor as well. Rs1 and Rs2, of 300 Ω each, were sufficient to isolate Cload from the output pad parasitic capacitor. To minimize input losses, small and low-loss probing pads were used.

The rectifier was measured on-wafer with differential probes, and differentially driven using True-Mode Stimulus Application (TMSA) feature of Agilent N5247A PNA-X, to generate a true differential signal. A variable load resistor was connected to the output of the rectifier to emulate different dc power dissipated by an MMID tag. The rectifier's power conversion efficiency (PCE) was computed as:

$$\text{PCE (\%)} = \frac{P_{\text{DC}}}{P_{\text{av}}} \cdot 100 \quad (3.7)$$

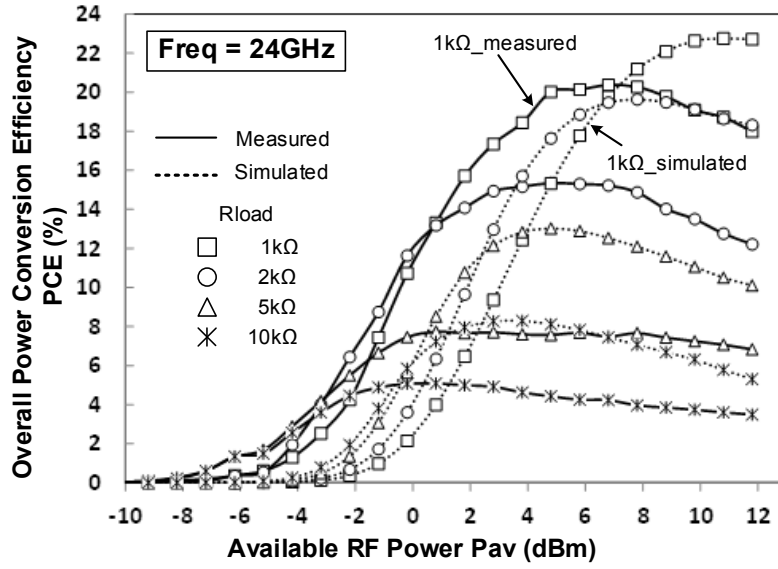
with P_{DC} being the dc power dissipated by the load resistor (including Rs1, Rs2), and P_{av} the available power at the rectifier input. Note that the efficiency would be higher if the mismatch loss were factored in (i.e. using the RF input power absorbed by the circuit instead of P_{av}).

3.4.2 Millimeter-Wave-to-DC Rectifier Performances

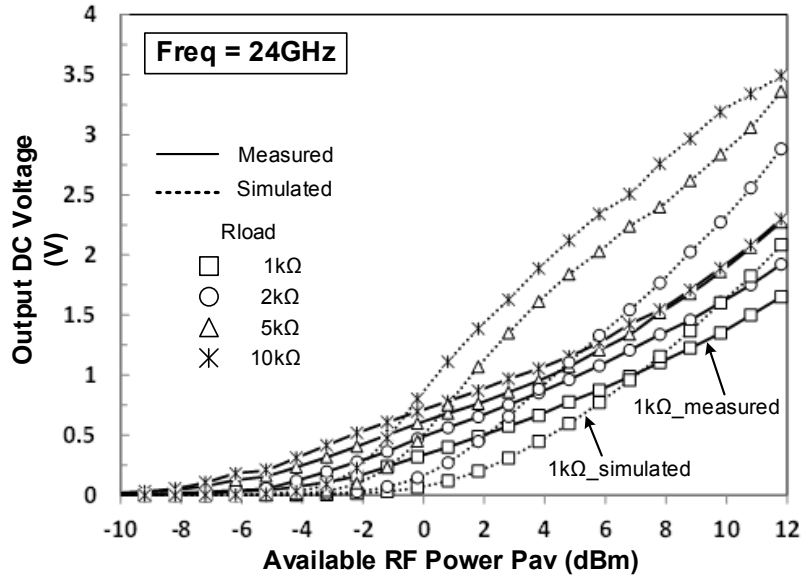
Substrate losses measured after calibration show an insertion loss $S_{12} = S_{43}$ of 2.2 dB at 24 and 35 GHz, and 2.7 dB at 60 GHz. The results presented in Fig. 3.5 to 3.7 below were obtained with the design variant with wider transistors.

The measurements were carried out at three frequencies: 24, 35, and 60 GHz over a wide mm-wave band. The PCE dependence on the available input RF power (P_{av}) was treated in [18], but is further analyzed here in the mm-wave context. As seen in figures 3.5 (a), 3.6 (a), and 3.7 (a), the PCE increases with the available RF power P_{av} , reaches a maximum and starts to decrease as P_{av} keeps increasing. This inflection is due to the increasing drain-gate voltage that induces a reverse operation of the MOS transistors (because of their symmetrical device structure) at the time the RF differential signal applied to the gates is supposed to turn the transistors off. These leakage

currents circulate in the opposite direction to IM2_pos, IM4_pos, IM1_neg and IM3_neg in Fig. 3.3 (a), and therefore reduce the charging of Cload.

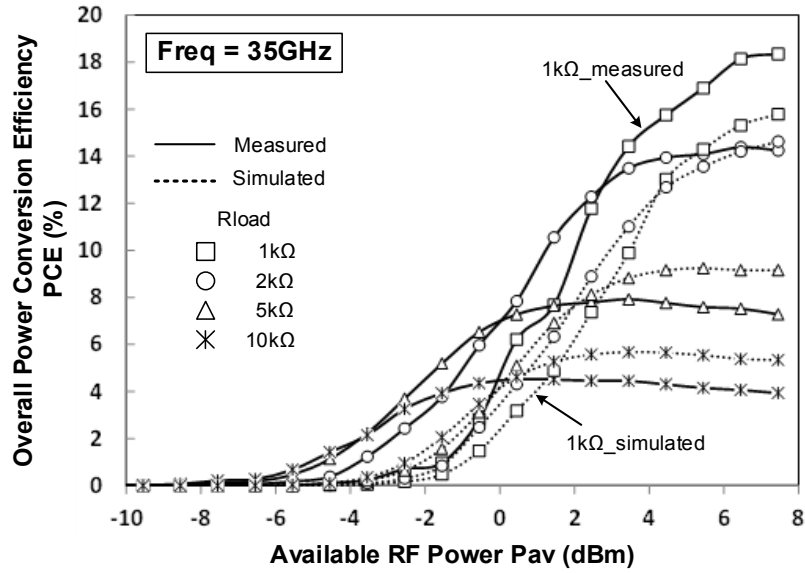


(a)

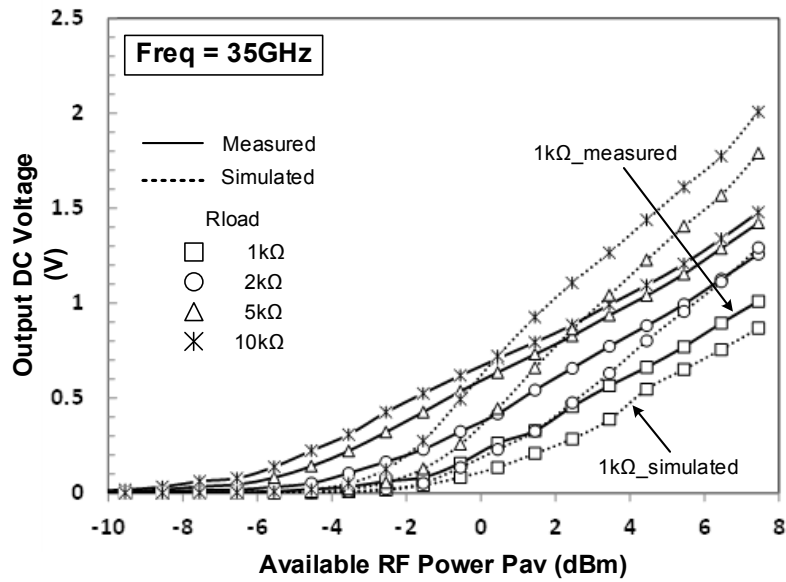


(b)

Figure 3.5: Measured and simulated results at 24 GHz. (a) PCE versus P_{av} , (b) dc voltage versus P_{av} .

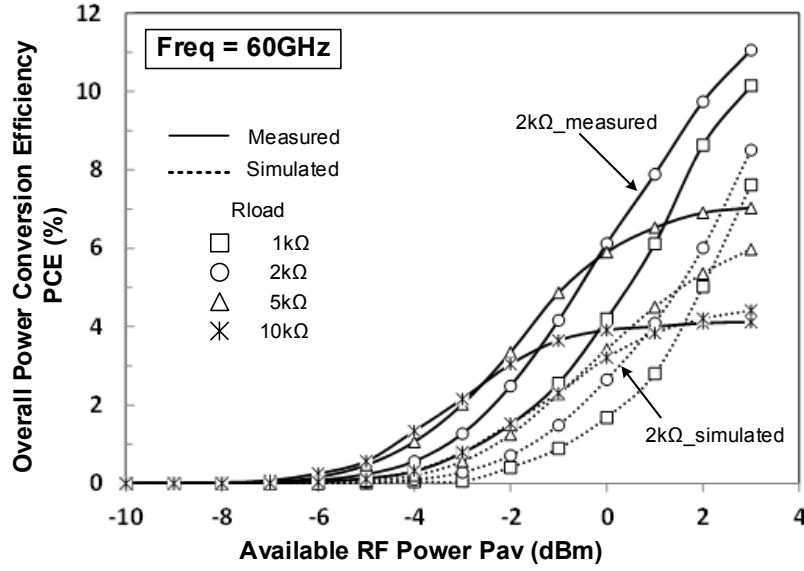


(a)

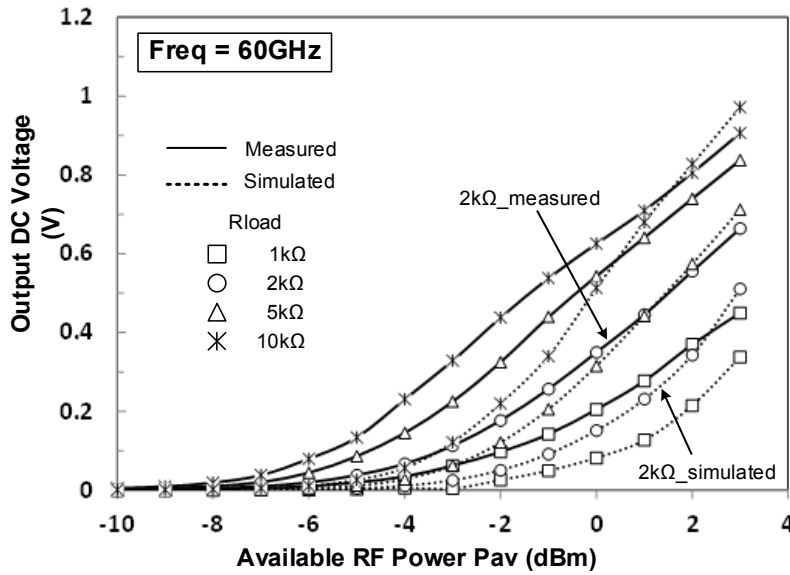


(b)

Figure 3.6: Measured and simulated results at 35 GHz. (a) PCE versus P_{av} , (b) dc voltage versus P_{av} .



(a)



(b)

Figure 3.7: Measured and simulated results at 60 GHz. (a) PCE versus P_{av} , (b) dc voltage versus P_{av} .

Figures 3.5 (b), 3.6 (b) and 3.7 (b) show that at any frequency, the output dc voltage increases with the load resistance. This stems from the fact that a higher resistance draws less charge from C_{load} , which then maintains a higher voltage. This also explains why the PCE is lower

with a larger load resistance, when P_{av} is in the upper range in Fig. 3.5 (a), 3.6 (a), and 3.7 (a). The larger dc potential (with a larger resistance) at the drain terminal of M3, M4 (Fig. 3.3 (a)) induces a higher reverse leakage current when either of these transistors is supposed to be OFF. This mechanism is less severe in the lower range of P_{av} , where the losses due to currents into the transistors' channel resistances predominate. The lower load resistance then implies larger currents, translating into a lower efficiency in the lower range of P_{av} .

The PCE decreases as frequency increases, because the losses through the MOS capacitances increase with frequency, and their decreasing reactance reduces the transistors' drain currents, thus reducing the charging of C_{load} .

To enhance PCE at lower available power, external threshold voltage cancellation techniques, such as what is proposed in [14] or zero-threshold voltage transistors as in [36], should be used for lower diode drop. However, external V_{th} cancellation or zero- V_{th} transistors come with a price of larger reverse leakage current, hence drastically decreasing PCE at medium and high available power (above 0 dBm, a range of interest for the proposed MMID tag). An improved cross-coupled bridge structure as reported in [16] that combines zero- V_{th} transistors to lower turn-on voltage, and four additional switches for reverse leakage current cancellation, should significantly improve PCE over a wider available power range (low, medium, and high P_{av}). However, a technology that includes zero- V_{th} RF model transistors is required.

From Fig. 3.5, 3.6, and 3.7, we can deduce a maximum measured overall PCE of 20%, 18%, and 11% at 24-, 35-, and 60-GHz, respectively, under a load resistor of 1 k Ω for 24 and 35 GHz, and 2 k Ω for 60 GHz. Assuming an on-chip tag antenna of 6 dBi gain [13] and a conservatively low RF power of 1 W EIRP (higher power will extend tag-reader communication range) transmitted from the reader, these rectifier characteristics demonstrate the feasibility of a fully-integrated batteryless MMID tag with the downlink parameters (approximated using Friis equation) and measured rectifier performances given in Table 3.1.

Note that the values in Table 3.1 assume a perfect line-of-sight alignment of reader and tag antenna beams. Any misalignment will result in conditions that deviate from the power budget associated to the values presented in Table 3.1.

Table 3.1: Possible link budget and dc operation condition of the proposed MMID tag.

Powering RF Frequency (GHz)		24	35	60
Transmitted RF Power from the MMID Reader (EIRP)		1W	1W	1W
Communication Range (cm)		3	2	1.8
MMID Tag Antenna Gain (dBi)		6	6	6
Available RF Power at the MMID Tag Antenna (dBm)		6.41	6.66	3
Rectifier Output Load ($k\Omega$)		1	1	2
Measured Rectifier Power Conversion Efficiency (%)		20	18	11
DC Output	V_{DC} (V)	0.92	0.9	0.67
	I_{DC} (μA)	950	927	332
	P_{DC} (μW)	874	834	222.5

In the conditions associated to the PCE maxima values in Table 3.1, the simulated input S-parameters (S11) are -4.2, -5, and -6.5 dB at 24, 35, and 60 GHz respectively, and measured S11 are -5, -7, and -10 dB at 24, 35, and 60 GHz respectively.

Note also that the measured results include the parasitic capacitances of the rectifier input pads. Impedance matching between the antenna and the rectifier should improve power transfer. However, careful trade-off is required since matching circuit losses are significant at mm-wave frequencies and should be taken into account.

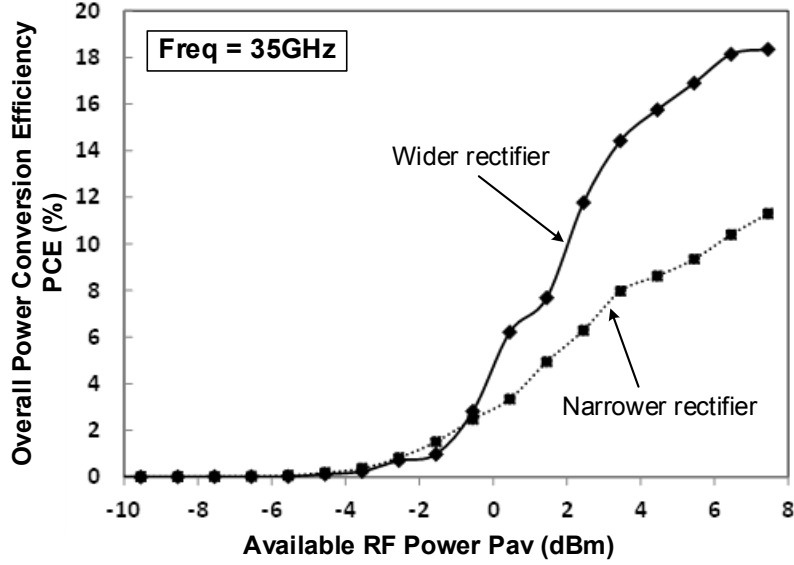


Figure 3.8: Measured PCE results in connection with the transistor and capacitor sizing.

As can be seen in Fig. 3.8, compared to our design variant using narrower transistors with smaller parasitic capacitances and smaller leakage current, our design variant with wider transistors (with higher I_{sat}) proved to be a better design centering for best efficiency as a function of the trade-offs discussed in Section III.

3.5 Conclusion

A millimeter-wave rectifier for batteryless active MMID tag, which can be remotely powered by a reader, has been designed and implemented in 65-nm CMOS technology. In addition to the small on-resistance and small leakage current achievable with a cross-coupled differential circuit, reducing transistor parasitic capacitances, series capacitor losses, and coupling between the on-chip metal lines are key factors for millimeter-wave rectifiers using a bulk CMOS process. The proposed rectifier achieves a PCE of 20% at 24 GHz, 18% at 35 GHz, and 11% at 60 GHz, under 6 dBm power driving for 24 and 35 GHz, and 3 dBm power driving for 60 GHz. These new results support the feasibility of the MMID Reader-Tag system proposed in this paper (Fig. 3.2), employing a batteryless “active” tag that is fully integrated on a single CMOS die, with no substrate, no die-attach and no wiring.

**CHAPTER 4 ARTICLE 2: LOW-POWER INJECTION-LOCKED
ZERO-IF SELF-OSCILLATING MIXER FOR HIGH GBIT/S DATA-
RATE BATTERY-FREE ACTIVE μ Rfid TAG AT MILLIMETER-WAVE
FREQUENCIES IN 65-NM CMOS**

Pascal Burasa, Nicolas G. Constantin, and Ke Wu

Published in the *IEEE Transactions on Microwave Theory and Techniques*, vol.64, no. 4, pp.
1055-1065, Apr. 2016

In this paper, a low-power zero-IF self-oscillating mixer (SOM) for a new generation of high data-rate battery-free, yet active μ Rfid tag (a fully integrated RFID tag on a single CMOS die with no external components nor packaging) operating at millimeter-wave frequencies is proposed and demonstrated. It exploits, on one hand the intrinsic mixing properties of an LC cross-coupled VCO, and on the other hand the injection-locking properties in oscillators. By injection-locking the SOM's natural oscillation frequency to the reader's carrier frequency (a frequency that bears information of the tag: reader-to-tag communication), it enables a direct-conversion to the baseband with no external LO source (self-mixing) nor RF frequency conversion into IF frequency, therefore significantly reducing its power consumption. Up-link communication (tag-to-reader communication) is performed by up-converting the tag's data using the same SOM. Furthermore, the in-phase injected energy stabilizes the self-generated LO and enhances the SOM phase noise, resulting into a low-phase noise baseband signal.

Using a standard 65-nm CMOS process, a 40 GHz zero-IF self-oscillating mixer was designed, fabricated, and tested. Experimental results exhibit a conversion loss of about 30 dB under -38 dBm injected RF power, with a power consumption of only 280 μ W during reader-to-tag communication, and 580 μ W during tag-to-reader communication.

4.1 Introduction

Driven by the ever-increasing needs, radio frequency identification (RFID) has attracted much attention as evidenced by a large variety of its applications in our everyday life, ranging from security, access control, monitoring, etc..., to biomedical systems [37]-[40]. Typically, low RF frequencies (below 3 GHz) have been used for RFID communications and applications. The main factors impeding the evolution of RFID technology over these RF bands are the limited available bandwidth resources and the large tag size (mainly dominated by antenna size at these frequencies and by the battery if active tags are considered). However, the emerging millimeter-wave identification (MMID) technology is set out to exploit smaller antenna size and larger available bandwidths in order to alleviate these limitations [19], [23]. Integrating the tag's antenna on a single-chip (feasible at millimeter-wave frequencies thanks to smaller antenna size), wirelessly harvesting sufficient dc power from incoming millimeter-wave signals (thereby providing an energy autonomy without the need of a battery and at the same time allowing miniaturization), and transmitting data to the reader over a large bandwidth at millimeter-wave frequencies will lead to the development of a new generation of high data-rate, battery-free μ RFID technology for applications that cannot be made possible today. In parallel, this MMID concept is fully compatible with upcoming and future applications of millimeter-wave technology in wireless communications such as 5G technologies and systems that are being discussed and developed worldwide.

Significant progress has been made for on-chip antennas with high gain [31]. Energy can now be efficiently and wirelessly harvested even at millimeter-wave frequencies, as demonstrated in [41]. In addition, extremely low-power CMOS circuit design and techniques for RFID applications have been extensively studied and reported [32]-[34], [42]. However, ultra-low-power and low-complexity millimeter-wave CMOS transceivers relying only on a rectified dc power remain a challenging problem and not demonstrated in the above-mentioned high data-rate MMID context. In our opinion, self-oscillating mixer (SOM) techniques present an adequate candidate for such low-power millimeter-wave transceivers, since they combine both oscillator and mixer functionalities into a single device and under a single bias current. So far, published works on SOMs [43]-[46] convert, first of all, the RF frequency into an IF frequency and thereafter filter out frequencies other than IF signal. This requires extra dc power consumption associated to the IF

processing. They are intended for applications with significantly higher power consumption than what is required in self-powered active MMIDs.

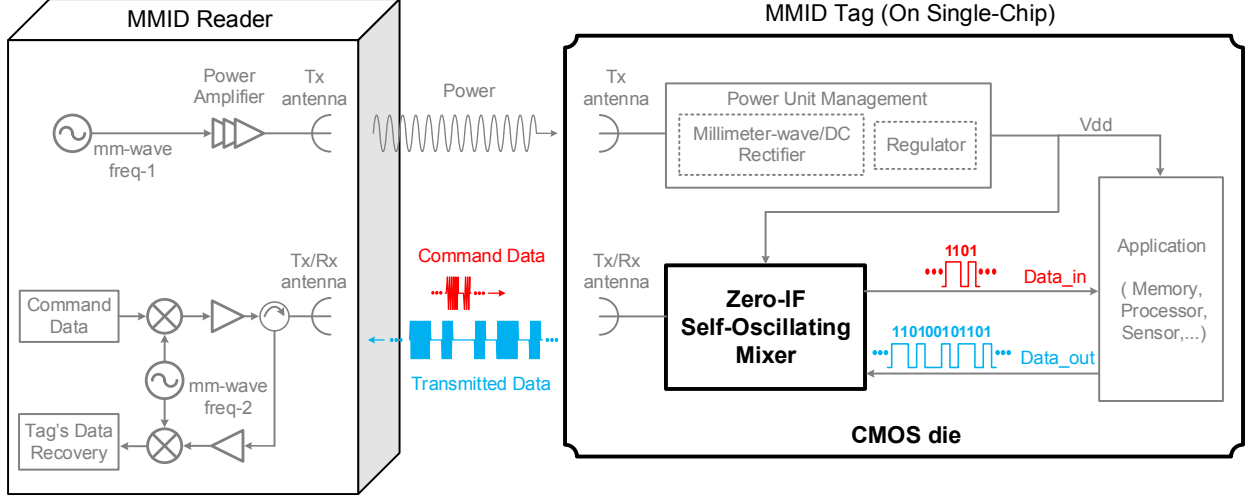


Figure 4.1: Block diagram of a recently proposed MMID system with a battery-free active tag on single-chip.

On the basis of our previous work [47], more details and analysis of a zero-IF self-oscillating mixer that performs both millimeter-wave receiver and transmitter mixing functions using only one device is proposed and demonstrated. As illustrated in Fig.4.1, which represents a newly proposed MMID reader-tag system [41], the proposed mixer is a key circuit block that renders possible the implementation of a battery-free active tag, fully integrated on single CMOS die. From Fig.4.1, a reader simultaneously shines a tag or multiple tags with two tones at millimeter-wave frequencies. *freq-1*, a continuous wave (CW), goes to the millimeter-wave-to-dc rectifier and supplies energy to the tag. The reader and the tag therefore exchange highly secured data at a high bit-rate on the *freq-2* carrier without compromising the tag's energy, regardless of the type of modulation or coding. During reader-to-tag communications, the SOM is injection-locked to *freq-2*, enabling a direct-conversion to baseband without any external *LO* source and no additional IF processing, thereby significantly reducing power consumption. Besides, the poor phase noise associated with the SOM's low-bias current is mitigated by the injection-locking signal since the SOM's phase noise follows that of the injected signal [48], [49]. For the tag-to-reader

communication, the tag's data are up-converted and transmitted using the same SOM as illustrated in Fig.4.1. A measured conversion loss of about 30 dB under -38 dBm injected RF power, with only 580 μ W dc power consumption, supports the feasibility of the MMID reader-tag system proposed in this paper (Fig.4.1).

Section II of this paper presents the operating principles of the proposed self-oscillating mixer. Section III analyzes the mixing mechanism of the SOM, and section IV presents and discusses the measurement setup and results.

4.2 Operating Principles of the Proposed Zero-IF SOM Circuit

As illustrated in Fig.4.2, during reader-to-tag communications, a reader sends an AM modulated signal RF_{inj} , carrying information to either write in the tag or interrogate the tag. In addition, the RF_{inj} signal accomplishes three key functions. First, having the same frequency as the natural oscillation frequency of the SOM, i.e. $f_{RF} = f_{LO}$, RF_{inj} injects an in-phase energy into the SOM, which relaxes the negative resistance required to compensate the SOM losses, and therefore triggers and starts LO oscillation with lower power consumption. Second, with $f_{RF} = f_{LO}$, RF_{inj} locks LO to its carrier frequency f_{RF} , allowing a direct-conversion to baseband, given that LO and RF_{inj} are self-mixed. Third, by injection-locking LO , RF_{inj} maintains a phase coherence between both signals, which enhances the SOM phase noise, as well as the phase noise of the down-converted baseband signal. The mixing function is performed by the cross-coupled pair transistors M2 and M3, thanks to their time-varying transconductances gm , as illustrated in Fig.4.4. The down-converted baseband is extracted at the common node V_{CM} . Ideally, even harmonics are in-phase and therefore sum-up at V_{CM} , but are filtered out by capacitor $C1$, whose self-resonance suppresses entirely $2f_{LO}$. The odd harmonics and the fundamental are out of phase and therefore cancel out each other at V_{CM} (self-filtering) [50]. Hence V_{CM} is a virtual ground at RF frequencies. Note, however, that our circuit topology (Fig. 4.2) presents a high impedance at the baseband frequency, thus allowing a baseband amplification at the output for zero-IF mixing. This constitutes a fundamental circuit technique difference with other self-mixing oscillators proposed so far (e.g. [43]).

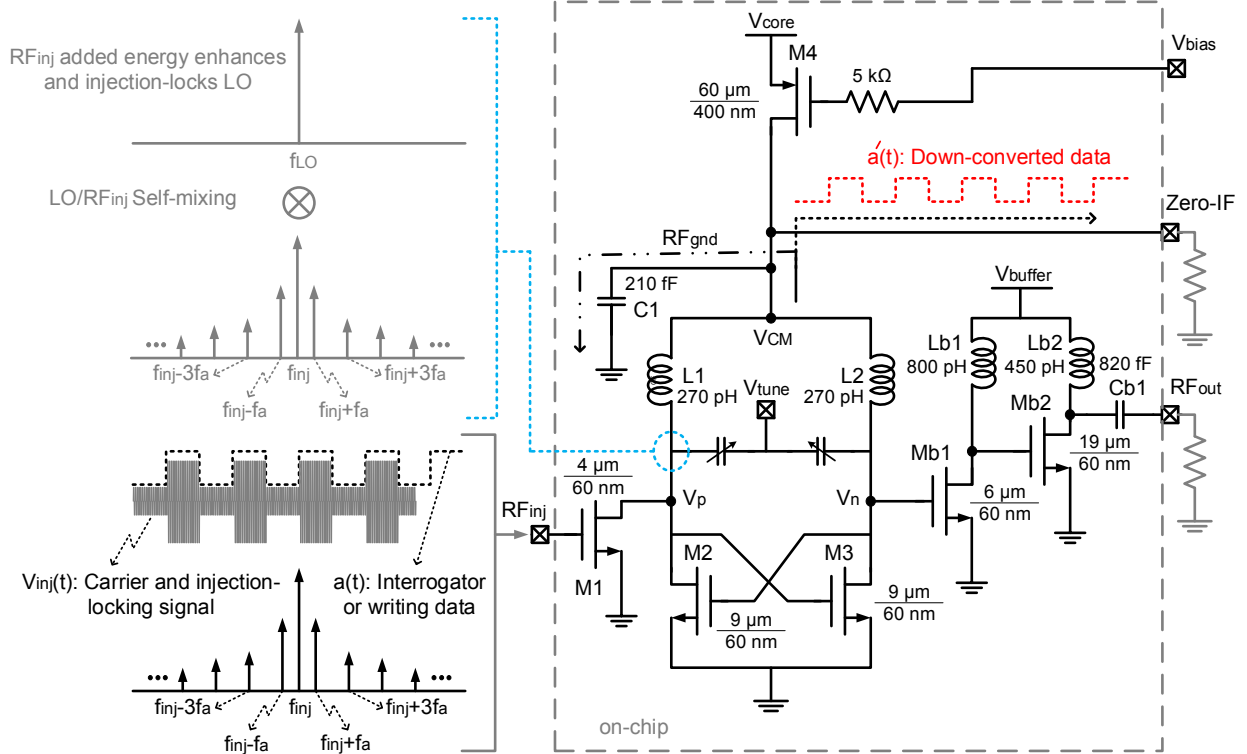


Figure 4.2: Operation principles of the proposed zero-IF SOM.

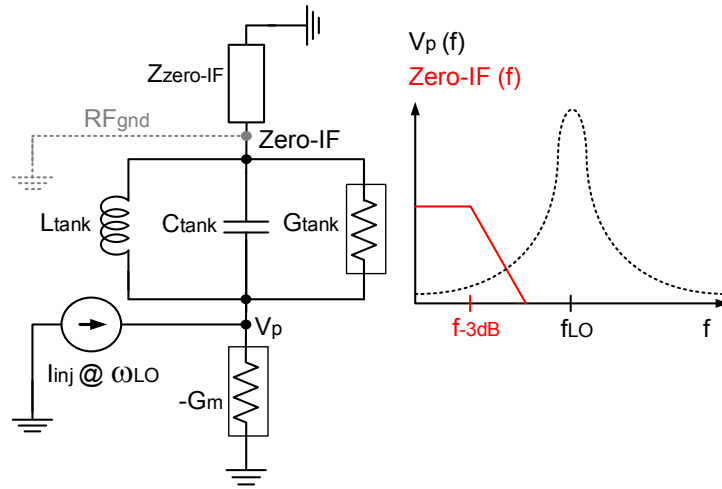
During tag-to-reader communications, an injection-locking of the SOM is maintained, but with a constant-amplitude millimeter-wave RF_{inj} signal coming from the reader (Fig. 4.2). The tag injects its data (from its memory, sensor...) into the mixer by summing the data signal with RF_{inj} and varying the gate voltage and drain current of transistor M1 at the baseband frequency, hence varying the operating conditions of M2, M3 at the baseband frequency during the injection-locking. It results in the modulation of the RF current intensities through M2, M3. This has the effect of a multiplication of the LO signal amplitude by the baseband information. The binary data is therefore up-converted through ASK modulation. As illustrated in Fig. 4.2, the up-converted signal is sensed at the output node V_n by an RF buffer comprising $Mb1$, $Mb2$, $Lb1$, $Lb2$, and $Cb1$. The output RF_{out} is matched to 50Ω for measurements purpose, but is intended to be matched to the transmitting antenna.

Unlike a symmetric injection-locked frequency divider where mixing function is mainly performed by the input transistor, the proposed SOM topology allows the input transistor (M1) to

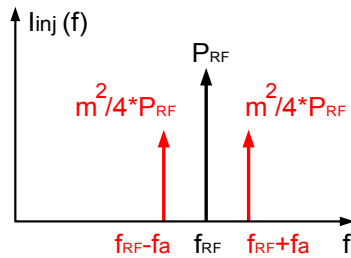
act as a transimpedance amplifier, therefore it can receive and inject a small RF_{inj} signal into the tank.

4.3 Analytical Expressions for Zero-IF SOM Operation

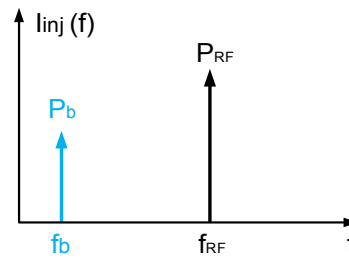
In this section, we first analyze the self-oscillating mixer's conversion gain as a function of circuit design parameters, dc power consumption, and the injected signal parameters such as the modulation index m (during reader-to-tag communications), then we analyze the trade-off between up-converted sidebands power levels and circuit design parameters, as well as the dc power consumption (during tag-to-reader communications).



(a)



(b)



(c)

Figure 4.3: (a) Zero-IF SOM simplified model, (b) spectrum of the injected $RFinj$ signal during reader-to-tag communication, (c) spectrum of $RFinj$ signal during tag-to-reader communication.

Fig.4.3 (a) depicts a simplified SOM model used in this section. Components are approximated as:

$$L_{\tan k} \approx L_1 + L_2 \quad (4.1)$$

$$C_{\tan k} \approx C_{\text{var}} + C_{\text{par}} \quad (4.2)$$

$$G_{\tan k} \approx G_{\text{var}} + G_{\text{par}} + R_s / (\omega_{LO} L_{\tan k})^2 \quad (4.3)$$

$$f_{LO} = \frac{1}{2\pi \sqrt{L_{\tan k} C_{\tan k}}} \quad (4.4)$$

where $L_{\tan k}$ (the loading inductance) and $C_{\tan k}$ (the loading capacitance) form the resonator, f_{LO} is the natural oscillation frequency of the SOM, $G_{\tan k}$ represents the total tank losses, C_{var} is the varactor capacitance, R_s is the inductor series resistance, and C_{par} represents the total parasitic capacitance that loads the tank. As illustrated in Fig.4.4, the total parasitic capacitance is mainly dominated by parasitic capacitors of the cross-coupled pair transistors M2 and M3, and the parasitic capacitors of the loading transistor M1 and output buffer transistor *Mb1* (Fig.4.2). The negative transconductance – G_m performs two functions: first, it provides a negative resistance to compensate the tank losses and therefore allows a sustained oscillation. Second, as the cross-coupled pair transistors M2 and M3 act as switches, they intrinsically perform the mixing function (self-mixing).

In the receiving mode (when the SOM is used to demodulate the millimeter-wave signal from the reader), corresponding to the frequency spectrum in Fig.4.3 (b), the injected current I_{inj} is an AM modulated signal, with a carrier frequency f_{RF} that locks the SOM and sidebands frequency contents ($f_{RF} \pm f_a$) bearing the information to be recovered by the tag (m is a modulation index).

In the transmitting mode (when the SOM is used to up-convert the baseband information to be sent to the reader), the injected current I_{inj} is the sum of the RF signal from the reader at frequency f_{RF} for injection-locking and the data signal from the tag at baseband frequency f_b . The corresponding frequency spectrum is illustrated in Fig.4.3(c). In both modes, the modulating signals at baseband frequencies f_a and f_b are considered as sinusoidal signals to simplify the analyses in the next section.

4.3.1 Conversion Gain of SOM: Reader-to-Tag Communication

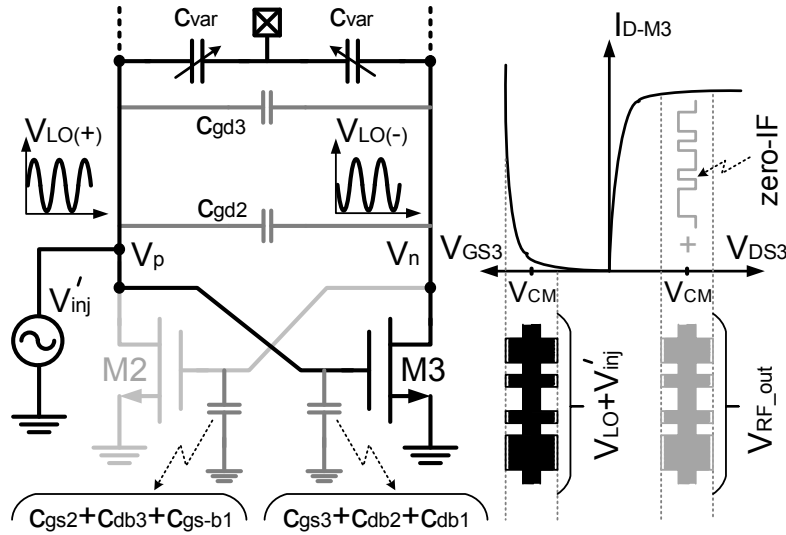


Figure 4.4: Operating condition of cross-coupled pair transistors when biased close to their threshold voltage and their respective parasitic capacitors.

Assuming that

$$V_{RF}(t) = V_{RF} \sin(\omega_{RF}t) \quad (4.5)$$

is the injection-locking carrier signal from the reader,

$$a(t) = V_a \sin(\omega_a t) \quad (4.6)$$

is the data signal for the tag and

$$V_{LO}(t) = V_{LO} \cos(\omega_{LO}t) \quad (4.7)$$

is the generated LO signal (the SOM natural oscillation frequency). V_{RF} and ω_{RF} , V_a and ω_a , and V_{LO} and ω_{LO} are the amplitudes and frequencies for the above defined signals. The received signal from the reader can be expressed as:

$$V_{inj}(t) = V_{AM}(t) = V_{RF} \sin(\omega_{RF}t) + \frac{V_a}{2} \cos(\omega_{RF} - \omega_a)t - \frac{V_a}{2} \cos(\omega_{RF} + \omega_a)t \quad (4.8)$$

The received AM modulated signal (4.8) injects a current:

$$i_{inj}(t) = gm_1 V_{inj}(t) \quad (4.9)$$

into the tank through the transistor M1 which acts as a transimpedance amplifier, gm_1 being its small signal transconductance. As illustrated in Fig.4.4, the injected current (4.9) in return injects a voltage:

$$V'_{inj}(t) = [gm_1 V_{inj}(t)] Z_{tan k} \quad (4.10)$$

across the tank. Assuming that the SOM is locked by $V_{inj}(t)$ since $\omega_{RF} = \omega_{LO}$

$$Z_{tan k} \big|_{\omega_{RF}} \approx \text{Re}(Z_{tan k}) = R_{tan k} \quad (4.11)$$

and equation (4.10) becomes

$$V'_{inj}(t) \approx (gm_1 R_{\tan k}) V_{inj}(t) \quad (4.12)$$

As shown in Fig.4.4, the total voltage across the tank has two components: one is $V_{LO}(t)$, at frequency ω_{LO} and which is generated by the SOM under injection-locking, and the other is the AM modulated signal $V'_{inj}(t)$ centered at $\omega_{RF} = \omega_{LO}$. The modulated gate-source voltage periodically swings M2, M3 transistors forth and back between the saturation and triode region. Frequency mixing occurs due to the modulation of transconductances $gm_{2,3}$ of M2 and M3 transistors. The quiescent gate-source voltages of pair transistors M2 and M3 are close to the threshold voltage $V_{GS2,3} = V_{CM} \approx V_{th2,3}$, a region where $gm_{2,3}$ is the most sensitive (nonlinear variations) to the externally injected RF_{inj} signal. Note that, to simplify the analysis, M2 and M3 junction capacitances are not taken into account since they have a small variation range. The output conductances $gd_{2,3}$ are also neglected, given the fact that $V_{CM} \gg V_{DS-sat2,3}$, ($V_{DS-sat2,3}$ being the saturation drain-source voltage of M2, M3) hence the output conductance $gd_{2,3}$ has much less contribution to mixing over transconductances $gm_{2,3}$. It is also worth noting that, since $V_{CM} \gg V_{DS-sat1}$ and $V_{inj}(t)$ of (4.8) is considered as small signal, transistor M1 remains in the saturation region and permanently injects current $i_{inj}(t)$ of (4.9) into the tank. Drain current, for example i_{D3} of M3 as illustrated in Fig.4.4, can be expressed as:

$$i_{D3} = \beta_3 (v_{GS3} - V_{th3})^2 \quad (4.13)$$

With

$$\beta_3 = \frac{1}{2} \mu_n C_{ox} \frac{W_3}{L_3} \quad (4.14)$$

$$v_{GS3} = V_{CM} + v'_{inj} + v_{LO} \quad (4.15)$$

β_3 is the transconductance parameter of M3, V_{CM} is the dc bias voltage at the common node (M2, M3 drains), v'_{inj} and v_{LO} are defined in (4.12) and (4.7) respectively, and V_{th} is the threshold voltage. Replacing (4.15) into (4.13), the drain current i_{D3} can be approximated as:

$$i_{D3} = \beta_3 \left[(V_{CM} - V_{th})^2 + 2(V_{CM} - V_{th})(v'_{inj} + v_{LO}) + (v'_{inj})^2 + v_{LO}^2 + 2v'_{inj}v_{LO} \right] \quad (4.16)$$

with the mixing term:

$$M_x = 2\beta_3 v'_{inj} v_{LO} \quad (4.17)$$

Replacing v'_{inj} in (4.17) by (4.12),

$$M_x(t) = 2\beta_3 g m_1 R_{\tan k} V_{inj}(t) V_{LO}(t) \quad (4.18)$$

Replacing $V_{inj}(t)$ and $V_{LO}(t)$ in (4.18) by (4.8) and (4.7) respectively, the mixing term can be derived as:

$$= 2\beta_3 g m_1 R_{\tan k} \left[\begin{array}{l} \left(V_{RF} \sin(\omega_{RF} t) + \frac{V_a}{2} \cos(\omega_{RF} - \omega_a) t \right) \\ - \frac{V_a}{2} \cos(\omega_{RF} + \omega_a) t \\ (V_{LO} \cos(\omega_{LO} t)) \end{array} \right] \quad (4.19)$$

By expanding (4.19) through trigonometric identities, it may be shown that, besides the down-converted baseband signal, the drain current i_{D3} also contains the fundamental, up-converted sidebands, and second order harmonics of the RF signal. The resonator filters out higher order harmonics, and the virtual ground at V_{CM} in Fig. 4.2 filters out the second order harmonic and its up-converted sidebands, but the circuit topology also allows a baseband signal amplification at the zero-IF output (at V_{CM}). Accordingly, after the expansion of (4.19) and considering only the mixing terms that contain the information signal $a(t)$, equation (4.19) is simplified to:

$$= 2\beta_3 g m_1 R_{\tan k} \frac{V_a V_{LO}}{4} \left[\cos(2\omega_{RF} - \omega_a)t - 2\cos(\omega_a t) \right. \\ \left. + \cos(2\omega_{RF} + \omega_a)t \right] \quad (4.20)$$

In equation (4.20), it can be observed that the down-converted baseband current (zero-IF current) is expressed as:

$$M_x(t)|_{\text{zero-IF (current)}} = \beta_3 g m_1 R_{\tan k} V_a V_{LO} \cos(\omega_a t) \quad (4.21)$$

with

$$V_{LO} = \frac{I_{LO} \text{Re}(Z_{\tan k})}{2} = \frac{I_{LO} R_{\tan k}}{2} \quad (4.22)$$

By replacing V_{LO} in (4.21) by (4.22), the baseband current of equation (4.21) is derived as:

$$M_x(t)|_{\text{zero-IF (current)}} = \frac{\beta_3 g m_1 (R_{\tan k})^2 V_a I_{LO}}{2} \cos(\omega_a t) \quad (4.23)$$

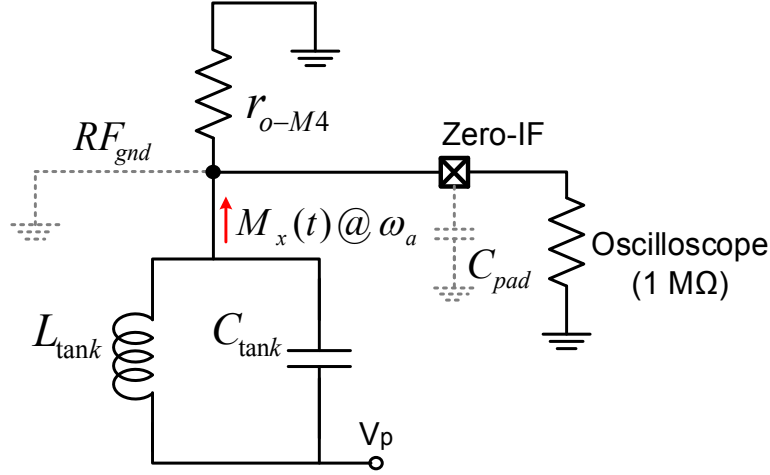


Figure 4.5: Zero-IF current and loading condition.

As discussed earlier, the only voltage across the common node V_{CM} results from the zero-IF current component, expressed by (4.23). Therefore, Fig.4.5 may be used as a small-signal output circuit representation. Any LO leakage due to the asymmetry in the differential outputs (due to layout and process variation) and the unfiltered RF signal at V_{CM} are considered as noise, and determine the lower detectable limit of the down-converted baseband. From Fig.4.5, then, transistor M4 operates simultaneously as a current source for the SOM and an active load for the down-converted baseband signal. Assuming that the parasitic capacitance at V_{CM} is small and has less impact on the baseband frequency, the zero-IF voltage can be defined as:

$$M_x(t)|_{zero-IF(voltage)} = (M_x(t)|_{zero-IF(current)}) (r_{o-M4}) \quad (4.24)$$

With

$$r_{o-M4} = \frac{1}{\lambda_4 \left[\frac{1}{2} \mu_p C_{ox} \frac{W_4}{L_4} (V_{SG4} - V_{th4})^2 \right]} \quad (4.25)$$

$$r_{o-M4} \approx \frac{1}{\lambda_4 I_{D4}} \quad (4.26)$$

where λ_4 is the channel-length modulation of the transistor M4. Combining (4.23) and (4.26), the down-converted zero-IF voltage $a'(t)$ of (4.24) can be written as:

$$a'(t) = \frac{\beta_3 g_{m1} (R_{\tan k})^2 V_a I_{LO}}{2 \lambda_4 I_{D4}} \cos(\omega_a t) \quad (4.27)$$

Small tuning varactors are used only to compensate small frequency variations because of process and temperature variations. Hence the tank quality factor $Q_{\tan k}$ is mainly dominated by the inductor losses, and we can approximate:

$$Q_{\tan k} \approx Q_L \Leftrightarrow R_{\tan k} \approx Q_L^2 R_S \quad (4.28)$$

Replacing $R_{\tan k}$ in (4.27) by (4.28), the recovered baseband signal can be expressed as:

$$a'(t) = \frac{\beta_3 g_{m1} Q_L^4 R_s^2 V_a I_{LO}}{2 \lambda_4 I_{D4}} \cos(\omega_a t) \quad (4.29)$$

Voltage conversion gain can be deduced from the ratio between the amplitude of the down-converted baseband $a'(t)$ and the amplitude of the injected carrier signal $V_{RF}(t)$ as:

$$CG = \frac{|a'(t)|}{|V_{RF}(t)|} = \frac{\beta_3 g_{m1} Q_L^4 R_s^2 V_a I_{LO}}{2 \lambda_4 I_{D4} V_{RF}} \quad (4.30)$$

For the purpose of this analysis, we define the modulation index of the injected signal m as:

$$m = \frac{V_a}{V_{RF}} \quad (4.31)$$

The conversion gain in equation (4.30) may then be estimated by

$$CG = \frac{|a'(t)|}{|V_{RF}(t)|} = \frac{\beta_3 gm_1 Q_L^4 R_s^2 I_{LO} m}{2\lambda_4 I_{D4}} \quad (4.32)$$

According to (4.32), apart from the fact that increasing the inductor quality factor pushes the conversion gain up, this gain is also dependent on a design trade-off, function of the channel length modulation coefficient of the PMOS current source (M4), its bias current, the bias current of M3 (through parameter β_3) and the amplitude V_{LO} of the oscillator's signal (related to I_{LO} by (4.22)). For example: 1) to increase CG through β_3 , larger W_3 may be used, resulting in higher quiescent current I_{D_M3} , until the point where any further increase of I_{D_M3} will cause I_{D_M4} (which supplies M2,M3) to be high enough to start reducing CG again. Besides, note that a larger W_3 induces more losses and that may cause the insufficient loop gain to start oscillation; 2) gm_1 can be enhanced by increasing the overdrive voltage ($V_{GSI}-V_{th1}$) or larger W_1 , again implying a more power consumption, and 3), increasing I_{LO} implies an increase of dc power consumption as well. To the other extremity, a certain minimum of dc current is needed to guarantee sufficient $gm_{2,3}$ in order to meet the SOM startup condition. Besides the trade-offs between CG and dc power, equation (4.32) reveals that once bias conditions are set, the SOM conversion gain is proportional to the modulation index m , as defined in (4.31) for the injected and modulated signal $V_{inj}(t)$, independently of its carrier signal power. In other words, once the SOM is injection-locked, any additional injected power but with no increase in modulation index does not improve the conversion gain.

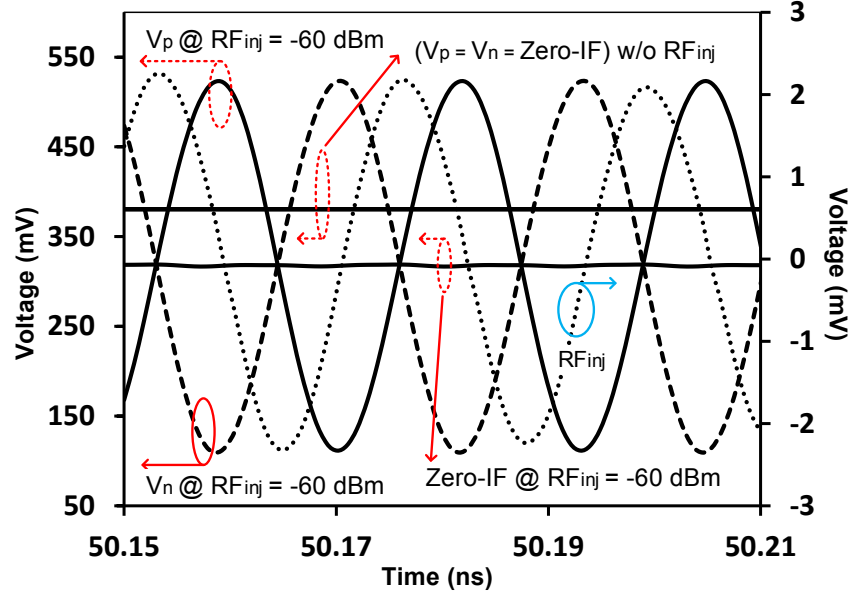
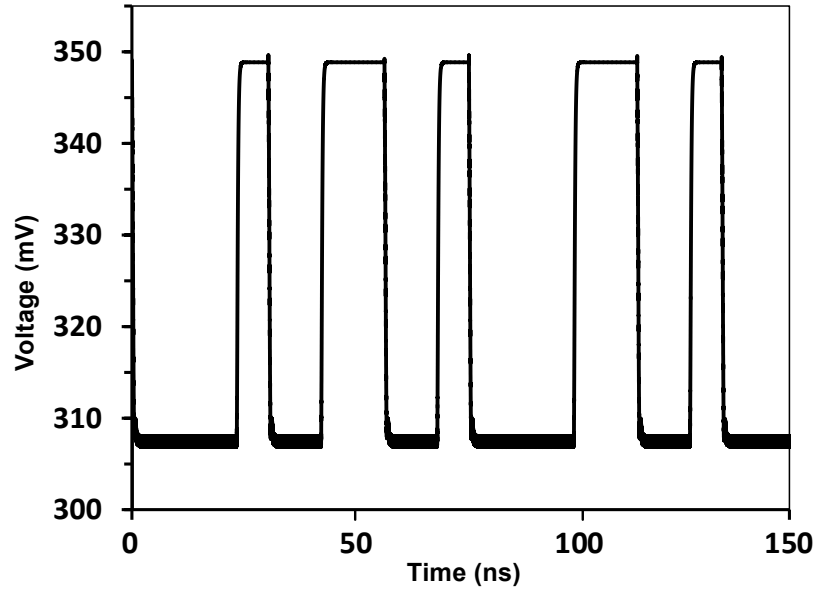
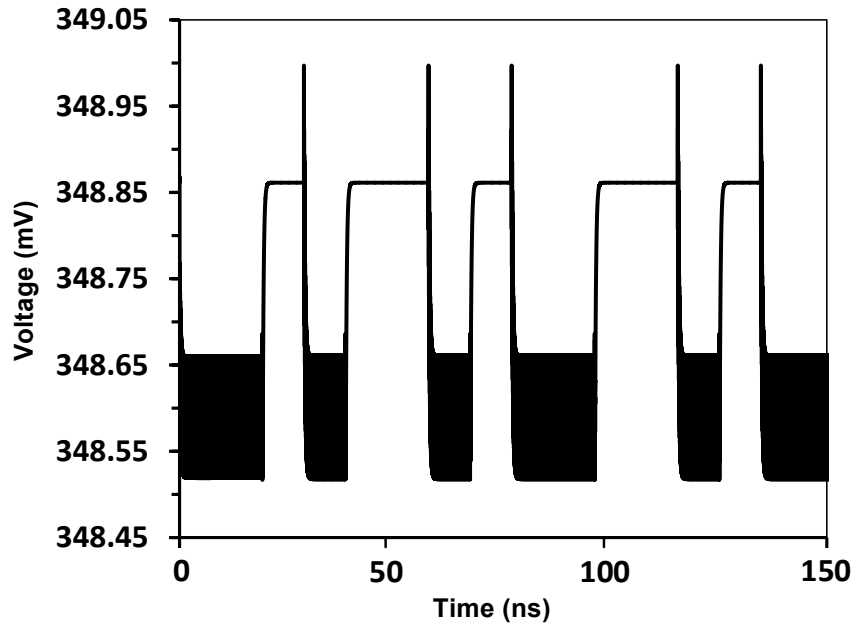


Figure 4.6: Simulated results that demonstrate the operating conditions of the SOM with and without $RFinj$ signal.

Fig.4.6 illustrates the operating conditions of the SOM. An extremely low-power, externally injected in-phase energy ($RFinj$ signal) is required to relax the negative transconductance ($-Gm$) and trigger oscillation. Fig.4.7 shows the down-converted signal at the common node. When $f_{RF} = f_{LO}$, the baseband signal is successfully recovered (Fig.4.7 (a)). However, when $f_{RF} \neq f_{LO}$, the output is a noise of low-frequency components (Fig.4.7 (b)).



(a)



(b)

Figure 4.7: Simulated results of the recovered (down-converted) baseband signal at zero-IF output pad, when an AM signal, modulated by a random signal, is injected into the SOM.

4.3.2 Up-Converted Sideband Power of SOM: Tag-to-Reader Communication

The tag communicates back to the reader by up-converting its data:

$$b(t) = V_b \cos(\omega_b t) \quad (4.33)$$

Using the SOM mixing function. V_b and ω_b are the amplitude and frequency of the baseband signal, respectively. In consistent with the frequency spectrum in Fig.4.3 (c), the injected signal can be expressed as:

$$V_{inj}(t) = V_{RF}(t) + b(t) \quad (4.34)$$

where $V_{RF}(t)$ is, this time, a CW injection-locking signal transmitted by the reader in order to stabilize and keep phase coherence between f_{RF} and f_{LO} . Assuming a linear amplification by M1, the associated CW Drain current in M1 at f_{RF} will induce an RF voltage across the tank only, given the virtual ground at V_{CM} (Fig. 4.2). The baseband component of the Drain current in M1 at ω_b will induce a v_{DS4} voltage across M4 only, given the negligible reactance of L1 at ω_b . Therefore, the injected voltage across the Gate-Source terminals of M3 may be approximated as the sum of these voltages:

$$V'_{inj}(t) = gm_1 [R_{tank} V_{RF}(t) + r_{o-M4} b(t)] \quad (4.35)$$

The mixing term that stems from a quadratic relation between i_{D3} versus v_{GS3} may be derived similarly as for (4.13)-(4.17) and is expressed as:

$$M_x = 2\beta_3 v'_{inj} v_{LO} \quad (4.36)$$

Replacing v'_{inj} in (4.36) by (4.35) yields:

$$M_x(t) = 2\beta_3 g m_1 [R_{\tan k} V_{RF}(t) + r_{o-M4} b(t)] V_{LO}(t) \quad (4.37)$$

By keeping only the second term that contains the information signal $b(t)$,

$$M_x(t)|_{Up-link} = 2\beta_3 g m_1 [r_{o-M4} b(t) V_{LO}(t)] \quad (4.38)$$

which can be expanded to:

$$M_x(t)|_{Up-link} = \beta_3 g m_1 r_{o-M4} V_b V_{LO} \begin{bmatrix} \cos(\omega_{LO} - \omega_b)t \\ + \cos(\omega_{LO} + \omega_b)t \end{bmatrix} \quad (4.39)$$

Combining (4.22), (4.26), and (4.28) with (4.39), the up-converted signal can be approximated by

$$M_x(t)|_{Up-link} = \frac{\beta_3 g m_1 Q_L^2 R_s V_b I_{LO}}{2\lambda_4 I_{D4}} \begin{bmatrix} \cos(\omega_{LO} - \omega_b)t \\ + \cos(\omega_{LO} + \omega_b)t \end{bmatrix} \quad (4.40)$$

Similar to 4.32), equation (4.40) shows that the sideband power can be enhanced by increasing inductor quality factor and dc power consumption.

4.4 Circuit Design and Experimental Results

4.4.1 Chip Design and Measurement Setup

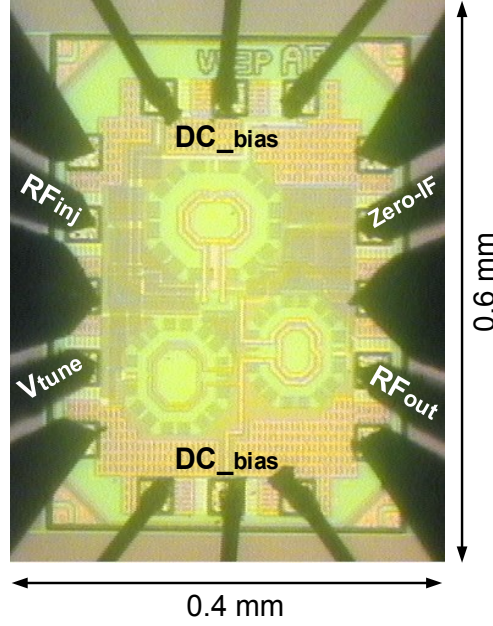


Figure 4.8: Die microphotograph of the fabricated SOM.

The proposed self-oscillating mixer was fabricated using a standard 65-nm CMOS process. Fig.4.8 shows the die microphotograph with an area of $0.4 \times 0.6 \text{ mm}^2$ including RF pads. For a low power design, the layout was optimized to minimize parasitic capacitances and the free-running tuning range was designed to only compensate frequency variations due to process variations. The sizes of M1 and Mb1 transistors were chosen to maintain as much symmetry as possible at the differential output (V_p, V_n). Measurements were carried out on-wafer, and Fig.4.9 (a) shows (at a conceptual level) the measurement setup used. In the receiving mode (during reader-to-tag communications), a power signal generator (Agilent E8257D) that emulates the reader's transmitter sends an AM modulated signal. The recovered data (down-converted baseband) is read by a digital oscilloscope (Agilent DSO-X3034A) with $1 \text{ M}\Omega$ input impedance (emulating a digital

buffer input impedance). In the transmitting mode (during tag-to-reader communications), a CW signal from the same power signal generator (Agilent E8257D) injection-locks the SOM, and another power signal generator (Hewlett-3000A) emulates the tag's data to be transmitted by injecting its data as well via a combiner to the SOM. The up-converted signal is received by a signal analyzer (Agilent PXA N9030A) which emulates the reader's receiver. Fig.4.9 (b) shows a photograph of the measurement setup.

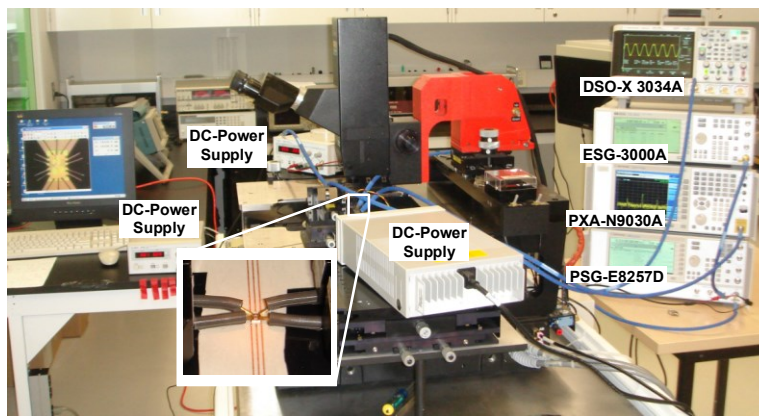
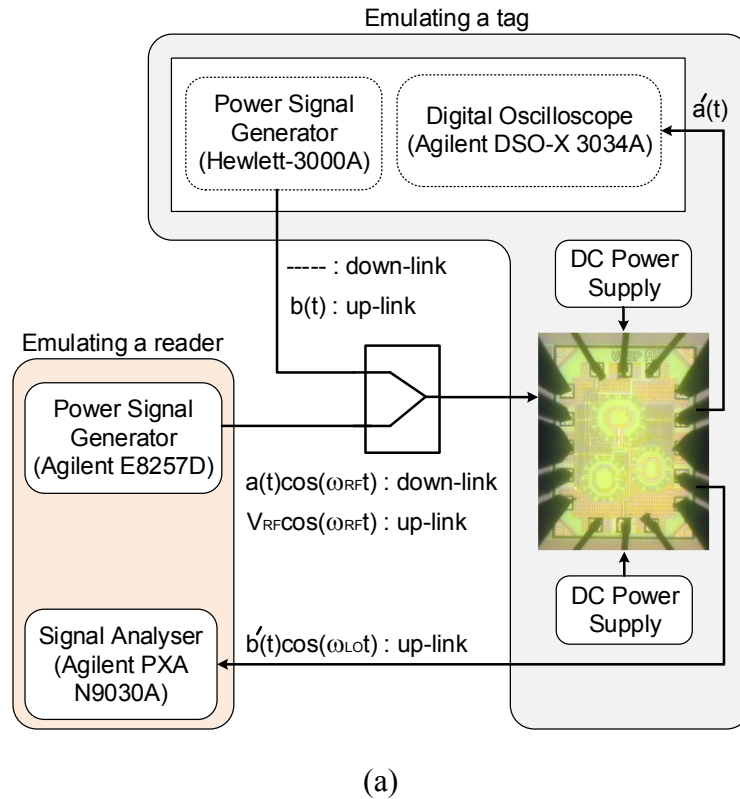


Figure 4.9: (a) measurement setup, (b) photograph of measurement setup and the probe station.

4.4.2 Zero-IF SOM Performances

Measurements were taken under 350 μ A bias current and 800mV supply voltage for the core section (280 μ W), while 500 μ A was drawn by the output buffer from a 600 mV supply. In order to evaluate the SOM injection-locking characteristics, a 40 GHz signal with variable RF power was injected into the SOM through RF_{inj} pad (Fig.4.2), and phase noise was measured at the output pad RF_{out} (Fig.4.2). Fig.4.10 shows that 1) the SOM phase noise is reduced as the power level of RF_{inj} increases, and tends to a comparable phase noise level to that of RF_{inj} . and 2) when the injected power becomes very weak (< -48 dBm in our case), the SOM is no longer locked to the injected signal. Fig.4.10, therefore, confirms the feasibility of using an extremely low-power and low-complexity millimeter-wave SOM with poor free-running phase noise performances to perform zero-IF down-conversion, with significantly enhanced spectral purity performances under injection-locking. This is suitable for transceivers in self-powered and fully-integrated MMID tags (for short range communications).

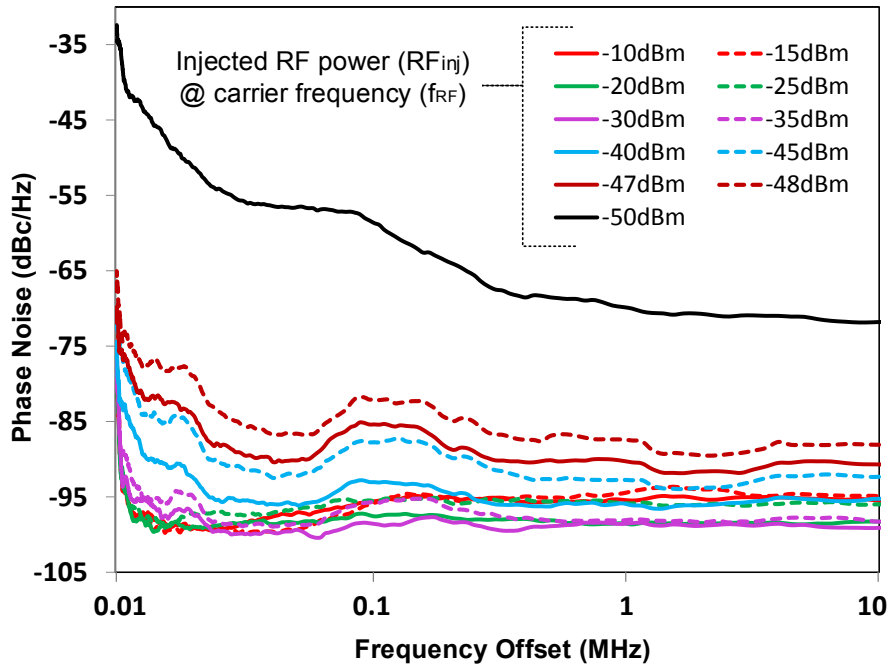
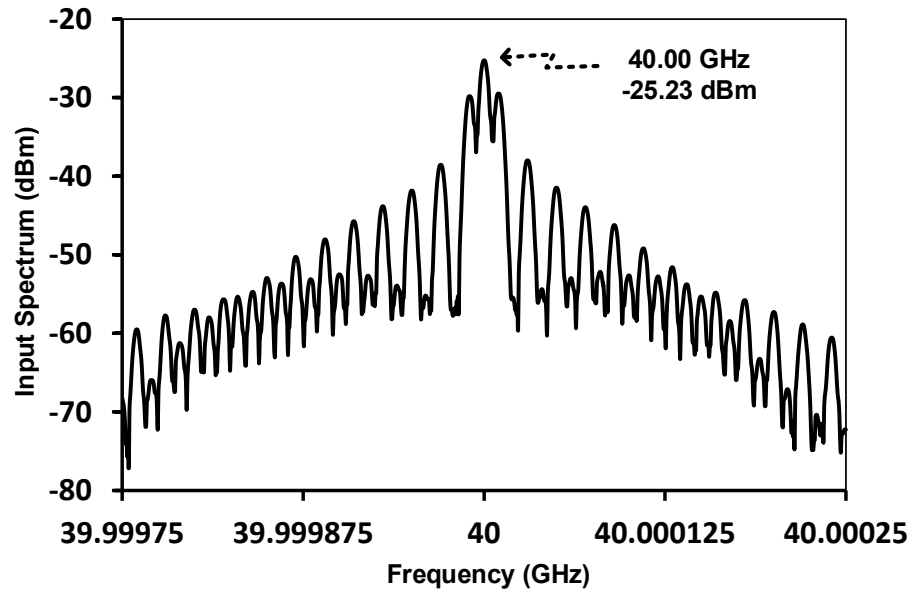
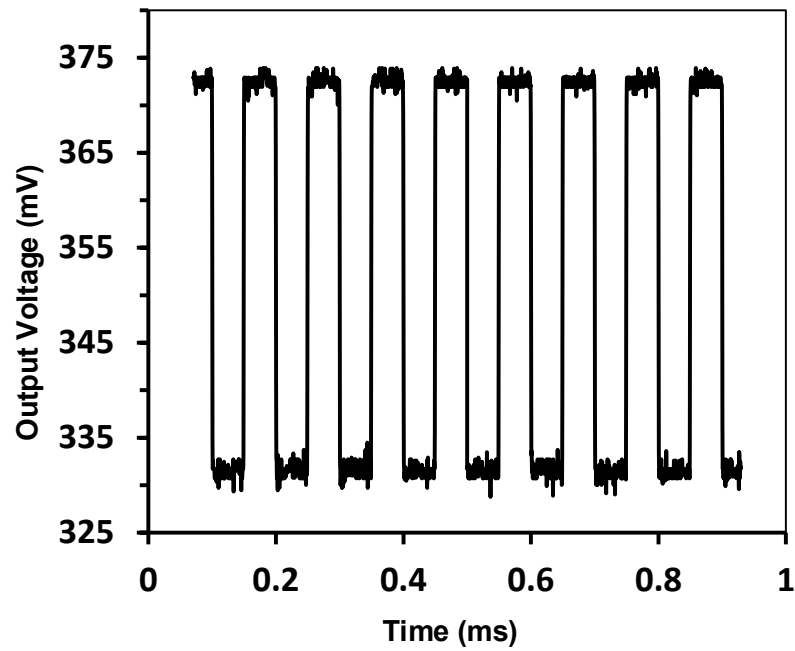


Figure 4.10: SOM phase noise measured at RF_{out} pad for different power levels of the injected RF_{inj} signal.



(a)



(b)

Figure 4.11: (a) Spectrum of AM signal, modulated by a 10-kHz square wave signal, and injected into the SOM at RFinj pad (Res BW 4.7 kHz, VBW 4.7 kHz), (b) recovered down-converted baseband signal measured at zero-IF pad.

Fig.4.11 (a) shows the spectrum of an injected AM signal which is modulated by a 10 kHz square wave. Fig.4.11 (b) shows the measured baseband at the output of the SOM (at the zero-IF pad). The 10 kHz modulating signal has been successfully recovered.

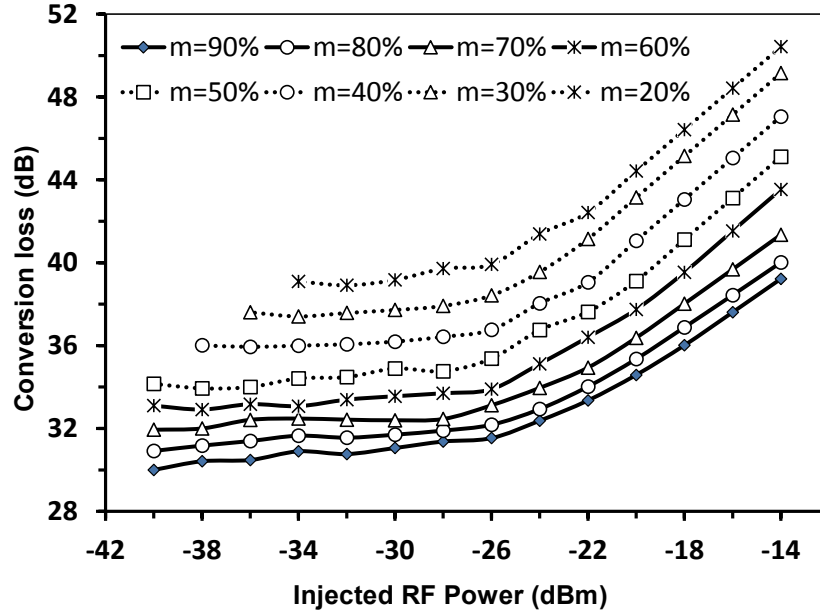


Figure 4.12: Measured conversion loss versus injected power for different modulation index.

Fig.4.12 shows the measured conversion loss when the SOM is injection-locked by an AM modulated signal with 40 GHz carrier frequency, with a variable power and a variable modulation index m . As predicted by (4.32), the results in Fig.4.12, on one hand show that once the SOM is injection-locked, any additional injected RF power is converted into losses rather than enhancing the conversion gain. On the other hand, the results confirm that for a fixed injected power, the conversion loss can be improved by increasing the modulation index of the received AM signal. In addition, the higher the modulation index m is, the better the sensitivity of the SOM is to detect and down-convert weak received signals (in our case $RF_{inj} \approx -40$ dBm when the carrier is 90% modulated).

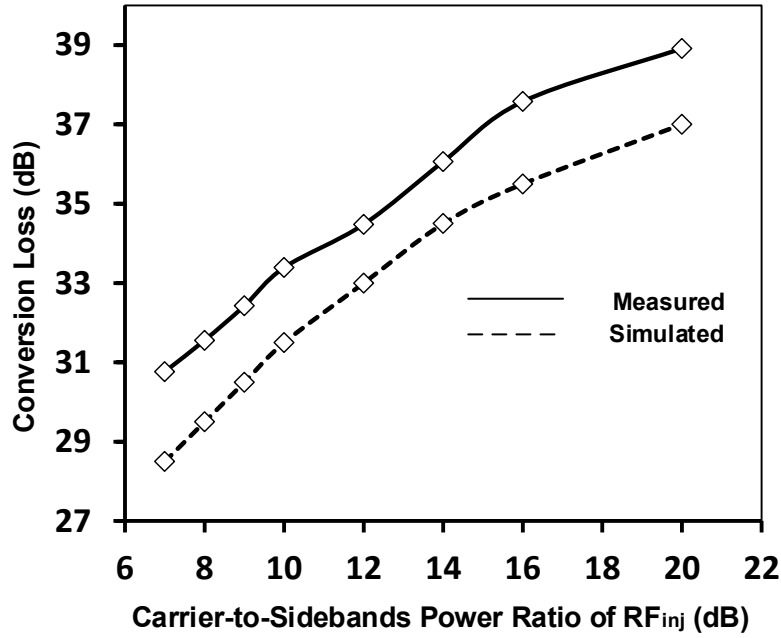


Figure 4.13: Measured and simulated conversion loss versus carrier-to-sideband power ratio of the injected RF_{inj} signal.

Fig.4.13 shows the measured conversion loss versus the ratio between carrier power and sideband power in the injected AM signal. It reveals that conversion loss can be enhanced by increasing the sideband power, i.e. by increasing the modulation index. This is consistent with the results in Fig.4.12.

Fig.4.14 shows the conversion loss when the frequency of the modulating signal increases. It can be seen that as the modulating frequency f_a increases, parasitic capacitance at the common node V_{CM} takes effect and the conversion loss slightly increases. However, these results suggest that the tag can be written or interrogated at high data-rate. Note also that the removal of the pad parasitic capacitor C_{pad} (at the zero-IF pad), which is there for measurement purposes, would significantly lower the total capacitance at V_{CM} .

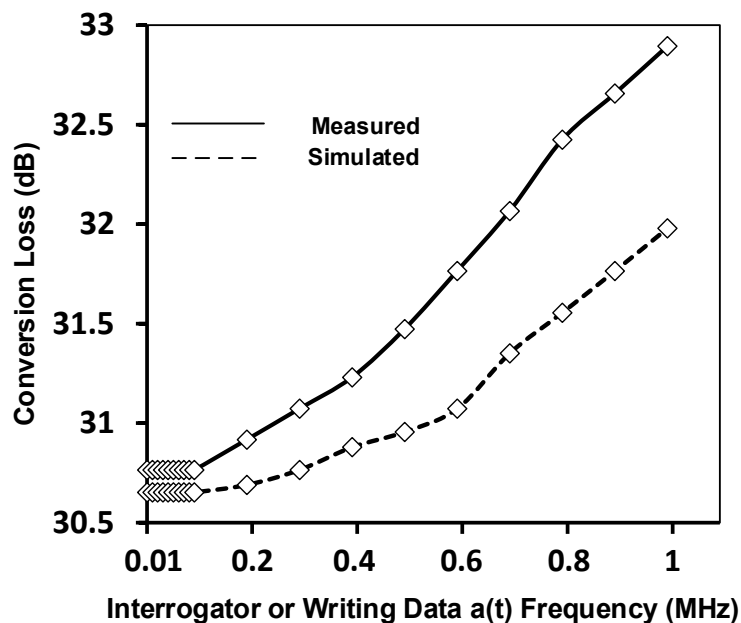


Figure 4.14: Measured and simulated conversion loss versus frequency of modulating signal $a(t)$.

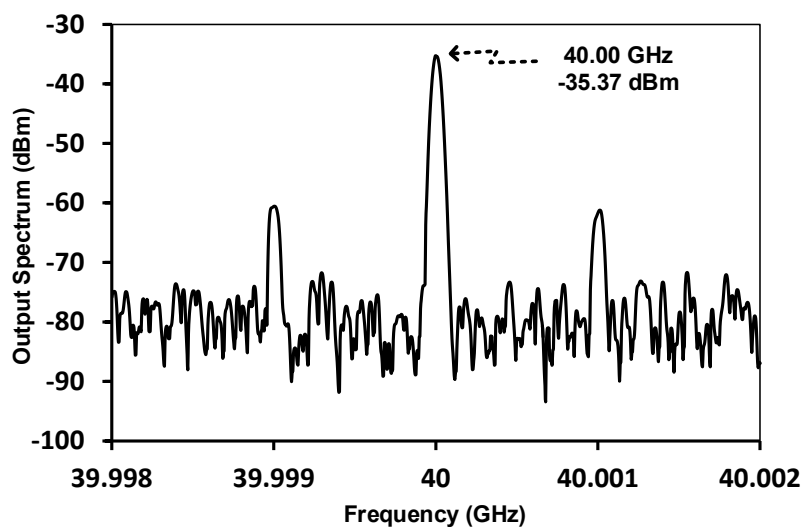


Figure 4.15: Spectrum of SOM measured at the RFout pad, when a 1-MHz sinus wave emulating the tag's data to be transmitted is injected into the SOM (Res BW 39 kHz, VBW 39 kHz).

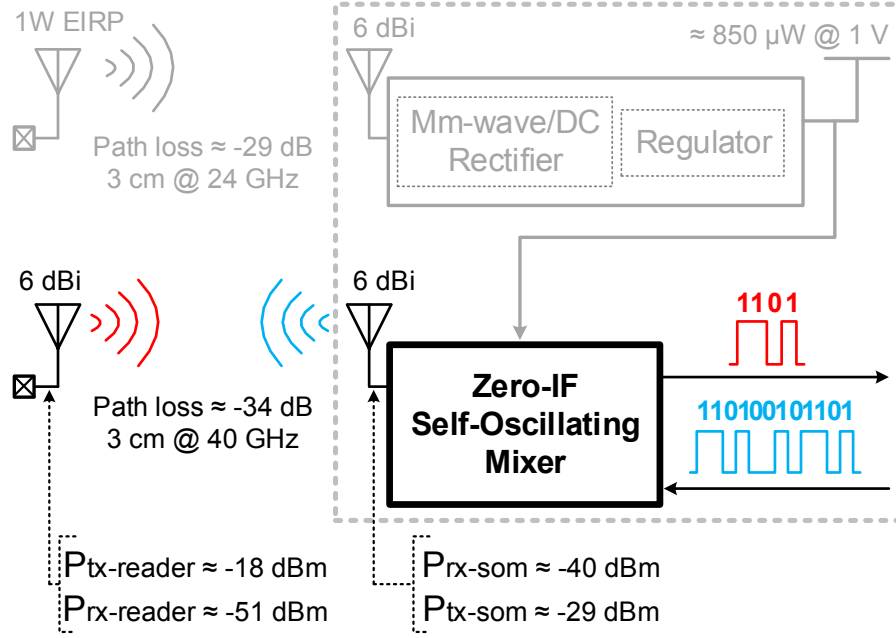


Figure 4.16: Power link-budget of the proposed MMID tag-reader system.

To evaluate SOM's tag-to-reader communication capability, a 1 MHz signal emulating the tag's data to be transmitted was injected into the SOM, while the SOM was injection-locked by a -40 dBm CW RF signal. Fig.4.15 shows the spectrum of the up-converted signal, measured at the output pad RF_{out} . The measured output power is about -36 dBm, and after de-embedding the cable losses @ 40 GHz, the actual output power is about -29 dBm. As a two-way communication system, the operating range of MMID is shorter between the reader-to-tag and the tag-to-reader communication range. However, for a wirelessly powered device (battery-free MMID tag in our case), the operating range is mostly limited by the capacity of a tag to harvest sufficient energy for its functioning (reader-to-tag communication range), rather than the reader's sensitivity (tag-to-reader communication range). Therefore, based on the previous published results on millimeter-wave/DC rectifier [41], and on-chip antennas [31], Fig.4.16 presents a possible link power-budget of the proposed MMID tag. With a 3 cm communication range and a 24 GHz powering signal [41], about 850 μ W @ 1 V is rectified, i.e. a power level which is largely above the required SOM's dc power. And, as illustrated in Fig.4.16, for the SOM to receive -40 dBm injection-locking power within 3 cm @ 40 GHz, it requires the reader to transmit almost -18 dBm. In the other direction, with -29 dBm power transmitted by the tag, the reader receives almost -51 dBm. Note that, a 1 W EIRP only of transmitted power [41], as considered in Fig. 4.16, to power up the tag is a

conservative analysis case. Hence, increasing the reader's transmitted power or the antenna gain will automatically increase the communication range. Therefore, the link power-budget in Fig.4.16 confirms the feasibility of the battery-free on-chip MMID tag proposed in this work (Fig.4.1).

Table 4.1 summarizes and compares performances of the previous published self-oscillating mixers with the zero-IF self-oscillating mixer proposed in this paper.

Table 4.1: Performance summary and comparison of SOMs.

	This Work	[43]	[44]	[45]	[46]
Technology	65 nm	0.13 μm	0.13 μm	0.13 μm	0.13 μm
RF Frequency (GHz)	40	30	1.57	7.8 - 8.8	5 – 11.8
Frequency Conversion	Baseband	IF band	IF band	IF band	IF band
Conversion Gain (dB)	-30	-30	36	11.6	12
Chip size (mm^2)	0.24	N/A	1.5	0.47	0.53
DC Power (mW)	0.28 (core)	26.4	5.4	12	68
	0.58 (core + buffer)				

4.5 Conclusion

A low-power zero-IF self-oscillating mixer suitable for self-powered MMID tag is proposed and analyzed. In addition to the SOM injection-locked to the reader's carrier frequency, operating the SOM's cross-coupled pair transistors in a region where their transconductances are the most sensitive to the externally injected signal and providing proper isolation between the millimeter-wave and the down-converted baseband signal, are the key factors to enable a low-power zero-IF self-oscillating mixer. Besides, the analysis detailed in this work reveals that the conversion loss significantly depends on how much the injected carrier signal is modulated (the modulation index value) and the SOM power consumption. A 40 GHz zero-IF SOM was fabricated in a standard 65-nm CMOS process, and a measured conversion loss of about 30 dB under -38 dBm injected RF power, with a power consumption of only 280 μ W and 580 μ W during the reader-to-tag and the tag-to-reader communication, respectively, supports the feasibility of the MMID tag-reader system proposed in this work. These results contribute to the demonstration of a potential for high data-rate μ RFID fully integrated on a single CMOS die with no external components.

**CHAPTER 5 ARTICLE 3: HIGH-DATA-RATE SINGLE-CHIP
BATTERY-FREE ACTIVE MILLIMETER-WAVE IDENTIFICATION
TAG IN 65-NM CMOS TECHNOLOGY**

Pascal Burasa, Tarek Djerafi, Nicolas G. Constantin, and Ke Wu

Published in the *IEEE Transactions on Microwave Theory and Techniques*, vol.64, no. 7, pp.
2294-2303, Jul. 2016

In this paper, a class of high data-rate, battery-free, yet active miniature RFID tag without any external components (except antenna) operating at millimeter-wave frequencies is proposed and demonstrated. This fully embedded tag consists of a recently proposed CMOS-based zero-IF self-oscillating mixer, a high power conversion efficiency millimeter-wave-to-dc rectifier and an ultra-low power voltage regulator on a single chip, integrated with ceramic-based antennas. Interconnection between the CMOS die and the antenna is realized using a wire-bonding technique, which is compensated and optimized to match the antenna input impedance and also to minimize the wire-bond associated losses at millimeter-wave frequencies. The 10 x 10mm² tag wirelessly harvests its energy from an incoming signal at 24-GHz, receives and recovers the data sent by reader on an AM-modulated 40-GHz carrier, and transmits its data back to the reader on a 40-GHz carrier, using an AM modulation as well. The tag exhibits a bit-rate of about 500 kbps during the reader-to-tag communication and 10 Mbps during the tag-to-reader communication, solely relying on the rectified energy for powering its operation. To the best of our knowledge, such an MMID tag at millimeter-wave frequencies has never been reported in the literature.

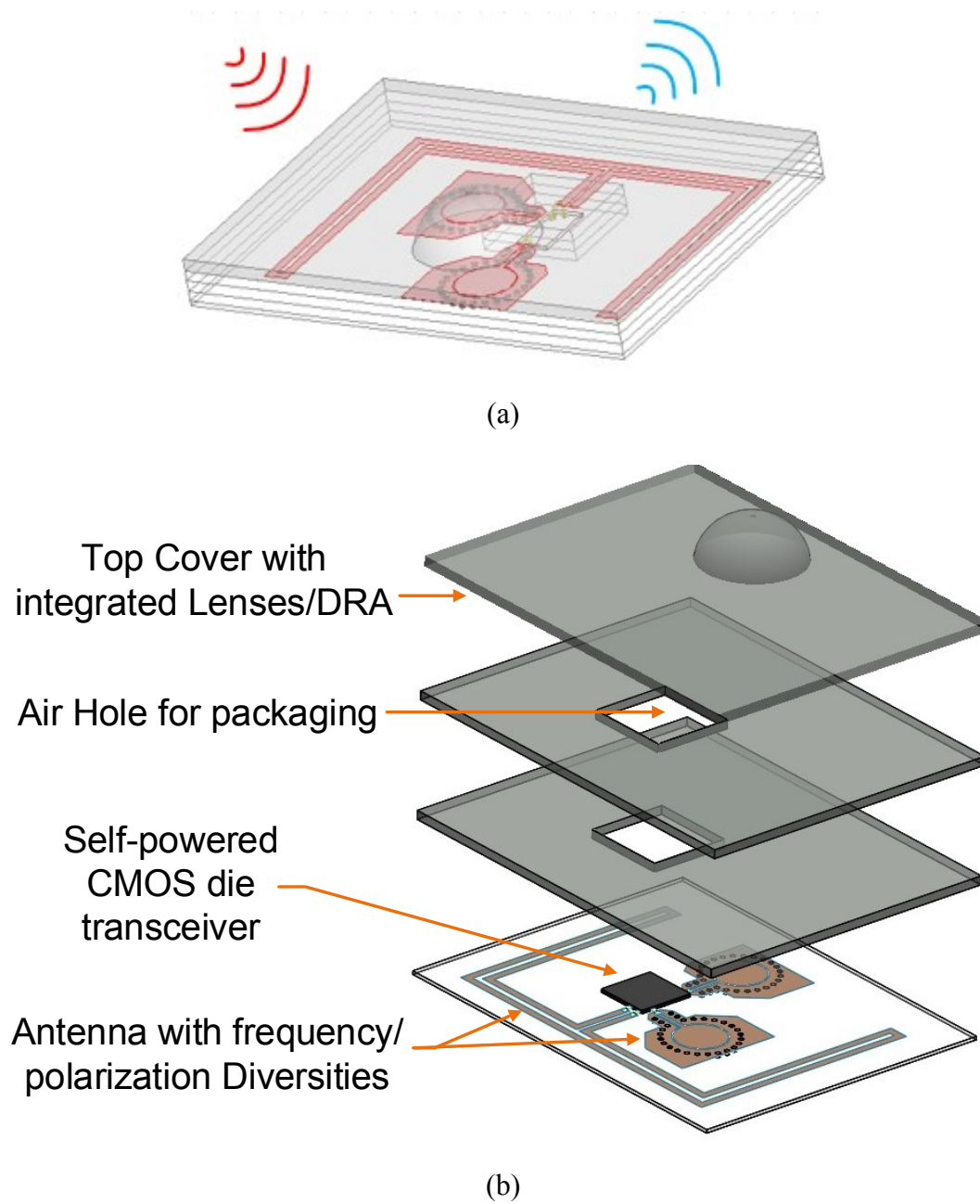


Figure 5.1: Illustration of the proposed battery-free active MMID tag in a single-chip with antenna-in-package: (a) top view, (b) exploded view.

5.1 Introduction

Radio frequency identification (RFID), a technology that is having an increasing impact on our daily life, has been mostly designed and developed at low RF frequencies (below 3-GHz). For many applications where short-range (few centimeters) and low data-rate communications are sufficient and in some cases even preferable, inductively coupled RFID systems that operate over either low-frequency (LF) or high-frequency (HF) bands have performed quite well and have been widely used for practical and commercial applications such as security, access control, etc [37]-[40]. On the other hand, in the quest for a longer communication range (few meters), higher data-rate, and smaller antenna size, radiative (or far-field coupling or rectification-based) RFID systems operating over ultra-high frequency (UHF) and microwave frequency bands (e.g., 2.4-GHz) have recently attracted much attention in the research and development community. This has been driven by a strong desire to cover numerous highly anticipated applications in connection with the internet of things (IoT), which will require a countless number of sensors and RFID devices. Typically, over these RF bands, a restricted available bandwidth together with an undesired tag size (mainly dominated by its antenna size) are the main factors that have been impeding the evolution of active RFID technology. As for purely passive RFID tags, they are hurdled by a limited number of bits and also a rather short interacting distance. Overcoming these limitations requires alternative approaches and systems, innovative techniques and integrated circuits, which allow propelling the RFID technology for operation at millimeter-wave frequencies. Indeed, the still-emerging millimeter-wave identification (or MMID) technology takes advantage of a much smaller antenna size at these frequencies and also a significantly larger bandwidth (a few GHz, for example) available at millimeter-wave carrier frequencies, which are being considered in the research community for this type of applications (e.g., 35 GHz, 60 GHz). Over these frequency bands, an effective wavelength is in the order of a few millimeters, hence close to a typical semiconductor (CMOS) die size. Therefore, it becomes possible to integrate the entire MMID tag circuitry on a single chip. The antenna may either be integrated on the same chip (in the 60 GHz band, in particular), or embedded in the related package (antenna-in-package – AiP), as illustrated in Fig.5.1. Shown in Fig. 5.1 is our proposed battery-free MMID tag containing a millimeter-wave transceiver, including millimeter-wave, analog and high-speed digital signal processing blocks,

which are entirely supplied by on-chip energy harvesting and power management circuits. The architecture shown in Fig. 5.2 has recently been proposed in [38] and represents a new generation of high data-rate, miniaturized active RFID technology for a wide range of applications.

Some research works in MMID technology have been published in recent years [51], [19]-[24]. However, none of them has demonstrated a functional MMID system using a single-chip tag, and none of them has experimentally shown the benefits of an integrated tag system operating at millimeter-wave frequencies. In [23], for example, a standard UHF RFID chip was combined with external mixers to up-convert the transmit-UHF signal to 10 GHz and down-convert the received 10 GHz signal to the UHF, with a 40 kbit/s data rate. In [24], a 60 GHz RFID tag design was reported, but a low RF-to-dc PCE (1.2 % at 2dBm input power) translates into a bit-by-bit sequential communication, limiting the data rate to 5 kbit/s at a range of 1.3 cm.

In our previous work [52], an ultra-low power zero-IF self-oscillating mixer (SOM) that performs both millimeter-wave receiver and transmitter functions is proposed, analyzed, and demonstrated. The proposed SOM presents an adequate candidate for extremely low-power transceivers such as self-powered active MMID tags. In this paper, however, a miniaturized (10x10 mm² including antennas) high data-rate, battery-free, yet active RFID tag that operates at millimeter-wave frequencies is proposed, studied and demonstrated. As illustrated in Fig. 5.2, the proposed tag consists of a CMOS die connected to antennas through wire bonds. The CMOS die comprises a millimeter-wave-to-dc rectifier to wirelessly harvest and provide energy to the tag, an ultra-low-power voltage regulator, and a zero-IF self-oscillating mixer (SOM) that performs both millimeter-wave receiver and transmitter functions to enable communication between the reader and the tag. This integration allows the demonstration of the three different functions in real environment. A standard, low-cost, and commercially available CMOS process with a high integration capability is the process of choice for a widespread adoption of the proposed new MMID technology. For the antenna-in-package implementation, a ceramic substrate is chosen in this work since it allows the realization of a small antenna. Besides, ceramic is a popular material of choice for antenna-in-package [53], rendering the single-chip CMOS tag and antenna-in-package assembly illustrated in Fig. 5.1 a viable solution. The tag wirelessly harvests its energy from the incoming signal at 24-GHz, receives the data sent by the reader on an AM modulated, 40-GHz carrier, and transmits its data back to the reader on an AM modulated, 40-GHz carrier as well. All the communications between the reader and the tag happen at a high bit-rate. To the best of our

knowledge, such an integrated MMID tag chip operating at millimeter-wave frequencies has never been reported in the literature.

Section II describes at a conceptual level the operating principles of the proposed MMID system. Section III analyzes the design of a self-powered, self-oscillating mixer. A small footprint, 24-GHz differential and 40-GHz dual-polarized antenna design is discussed in section IV. Section V presents and discusses the measurement setup and experimental results.

5.2 Proposed MMID system with battery-free active tag on single-chip

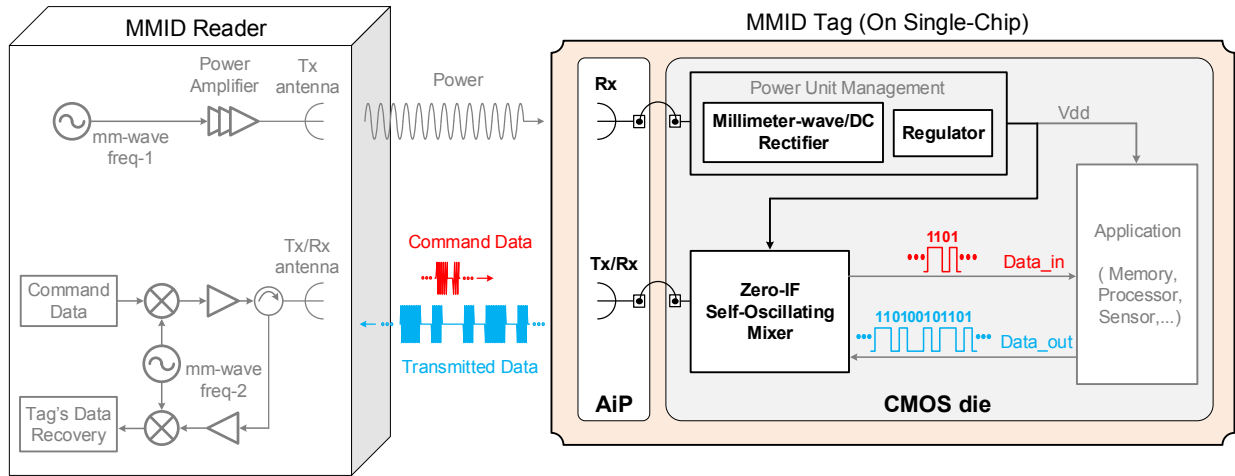


Figure 5.2: Block diagram of the proposed millimeter-wave identification (MMID) system with a battery-free active tag on single-chip.

As illustrated in Fig. 5.2, a reader simultaneously shines a tag or multiple tags with two tones ($Freq_1$ and $Freq_2$) at millimeter-wave frequencies. A continuous wave tone at frequency $Freq_1$ is dedicated to supplying energy to the tag, and its available power is applied to the millimeter-wave-to-dc rectifier through a differential antenna connected to the rectifier via wire-bonds. It is worth noting that a differential antenna is used because the rectifier is based on a differential-driven cross-coupled topology that has demonstrated a high power conversion

efficiency at millimeter-wave frequencies [41]. An ultra-low power voltage regulator is used to ensure a more stable power supply and reduce the ripples on the rectified voltage. The reader and the tag exchange data at a high bit-rate on a different carrier at frequency $freq_2$, therefore without compromising the tag's energy, regardless of the type of modulation or coding used for communication. The tag makes use of a dual-polarized antenna with a high isolation to desensitize both receiving and transmitting antennas. As depicted in Fig. 5.2, during the reader-to-tag communications, the reader sends an AM-modulated signal to the tag. This modulated signal is down-converted directly to baseband thanks to a self-oscillating mixer (SOM), and the recovered data is then sent to the processing block. In the opposite path, during the tag-to-reader communications, the tag's data are up-converted through the same SOM and transmitted to the reader on a carrier at frequency $freq_2$.

The antennas are connected to the CMOS die via wire-bonds, as illustrated in Fig. 5.1. Although the wire-bonding increases the impedance and losses, especially at higher frequencies, it has been proven that interconnection using wire-bonding is still applicable and appreciable at low cost in the 60-GHz band and beyond [54].

5.3 Self-powered zero-IF self-oscillating mixer circuit

Fig. 5.3 shows the power management circuit block used in this work. It consists of a millimeter-wave-to-dc rectifier and an ultra-low power voltage regulator. The incoming RF signal from the reader, dedicated to supplying energy to the tag, is received and rectified by the millimeter-wave-to-dc rectifier circuit. The rectifier is a differentially driven cross-coupled topology comprising M1 to M4, Ca, Cb, and Cload, which was demonstrated to offer a high power conversion efficiency (20 %) at millimeter-wave frequencies [38]. During the positive cycle of the incoming millimeter-wave signal (RF in Fig. 5.3), and as the difference between V_{in_rf+} and V_{in_rf-} swings above the transistors' threshold voltage V_{th} , the pulsed currents $IM3_{pos}$ and $IM2_{pos}$ charge the capacitor Cload. In the negative cycle of RF, Cload is charged by $IM4_{neg}$ and $IM1_{neg}$. Transistors M1, M2, M3, and M4 periodically charge the capacitor Cload, as long as the reader shines the tag. A rectified dc voltage is always available across Cload.

However, unlike a battery, the rectified dc voltage V_{rect} is far from being a stable power supply. It varies with the distance between the reader and the tag, the level of the power received at the antenna, the antenna alignment, the operating state of the rest of the tag's components, etc. Besides, since the rectified voltage is intended to supply energy to the SOM (Fig. 5.4), any supply noise (variations of V_{rect}) will be injected into the SOM. On one hand (during the reader-to-tag communications) this adds noise to the down-converted zero-IF (data in Fig.5.4), and on the other hand (during the tag-to-reader communications) the noise is up-converted to the vicinity of the SOM's natural oscillation frequency and therefore contributes to the overall SOM phase noise [55], [50], and [56].

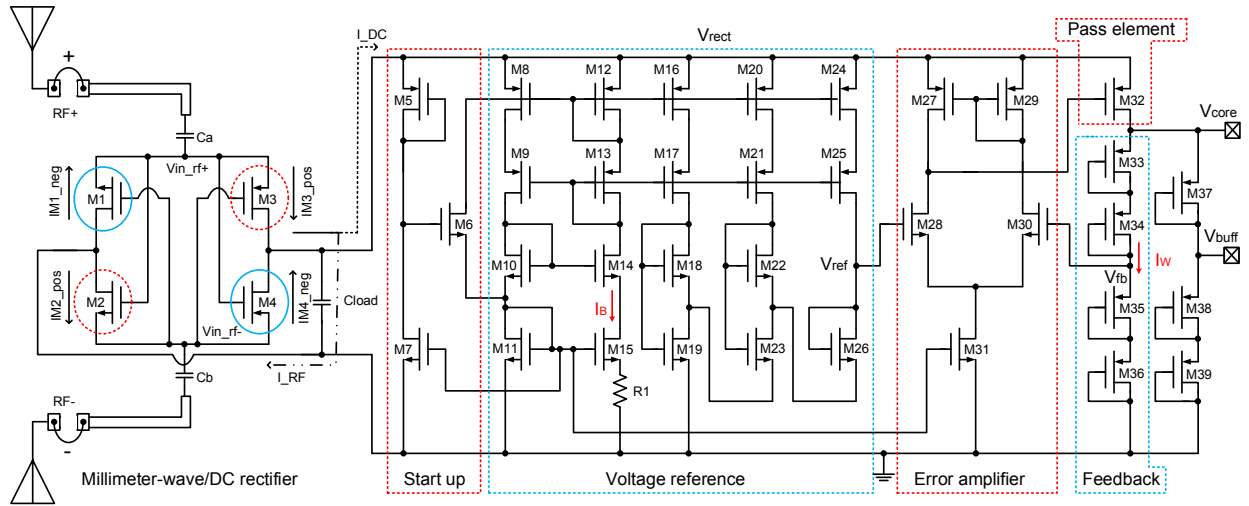


Figure 5.3: Circuit schematic of the power unit management, comprising of a mm-wave/dc rectifier and a low-power voltage regulator.

As illustrated in Fig. 5.3, an ultra-low power voltage regulator is implemented, comprising a start-up circuit, a voltage reference, an error amplifier, a feedback network, and a pass element. The regulator follows the rectifier to reduce the ripples on the rectified voltage V_{rect} and to provide a more stable power supply for the SOM and the digital block [57]. Most of the voltage regulator's transistors are optimized to operate in the subthreshold region for a low power dissipation since the whole tag's energy supply relies on the collected and rectified energy. The circuit comprising transistors M8 to M15 forms a current source that generates a stable bias current I_B with voltage

and temperature compensation. Transistors M16 to M26 form a bias voltage V_{ref} that is derived from the stabilized current I_B , and provide a stable reference voltage V_{ref} for the non-inverting input (gate of M28) of the error amplifier. The amplifier, consisting of M27 to M31, senses and compares the feedback voltage V_{fb} with the reference voltage V_{ref} . Whenever V_{fb} differs from V_{ref} , the amplifier generates a proportional controlling signal to the pass element M32, thereby setting the output voltage V_{core} to the desired voltage, ideally independent of the loading condition and the rectified voltage variation. The feedback network that determines the output voltage V_{core} consists of four diode-connected PMOS transistors M33 to M36, allowing to benefit from larger equivalent resistors with smaller chip area. Therefore, this significantly reduces the wasted current I_W that flows into the feedback network even if there is no load connected to the regulator. For such a self-powered active MMID tag, power consumption is the main issue and any leaking power should be minimized. Transistors M5, M6, and M7 form an auto-startup circuit that forces the voltage regulator circuit to start working in the right state.

Line regulation LiR and load regulation LoR , respectively, can be expressed as [57]:

$$LiR = \frac{\partial V_{core}}{\partial V_{rect}} \approx \frac{1}{g_{m28}(r_{o-M28} \parallel r_{o-M27})} \left(\frac{R_{M33,34} + R_{M35,36}}{R_{M35,36}} \right) \quad (5.1)$$

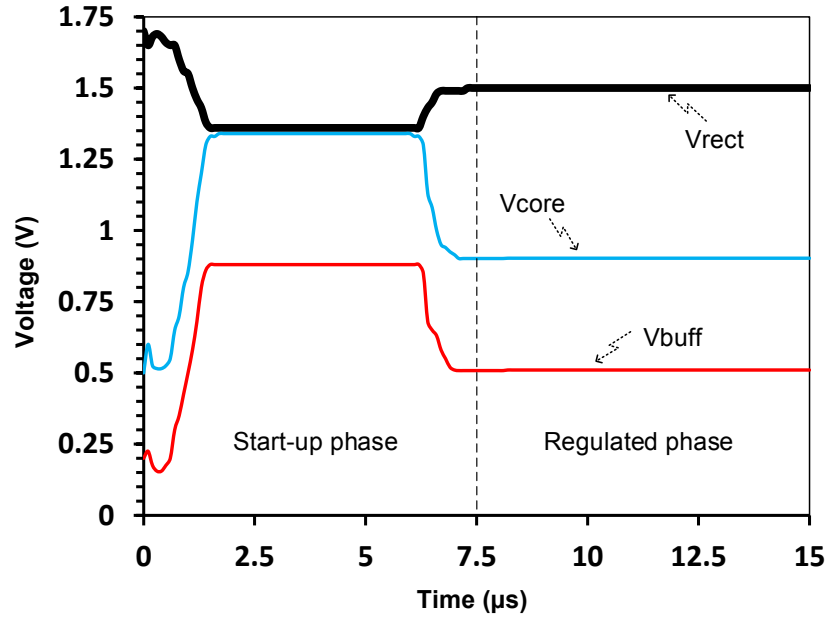
$$LoR = \frac{\partial V_{core}}{\partial I_{SOM}} \approx \left[\begin{array}{c} \left(\frac{r_{o-M32}}{g_{m28}(r_{o-M28} \parallel r_{o-M27})} \right) \\ \left(\frac{1}{g_{m32}(r_{o-M32} \parallel R_{SOM})} \right) \\ \left(\frac{R_{M35,36} + R_{M33,34}}{R_{M35,36}} \right) \end{array} \right] \quad (5.2)$$

where $g_{m28}(r_{o-M28} \parallel r_{o-M27})$ represents the voltage gain of the error amplifier, g_{m28} and g_{m32} are the transconductances of the differential error amplifier and the pass element M32, respectively, $r_{o-M27,28,32}$ represent the output resistance of M27, M28, and M32 respectively, $R_{M33,34}$ and $R_{M35,36}$ are the equivalent resistances of M33 to M36, and R_{SOM} is the SOM's loading resistance.

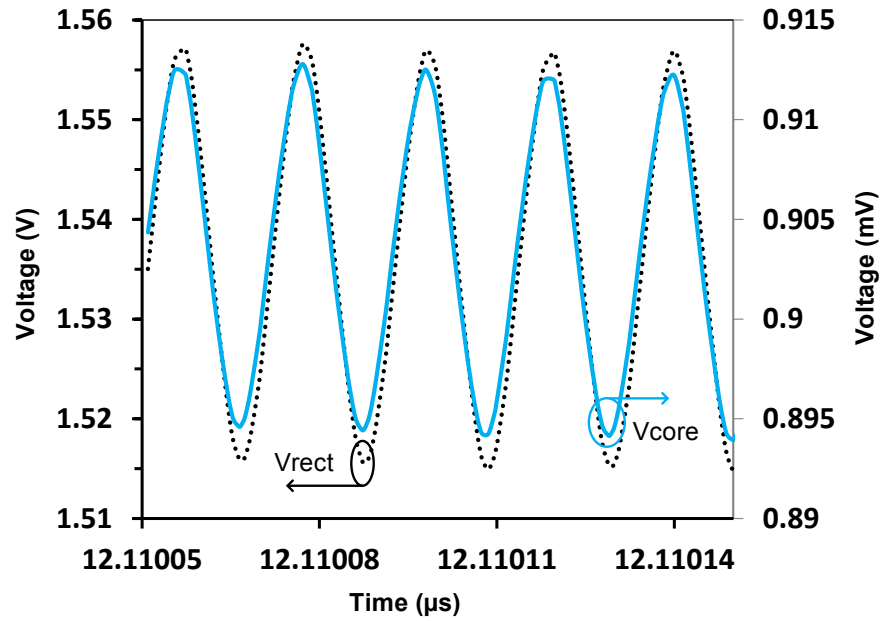
external RF source, nor any frequency conversion to an intermediate frequency (IF), which significantly reduces the power consumption. Furthermore, the injected in-phase energy on one hand relaxes the negative resistance of the SOM, thereby triggering oscillation with a lower power consumption, and on the other hand maintains phase coherence between both signals, thereby enhancing the SOM phase noise, as well as the phase noise of the down-converted baseband signal. RF_{inj} signal is injected into the SOM through M1. Both RF_{inj} and the SOM's natural oscillation frequency are self-mixed thanks to the cross-coupled pair transistors M2 and M3 [52]. The down-converted baseband signal is extracted at the common node V_{cm} , which simultaneously acts as a virtual ground at the RF frequency and as a high impedance at the baseband frequency.

During the tag-to-reader communications, a CW injection-locking signal is transmitted by the reader in order to stabilize and keep a phase coherence between the reader and the SOM, and the tag injects its data (from its memory, sensor...) into the mixer as illustrated in Fig. 5.4. The baseband information from the tag, which may have a large bandwidth, is up-converted to the vicinity of the SOM's injection-locked frequency, without compromising the SOM operation. As illustrated in Fig. 5.4, the up-converted signal is sensed at the output node V_n by an RF buffer comprising $Mb1$, $Mb2$, $Lb1$, $Lb2$, and $Cb1$. The output RF_{out} is matched to the transmitting antenna.

Fig.5.5 (a) shows the transient response of the power unit management block when it is shined with a 24 GHz source. The voltage regulator requires a start-up time of 7.5 μs , and the regulated voltages are 900 mV and 500 mV for the SOM's core section and buffer section, respectively. The voltage regulator exhibits a line and load regulation of 6 mV/V and 13 mV/100 μA at 27⁰ C, respectively, with a current consumption of 500 nA and loading current capacity of 900 μA . As shown on the Fig.5.5 (b), the supply voltage noise (variation of the rectified and the regulated voltage) are as low as 43 mV and 18 mV, respectively.



(a)



(b)

Figure 5.5: Simulated results of the power unit management circuit (powering RF signal = 24 GHz @ 10 dBm): (a) start-up and regulated phases as a function of time, (b) rectified and regulated voltage ripples.

5.4 A small footprint high-gain 24-GHz differential and 40-GHz dual-polarized antenna

The demand for small devices with wireless connectivity and multifunction capability has generated an increasing pressure on antenna engineers to improve electromagnetic performances in smaller packages [58]. These constraints are further intensified by an increasing demand for bandwidth, efficiency, and frequency coverage. Three antennas are necessary in our design to cover the desired tasks: energy harvesting at 24 GHz, data transmission at 40 GHz, and data reception at 40 GHz, even though they may be combined into a single geometry. In demonstrating the functionality of our system, no attempt was made to develop a single antenna topology for multi-frequency applications. The two antennas at 40 GHz are arranged in a perpendicular configuration to achieve an acceptable isolation and to ensure the half-duplex communications in the both ways. Printed antennas on a ceramic substrate present the required low profile in this work, and can be assembled with MMICs attached on them.

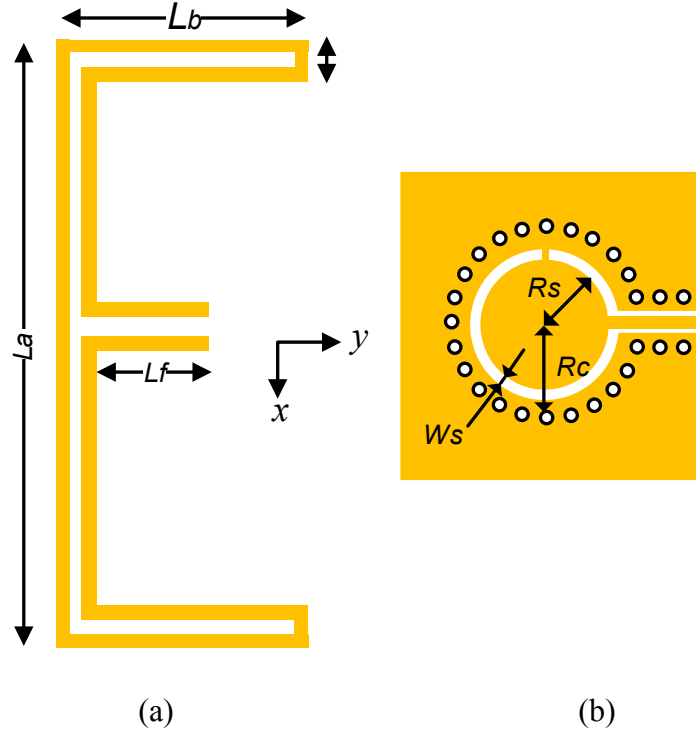


Figure 5.6: Proposed antenna: (a) U-folded coplanar folded dipole, (b) ring slot backed SIW cavity fed by GCPW.

The antennas are built on a commercially available and high-permittivity (9.6) Al₂O₃ ceramic. The structures require only a single substrate and are compatible with uniplanar technology, which facilitates connectivity with the CMOS die through a wire-bonding process. A folded U-shaped dipole is proposed for 24 GHz antenna (Fig. 5.6 (a)) and a new slot ring structure integrated in an SIW (Substrate Integrated Waveguide) cavity is proposed for the 40 GHz antenna (Fig. 5.6 (b)). The selection of the antenna is defined principally by the feed available at chip level: differential mode for the power harvesting and common-mode for the transmission access.

The folded dipole (and its complementary version: the folded slot), whose overall length is in the range of multiple wavelengths, is well known. A U-shaped antenna based on the same principle is used in our design to save space. To achieve the required resonance, the overall length is equal to about one wavelength. The input impedance can be controlled by the ratio L_a/L (Fig. 5.6). L_f is a quarter-wavelength transformer used to match the antenna impedance to that seen at the die access point [59]. The overall length is increased to reach the required gain of 7 dBi.

Annular-ring microstrip and slot antennas are possible candidates for planar millimeter-wave applications thanks to their compact geometry and potential for polarization diversity [59]. Slot-ring structures have been developed to operate as millimeter-wave frequency antennas, which are fed by coplanar waveguide (CPW) to be compatible with uniplanar mixers and low-noise amplifiers. However, these structures are not well suited for millimeter-wave applications. This is because, in order to avoid power loss into substrate modes, very thin substrates ($\lambda_d/20$) are required, which renders the substrate fragile and difficult to fabricate [60]. To eliminate substrate modes, a dielectric lens with roughly the same dielectric constant as the antenna wafer is placed on top of the antenna. The lens effectively exhibits a dielectric half-space, hence does not support surface waves. This fabrication method of the lens and the availability of the adequate material limit the use of this technique. The concept of an antenna backed by an SIW cavity may be used to avoid the substrate mode over the millimeter-wave range [61].

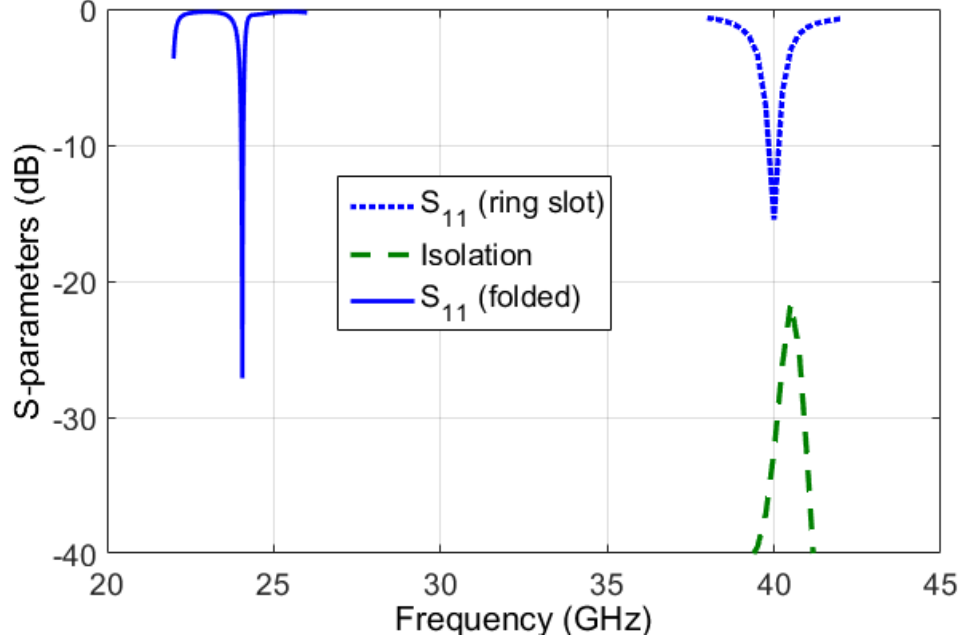
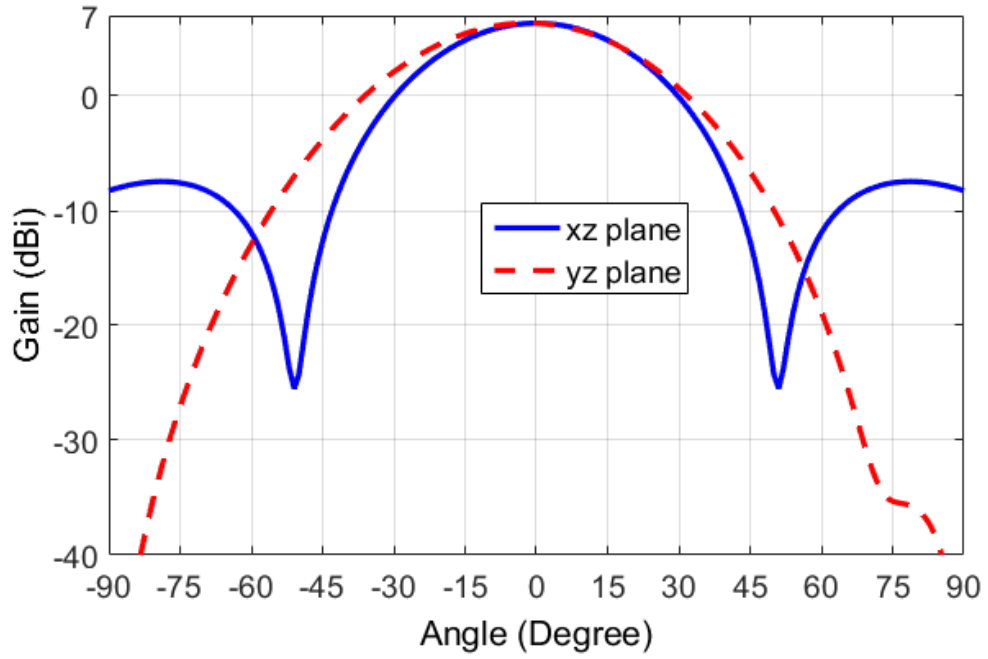


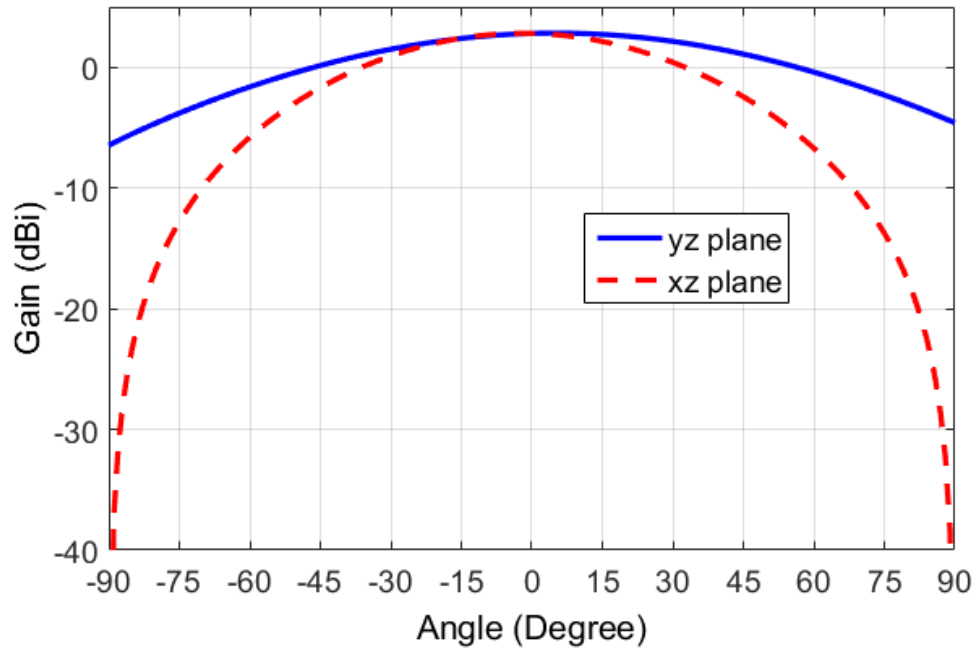
Figure 5.7: Reflection coefficient $|S_{11}|$ (dB) of the U-folded antenna and ring slot antenna and the isolation between two ring antennas in a perpendicular configuration. $L_a = 9.5$ mm, $L_b = 6.84$ mm, $L_f = 1.16$ mm, $R_s = 0.58$ mm, $R_c = 1.065$ mm, $W_s = 0.025$ mm.

The circular cavity is used to increase the quality factor and efficiency. Slot-ring antennas were designed with GCPW feed lines. The rules defined in [59] were used to design the slot ring. To validate the design, the S-parameters (Fig.5.7) of the proposed antenna were simulated using Ansoft High Frequency Structure Simulator (HFSS). The bandwidths for a 10-dB reflection coefficient are 70 MHz (0.3%) and 300 MHz (0.7%) for the 24 and 40 GHz antennas, respectively. These results show that the proposed antenna has exceptional quality factors and selectivity. This restricted bandwidth is desired to reduce interferences. The isolation between the two perpendicular antennas at 40 GHz in the required band is better than 28 dB.

The radiation patterns of the proposed antenna are shown in Fig. 5.8. For the U-folded antenna, the 3-dB beam widths are 88 and 76 degree in E-plane (xz plane) and H-plane (yz plane). For the 40 GHz antenna, in the vertical polarization case, the 3-dB beamwidths are 44 and 36 degrees in E-plane (yz plane) and H-plane (xz plane), respectively.



(a)



(b)

Figure 5.8: Simulated radiation patterns: (a) U-folded dipole antenna, (b) ring slot backed SIW cavity.

5.5 Measurement setup and experimental results

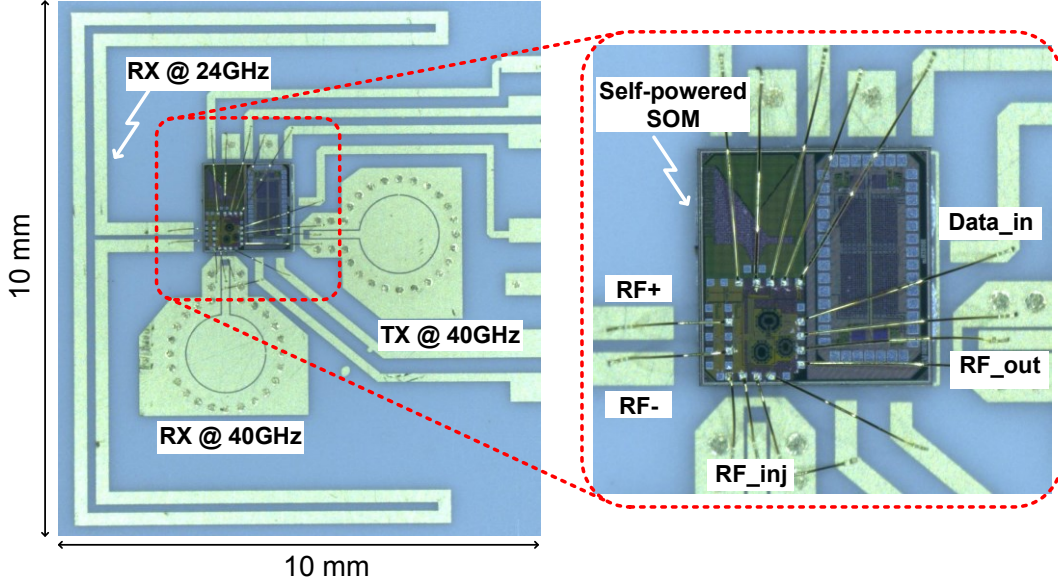
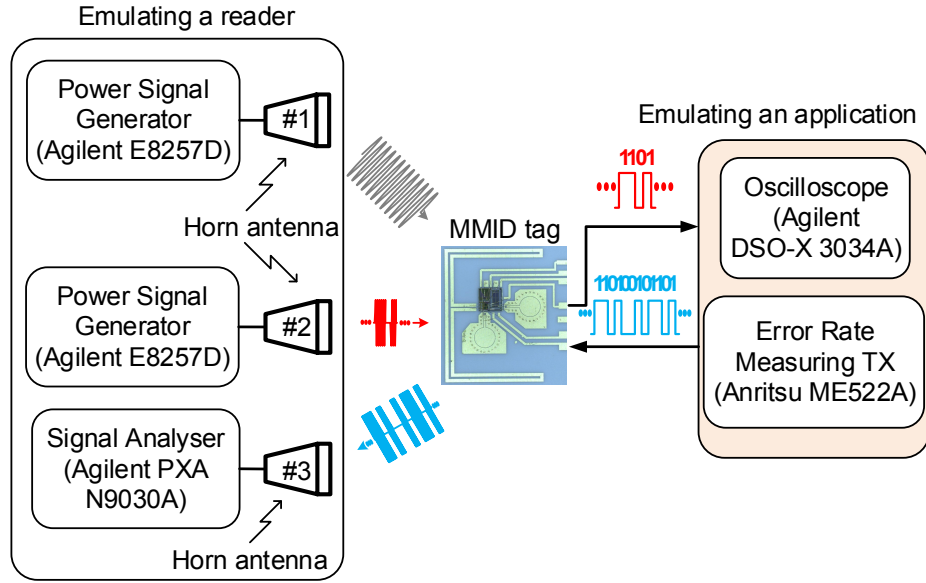


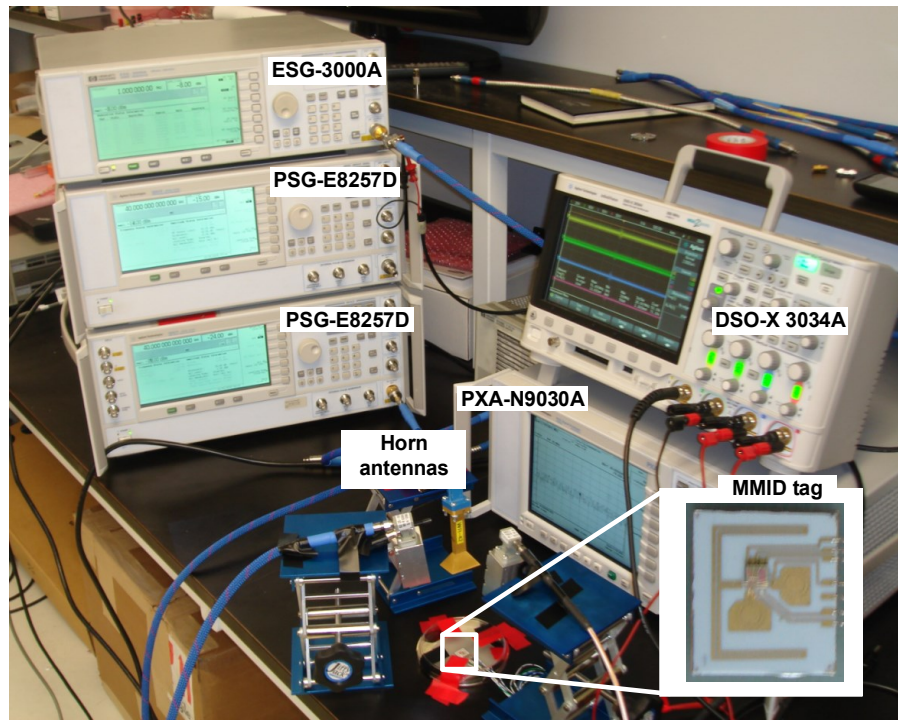
Figure 5.9: The proposed MMID tag with the CMOS die microphotograph.

Fig. 5.9 shows the proposed battery-free active MMID tag with an area of $10 \times 10 \text{ mm}^2$ including antennas. The self-powered self-oscillating mixer was fabricated using a standard 65-nm CMOS process and has an area of $0.7 \times 0.7 \text{ mm}^2$ including the bond pads. As shown in Fig. 5.9, the antennas were connected to the CMOS die using a wire-bonding technique that was realized in our Poly-Grames Research Center.

A matching network is required between the tag's antennas and the IC's input impedances, in order to maximize power transfer and the tag communication range, taking in account the bond wire effect. Since the tag access work at different single tone at mm-wave frequency range, sample matching network can be used. The chip impedance is measured using on-wafer probing to characterize the access ($Z_{in_rectifier} = 29.25 - j59.6$; $Z_{RFinj} = 7.15 - j21$; $Z_{RFout} = 14.4 - j17.25$), thereafter impedances are modeled as equivalent circuit of a parallel RC . The bond wire length and position are estimated in such way that the imaginary part is avoided. The quarter wave lines feed the resonant antennas (pure resistance) translate the input impedance of each antenna to the desired pure resistance part.



(a)



(b)

Figure 5.10: (a) Measurement setup, (b) photograph of the measurement setup.

Fig. 5.10(a) shows (at a conceptual level) the measurement setup used in this work. Three horn antennas are used to simulate the reader. The first horn antenna is connected to a power signal

generator (Agilent E8257D) and continuously shines the tag with a CW signal at 24 GHz, to supply energy to the tag. In the receiving mode (during the reader-to-tag communications) the second horn antenna, which is connected to another power signal generator (Agilent E8257D) to emulate the reader's transmitter, sends data to the tag over a 40 GHz carrier frequency. The recovered data (the down-converted baseband signal) is read at the output of the tag with a digital oscilloscope (Agilent DSO-X3034A) having a 1 M Ω input impedance that emulates the input impedance of a digital processor. In the transmitting mode (during the tag-to-reader communications) a 40 GHz CW signal sent by the PSG (via horn antenna two) injection-locks the tag. At the same time, an error rate measurement equipment transmitter (Anritsu ME522A), which randomly (with a fixed data rate) generates a flow of data, injects the data into the SOM to emulate the tag's data to be transmitted to the reader. This baseband information is up-converted, transmitted by the tag, and detected by a third horn antenna connected to a signal analyzer (Agilent PXA N9030A) emulating the reader's receiver. Fig.5.10 (b) shows a photograph of the measurement setup.

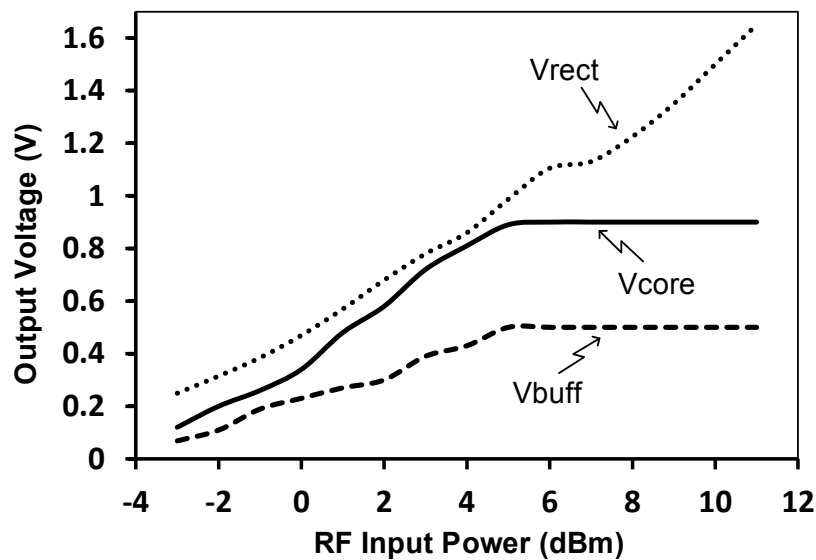
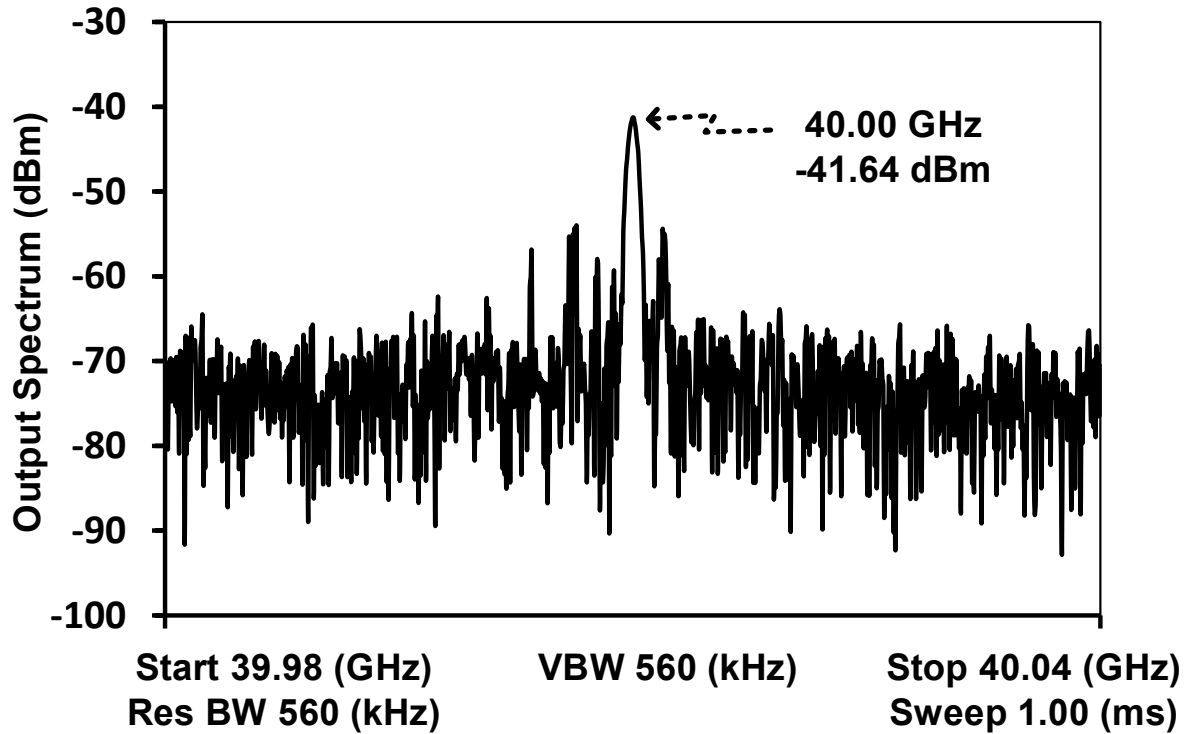


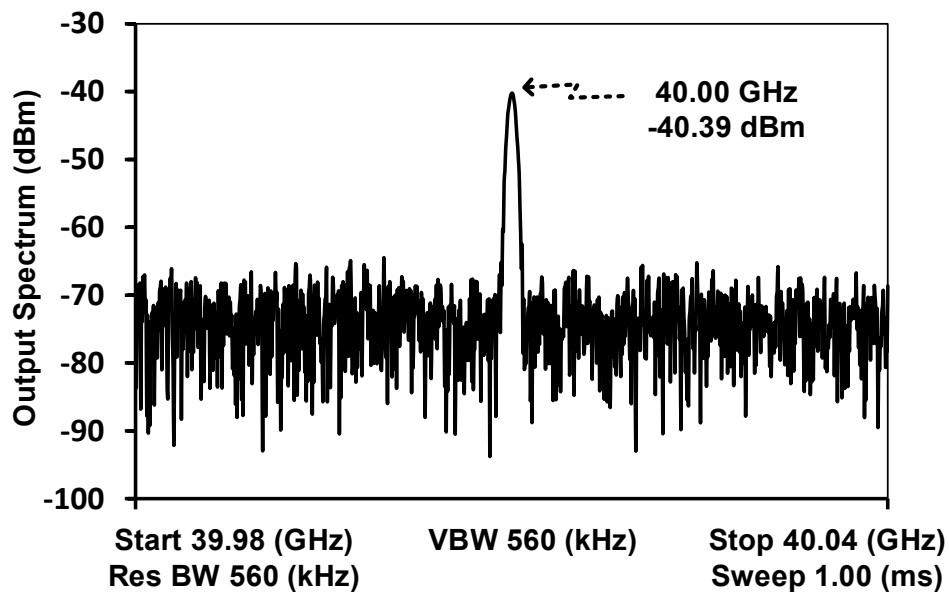
Figure 5.11: Rectified and regulated voltages as a function of RF input power (RF powering signal = 24 GHz) measured at the output of the tag.

Fig.5.11 shows the rectified and regulated voltages measured at the output of the tag, when the tag is being shined by a 24-GHz source with a variable distance between the tag and the source (variable RF input power). As shown in Fig.5.11, starting from an estimated available power of

about 6 dBm at 24 GHz across the antenna of the rectifier, when the distance between the tag and the powering horn antenna is within 3 cm, the tag rectifies sufficient dc power for its operation. Regulated dc supply voltages of 900 mV and 500 mV across the SOM's core and buffer output, respectively, were measured. The operating range is mostly determined by the capacity of a tag to rectify sufficient energy for its operation. Once this range is reached (within 3 cm in our case), the reader and the tag start exchanging their data.



(a)



(b)

Figure 5.12: Measured spectrum from the tag: (a) when the tag is unlocked (free-running), (b) when the tag is injection-locked by the reader ($R_{Finj} \approx -30$ dBm @ 40 GHz).

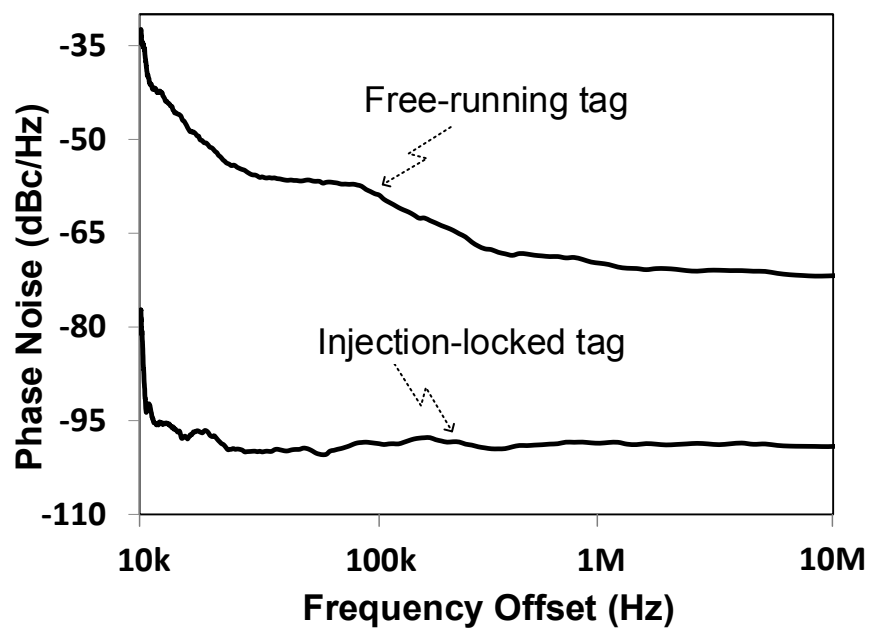
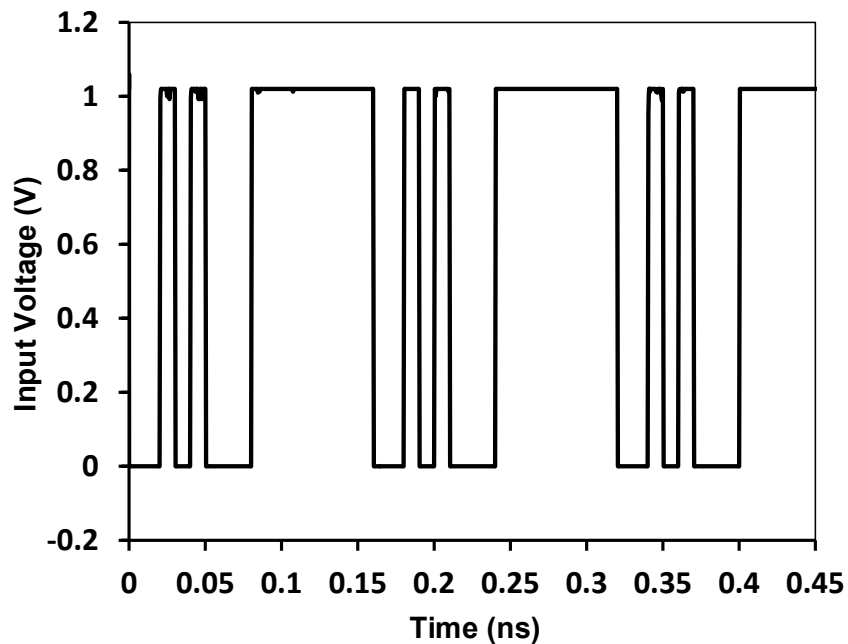


Figure 5.13: Measured phase noise from a free-running and an injection-locked ($R_{Finj} \approx -30$ dBm @ 40 GHz) tag.

Fig.5.12 (a) and Fig.5.12 (b) show the frequency spectral content of the signal received from the tag when it is in a free-running and in an injection-locked mode, respectively. As apparent and also supported by the measured phase noise as shown in Fig.5.13, the reader enhances the tag's phase noise by locking it to its carrier frequency before they (the reader and the tag) start exchanging their data.

Fig.5.14 (a) shows the flow of data which modulates a 40-GHz carrier signal (with an amplitude modulation scheme), and that is transmitted by the horn antenna two to the tag. Fig.5.14 (b) shows the down-converted data measured at the output the tag. The 40-GHz transmitted signal has been successfully received and the modulating data demodulated and recovered in the experiments. The captured eye diagram as shown in Fig.5.15, demonstrates that the tag can receive and recover data at a bit rate of about 500 kbps.



(a)

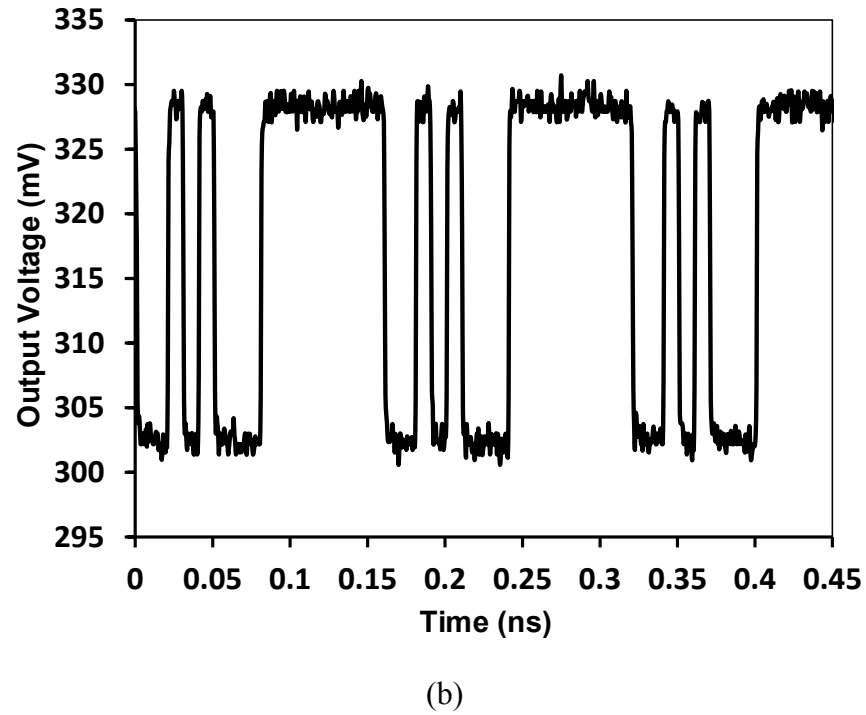


Figure 5.14: (a) Data sent to the tag by the reader @ 100 kbps, by modulating a 40 GHz carrier signal transmitted to the tag, (b) received and demodulated data measured at the output of the tag.

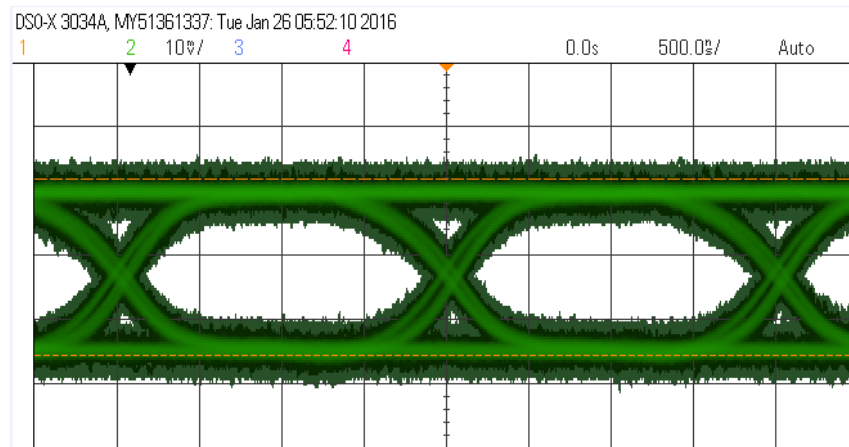
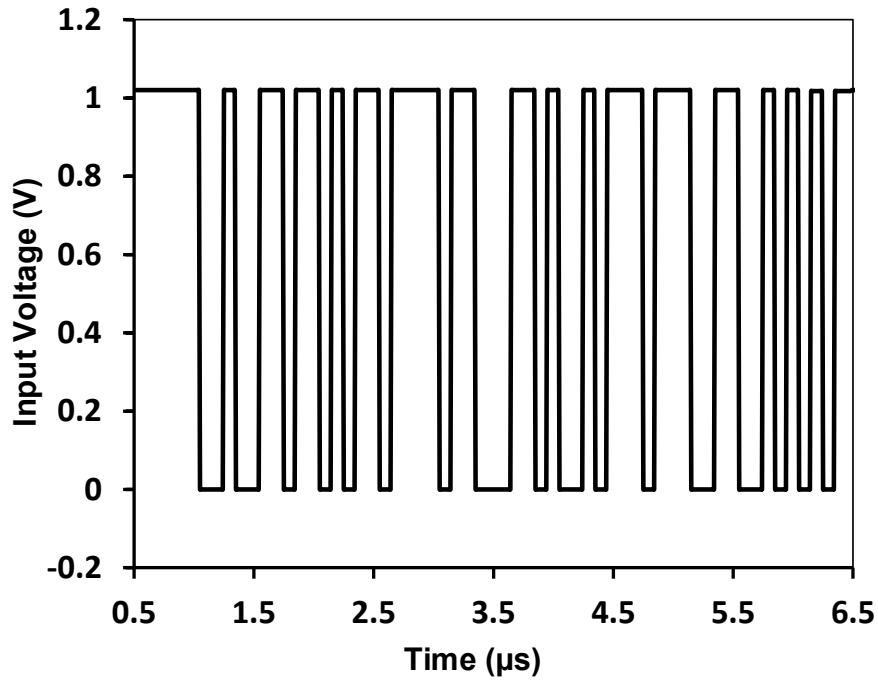
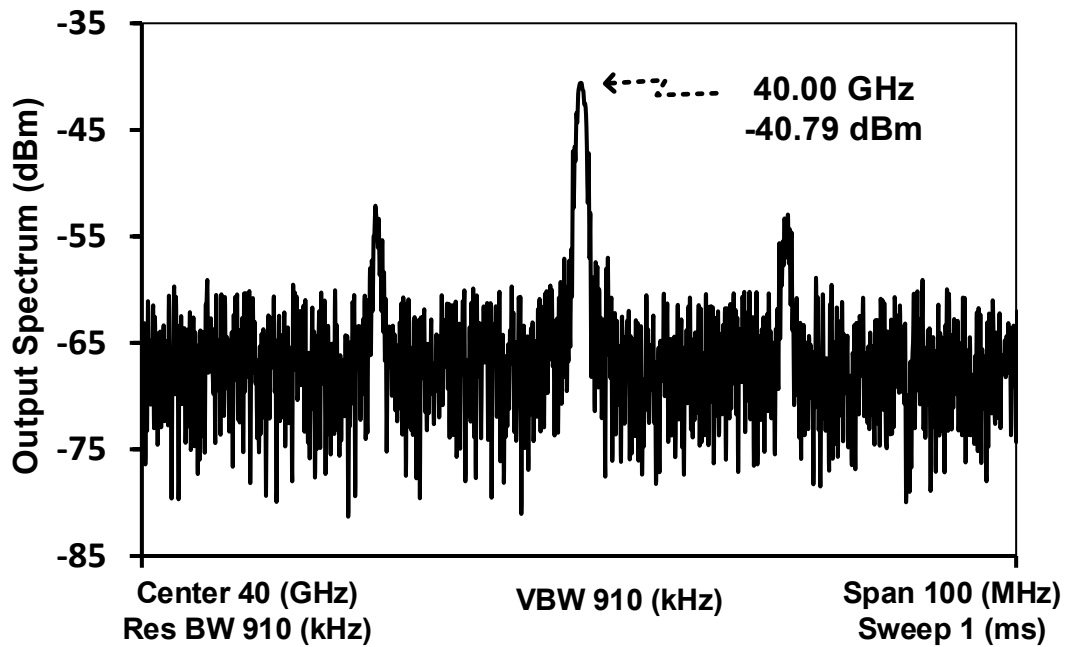


Figure 5.15: Eye diagram of the recovered data (demodulated by the tag) when the reader sends data at 500 kbps.



(a)



(b)

Figure 5.16: (a) Data sent to the reader by the tag @ 10 Mbps, by modulating the injection-locked SOM's natural oscillation frequency, (b) measured spectrum of the transmitted data from the tag.

Table 5.1: Performance summary and comparison of millimeter-wave identification (MMID) tags

	This Work	[23]	[24]	[51]
Technology	65 nm	PCB	90 nm	SIW
Tag type	Self-powered active	Passive	Self-powered active	Chipless
Sensitivity	6 dBm @ 24-GHz	-4 dBm @ 10-GHz	2 dBm @ 45-GHz	N/A
Reader-to-tag (RX) carrier frequency	40-GHz	Uses external mixer to down-convert a 10-GHz to [850-950 MHz]	60-GHz	35-GHz
Tag-to-reader (TX) carrier frequency	40-GHz	Uses external mixer to up-convert [850-950 MHz] to 10-GHz	60-GHz	35-GHz
RX data rate	500 kbps	-	-	-
TX data rate	10 Mbps	40 kbps	5 kbps	-
Tag size	10 x 10 mm ² (including antennas)	50 x 50 mm ² (including antennas)	1.3 x 0.95 mm ² (die only)	7 x 1 mm ²
Power consumption	320 μ W (RX)	-	4.8 mW	N/A
	560 μ W (TX)			

In order to evaluate the capability of the tag to transmit its data to the reader, a 10 Mbps data (Fig. 5.16 (a)) that emulates the tag's data to be transmitted to the reader was injected into the SOM while the SOM was injection-locked by a 40 GHz CW transmitted by horn antenna two. Fig.5.16 (b) shows the spectrum of the signal received by horn antenna three, and which is connected to the signal analyzer. The results confirm that the tag has successfully up-converted and transmitted its data to the reader with a detectable RF energy, without any battery in the tag, but relying only on the wirelessly transmitted and rectified energy. However, given the broad

frequency response of the amplitude-modulation mechanism in our SOM design, at the expense of a shorter communication distance between the reader and the tag, we foresee the possibility of injecting baseband signals with large bandwidths into the SOM for up-conversion and transmission from the tag to the reader, without compromising the tag's performances. This will enable a high bit-rate communication between the tag and the reader.

5.6 Conclusion

This paper has proposed and demonstrated a miniature high Gbit/s data-rate battery-free, yet active millimeter-wave identification (MMID) tag for single-chip solution. The tag consists of CMOS-based (designed and fabricated using a standard 65-nm CMOS process): zero-IF self-oscillating mixer, a high power conversion efficiency millimeter-wave-to-dc rectifier, and an ultra-low power voltage regulator, which are all implemented on a single CMOS chip and integrated with ceramic-based antennas. Antennas are connected to the CMOS die through wire-bonds that are carefully profiled to minimize loss. The tag wirelessly harvests its energy from the incoming signal at 24-GHz, receives the data sent by the reader on an AM modulated, 40-GHz carrier, and transmits its data back to the reader on an AM modulated, 40-GHz carrier as well. All the communications between the reader and the tag were demonstrated at a high bit-rate. This supports and contributes to demonstrating the feasibility of high data-rate μ RFID fully integrated on a single-chip (an all-in-one solution) with no external components.

CHAPTER 6 ARTICLE 4: ON-CHIP DUAL-BAND RECTANGULAR SLOT ANTENNA FOR SINGLE-DIE MILLIMETER-WAVE IDENTIFICATION TAG IN STANDARD CMOS TECHNOLOGY

Pascal Burasa, Tarek Djerafi, Nicolas G. Constantin, and Ke Wu

Submitted to the *IEEE Transactions on Antennas and Propagation*, Oct. 2016

On-Chip Dual-Band Rectangular Slot Antenna for Single-Die Millimeter-Wave Identification Tag in Standard CMOS Technology

Journal:	<i>Transactions on Antennas and Propagation</i>
Manuscript ID	AP1610-1402
Proposed Manuscript Type:	Paper
Date Submitted by the Author:	04-Oct-2016
Complete List of Authors:	Burasa, Pascal; Ecole Polytechnique de Montreal Djerafi, Tarek; Institut national de la recherche scientifique Centre Energie Materiaux Telecommunications Montreal Constantin, Nicolas; Ecole de technologie superieure Wu, Ke; Ecole-Polytechnique de Montreal, M-6021, Pavillon Lassonde
Key Words :	CMOS integrated circuits, Antennas, Coplanar waveguides, Dielectric loaded antennas, Dielectric resonator antennas, Loaded antennas, Slot antennas, Millimeter wave antennas, Packaging

SCHOLARONE™
Manuscripts

Only

In this paper, an on-chip dual-band rectangular slot antenna, is proposed and demonstrated for a new generation of high data-rate, battery-free, yet active millimeter-wave identification (MMID) system, which is fully integrated on a single CMOS-die. It, therefore, does not require any external components (pinless) nor packaging parts whatsoever. The single-antenna solution proposed in this work addresses the overall system compactness, the cost, and the underlying technical challenges related to multi-frequency reader-tag MMID system, such as the alignment between the reader's and tag's antennas (accurate line of sight, especially in a short-range communication system). The targeted 24/40-GHz compact antenna is a hybrid structure of a dielectric resonator antenna (DRA) and a CPW fed rectangular slot antenna in order to facilitate interconnections with other integrated circuit blocks. Design analyses of the antenna are presented. Dual dielectric resonator is optimized to enhance the antenna radiation efficiency as well as the gain over the two bands. Using a 65-nm bulk CMOS process, a chip was fabricated and tested. The prototyped antenna exhibits a measured gain of -1 dBi at 24 GHz with a bandwidth of 19 %, 0 dBi at 40 GHz with a bandwidth of 20 %, and a radiation efficiency of 41 % and 31 %, at 24 GHz and 40 GHz, respectively. The antenna occupies a compact size of $2.5 \times 2.5 \times 2.5 \text{ mm}^3$ with DRA.

6.1 Introduction

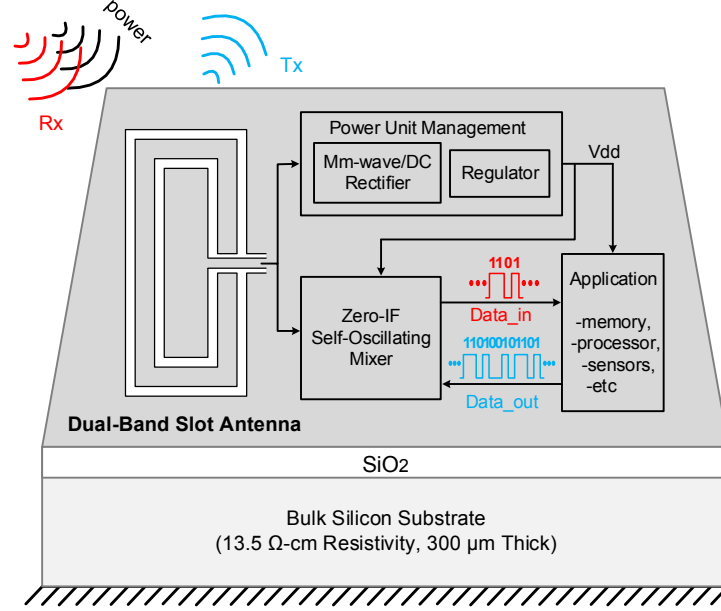
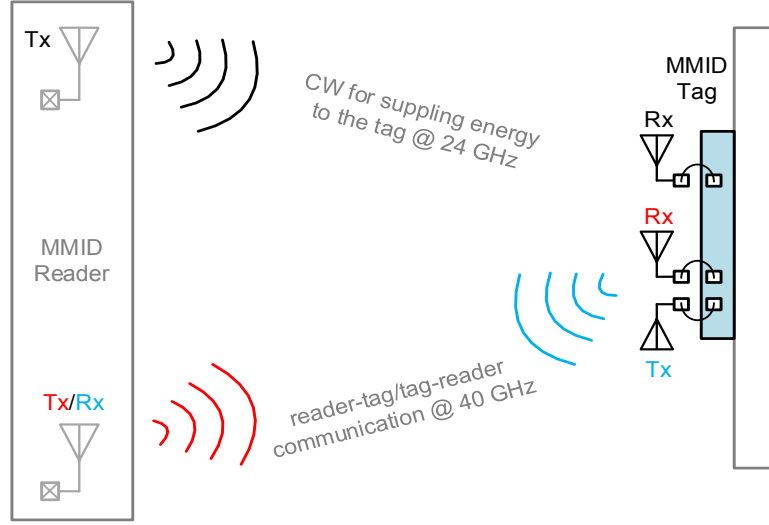


Figure 6.1: Illustration of the proposed single CMOS-die active MMID tag that uses a harvested energy from an incoming mm-wave signal from the reader.

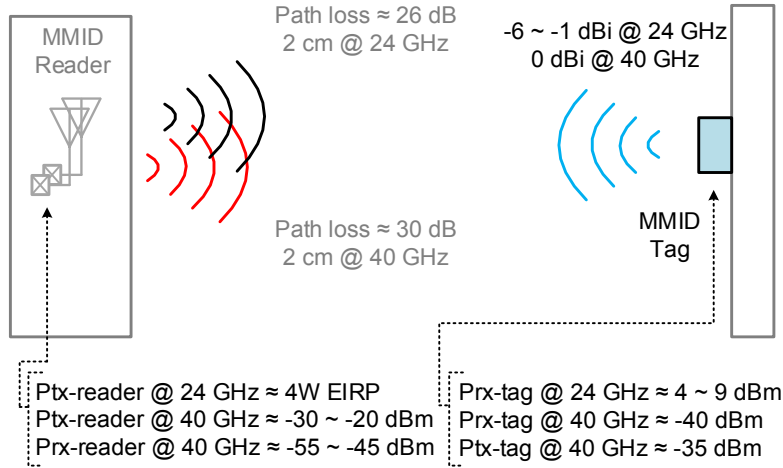
Millimeter-wave identification (MMID) technology has recently attracted much attention in both academia and industry, essentially motivated by the anticipated applications of millimeter-wave (mm-wave) technology in next generation wireless communications such as 5G and IoT technologies, and other systems which are being developed worldwide [62] and [63]. The MMID technology is emerging as a promising and future sensing technology that offers secured high-speed data communication, pinpoint sensing through steerable narrow-beam antennas, smaller tag size (over the mm-wave bands as the wavelength is comparable with IC dimensions), etc. [64].

In recent years, few works on MMID technology have been published [19]-[24], [51], and [65]. In a recently published work [65], a 10x10 mm² single-chip, battery-free, yet active MMID tag has been presented. The tag has experimentally demonstrated a bit rate of 500 kbit/s and 10 Mbit/s for downlink and uplink communication, respectively. However, three antennas were required to accomplish the desired tasks in the design: energy harvesting at 24 GHz, as well as data transmission and data reception, both at 40 GHz. Those off-chip antennas negatively impact the

tag's sensitivity because of the packaging parasitics and transmission losses associated to the chip-to-package interconnections. This is generally less severe at lower frequencies than in the mm-wave band. Therefore, integrating antennas on the same bulk silicon substrate with other MMID tag's circuit blocks, as conceptually proposed and illustrated in Fig.6.1, enables a new generation of high data-rate, fully-integrated, and pinless MMID tag without any external components nor packaging. To the best of our knowledge, such an MMID tag has not been reported yet.



(a)



(b)

Figure 6.2: Two MMID system design platforms of choice: (a) AiP-based MMID system reported in [62]; (b) AoC-based MMID system proposed in this work.

Fig. 6.2 compares the antenna-in-package (AiP)-based MMID system presented in [65], where different antennas of different polarization are embedded in the tag's package (Fig. 6.2(a)), with the proposed antenna-on-chip (AoC)-based system (Fig. 6.2(b)). It describes the fact that a single antenna in the tag as well as in the reader, with their centers aligned (Fig. 6.2(b)), translates into a wave propagation with energy more concentrated on the targeted area, hence a more efficient energy transfer. In addition to eliminating losses associated to the physical connection between the tag and the off-chip antennas, the AoC solution enables a fully integrated MMID tag design that reduces the size and cost of the tag (which are the two obstacles to the evolution and the widespread adoption of an emerging technology).

Fig.6.2 (b) presents a possible link power budget for communication within a distance of about 2 cm between a reader and the proposed single CMOS-die tag. During the reader-to-tag communication, the tag is illuminated by two tones, namely a 24 GHz powering signal and a 40 GHz signal for data exchange. Assuming a 4W EIRP from the reader (a conservative analysis case since radiated power could be much higher at 24 GHz), the RF power received at the input of the tag is at 4 ~ 9 dBm, for which the rectifier conversion efficiency presented in [38] is at its maximum. In these conditions, about 500 μ W to 1.60 mW @ 1 V is available at the output of the rectifier, i.e. a power level which is largely above the DC power required by the tag. As illustrated in Fig.6.2 (b), for the tag to receive -40 dBm injection-locking power within 2 cm @ 40 GHz [49], it requires the reader to transmit almost -30 to -20 dBm, assuming 10 to 20 dBi for the reader's transmitter/receiver antenna gain. In the other direction (tag-to-reader), with -35 dBm power transmitted by the tag [49], the reader receives almost -55 to -45 dBm, assuming the same reader antenna gain. The successful implementation of such an MMID system, therefore, would require a co-centric AoC with good radiation pattern and gain performance, e.g., ~ -6 to -1 dBi at 24 GHz and almost 0 dBi at 40 GHz.

In this work, an AoC dual-frequency rectangular slot antenna achieving the desired gain is proposed and demonstrated. The antenna is a CPW-fed (coplanar waveguide) structure, which simplifies the integration with other system blocks. The 24-GHz frequency goes to the integrated mm-wave/DC rectifier and supplies energy to the tag, whereas the 40-GHz frequency ensures a high bit-rate data exchange between the tag and the reader. The antenna is loaded with a dielectric resonator (DR) to enhance the gain and therefore the overall system efficiency.

The antenna has successfully been implemented using a commercial standard 65-nm CMOS process, and experimental results exhibit almost -1 dBi @ 24 GHz and 0 dBi @ 40 GHz, therefore supporting the feasibility of the single-die MMID tag as proposed in this paper.

6.2 Antenna Design Considerations

Different dual-frequency CMOS based systems have widely been presented in the literature as in [66] and [67]. However, most of the existing works in the literature are not related to the associated multi-frequency AoC.

Only a few dual frequency CMOS antenna techniques are presented in the technical publications. A dual-band on-chip rectifying antenna at 35 and 94 GHz for wireless power transmission was proposed in [31]. LTSA (Linear Tapered Slot Antenna) rectenna is designed in slotline (SL) and finite-width ground coplanar waveguide (FGCPW) transmission lines using a 0.13 μm CMOS process. The presented antenna achieves a fractional bandwidth of 82% and 41%, and a gain of 7.4 and 6.5 dBi at 35 and 94 GHz, respectively, with a total length of $2.9 \times 1 \text{ mm}^2$ ($0.34 \times 0.12 \lambda_0^2$, considering the lower frequency point). In fact, the used LTSA is not a dual-band antenna. Instead, it is a broadband antenna, just like the whole system comprising the FGCPW and SL transition. The presented rectenna was optimized for dual-band operation, using a bandpass filter added between the whole system and the rectifier.

In [68], a dual-band mm-wave CPW-fed AoC was presented for a 24 GHz ISM band application and for 60 GHz WPAN application. This antenna was also fabricated with a 0.13 μm standard CMOS process. The bandwidth is about 0.75% for the lower band and about 1.67% for the second band. For the lower band, the gain is about -9dBi and at the higher band, the maximum gain is about 1 dBi. The whole size is about $1.045 \times 0.76 \text{ mm}^2$ ($0.09 \times 0.06 \lambda_0^2$ considering the lower frequency).

The selection of the antenna is defined principally by the feed available at chip level proposed in [41], [52], and [65]. The rectifier circuit proposed in [41] was differentially driven, whereas the transceiver proposed in [52] uses common mode ports. To achieve dual-band characteristics in the feed with CPW, there are many reported antenna techniques and

configurations. In [69], two orthogonal C-shaped monopoles are directly fed by CPW, providing a dual band 2.4/5.2GHz with spatial diversity. In [70], two operating modes of the proposed antenna are associated with various lengths of two monopoles. The proposed antenna in [71] was constructed by dual concentric annular-ring slots fabricated on FR4 substrate, using a single CPW-fed or microstrip-fed configuration. In [72], CPW can act as both a transmission line and a radiator at the same time. An extra independent frequency can be obtained without adding new components or increasing the design complexity. Two bands are necessary in our design to cover the desired tasks: energy harvesting at 24 GHz, data transmission and data reception both at 40 GHz.

The proposed antenna consists of two concentric rectangular-ring slots and the two operating frequencies are obtained by means of those multiple radiating rectangular-ring slots. The antenna is compact due to the use of the concentric ring slots, and the outer ring resonating at 24 GHz defines the overall size. To achieve the optimal efficiency at the level of the rectifier, a DR is added to the concentric dual-band rectangular slot antenna to realize the desired gain enhancement for the MMID chip. The design parameters, rules and constraints will be detailed in the following section.

6.2.1 Slot Antenna

Although many antenna elements suitable for a CPW-fed configuration have been proposed, the slot antenna is one of the most attractive solutions. One of the main issues with CPW-fed slot antennas is to provide an easy impedance matching to the CPW line. For that reason, many slot antennas using different techniques were presented in the last decade (e.g. [73]-[75]).

Different slot antennas using CMOS technology have been reported. A novel design for a fully on-chip antenna operating at 140 GHz was proposed in [77]. In addition to a traditional microstrip feeding, the slot antenna is backed with an extremely thin cavity formed by two CMOS inner metal layers and vias in between. The simulated gain is around 2 dBi. The total area of this antenna is 1.2x0.6 mm ($0.09 \times 0.06 \lambda_0^2$ at 140 GHz). In [78], a 60 GHz slot AoC was designed on a CMOS substrate. To enhance the slot AoC performance, an off-chip artificial dielectric layer (ADL) which is known for its anisotropic properties was designed using UL2000 substrate. Gain

and efficiency at 60 GHz are 3.6 dBi and 32.5%, respectively. A folded dipole slot antenna backed by artificial magnetic conductor (AMC) structure based on a standard 0.18 μm CMOS process was proposed in [79] at 140GHz. An AMC constructed by a periodic 6x6 square patch array is adopted as the background to improve the gain of the proposed folded dipole slot to -2 dBi.

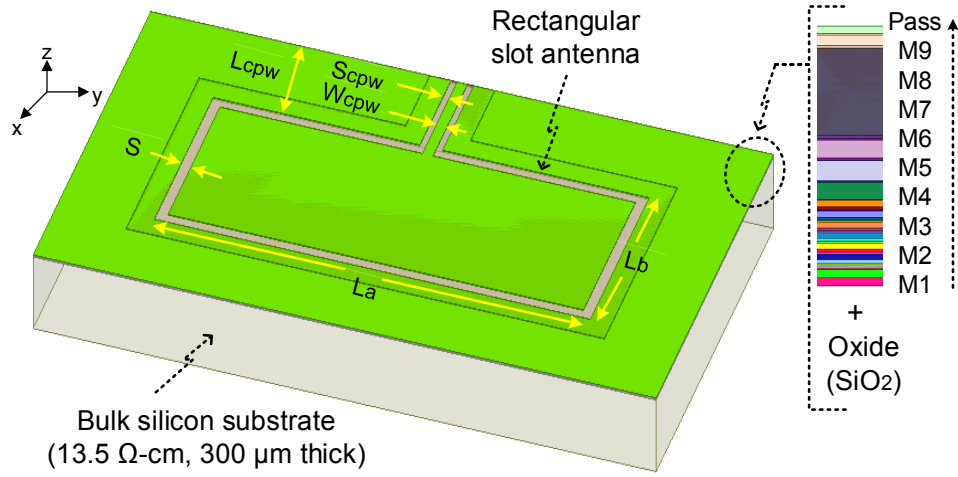


Figure 6.3: Illustration of the proposed rectangular slot antenna on CMOS process.

Rectangular slot-ring antennas are designed in our work, using CPW feed lines. The rules defined in [76] are used to design the slot ring. The resonant frequencies of both antennas are primarily determined by the mean perimeter of their respective rectangular-ring slots. The initial slot width is selected to be around $\lambda_r/10$ (λ_r : wavelength) to avoid the appearance of a leaky-wave mode.

Fig .6.3 illustrates the proposed configuration for the on-chip slot antenna, which consists of a rectangular slot aperture with slot width S, length L_a and width L_b , implemented on the top metal layer (M9) and above a silicon dioxide (SiO_2) dielectric, between the top most metal layer (M9) and bottom metal layer (M1). The SiO_2 dielectric is therefore only around 5.5 μm , given the spacing between M1 and M9 in a typical CMOS chip. The 300 μm bulk silicon substrate has a low resistivity (13.5 $\Omega\text{-cm}$). The antenna is fed from the edge by a 50-ohm CPW line (W_{cpw} , $SCPW$). The dimensions are selected to have a resonance frequency at:

$$c/(2(L_a + L_b)\sqrt{\epsilon_{\text{eff}}}) \quad (6.1)$$

with c being the speed of light in free space, and ϵ_{eff} the effective dielectric constant for a slot line. To avoid a very low radiation efficiency, the bottom metal layer (M1) is generally not used as ground shielding between the insulator layers and the silicon substrate [80]. With the CPW structure, a large part of electromagnetic fields is directed in the air above the top metal layer. However, not using the bottom metal layer (M1) allows the antenna radiating more toward the low resistivity, high permittivity silicon substrate than if M1 were present, which translates into a severe degradation of gain and efficiency at mm-wave frequencies [81].

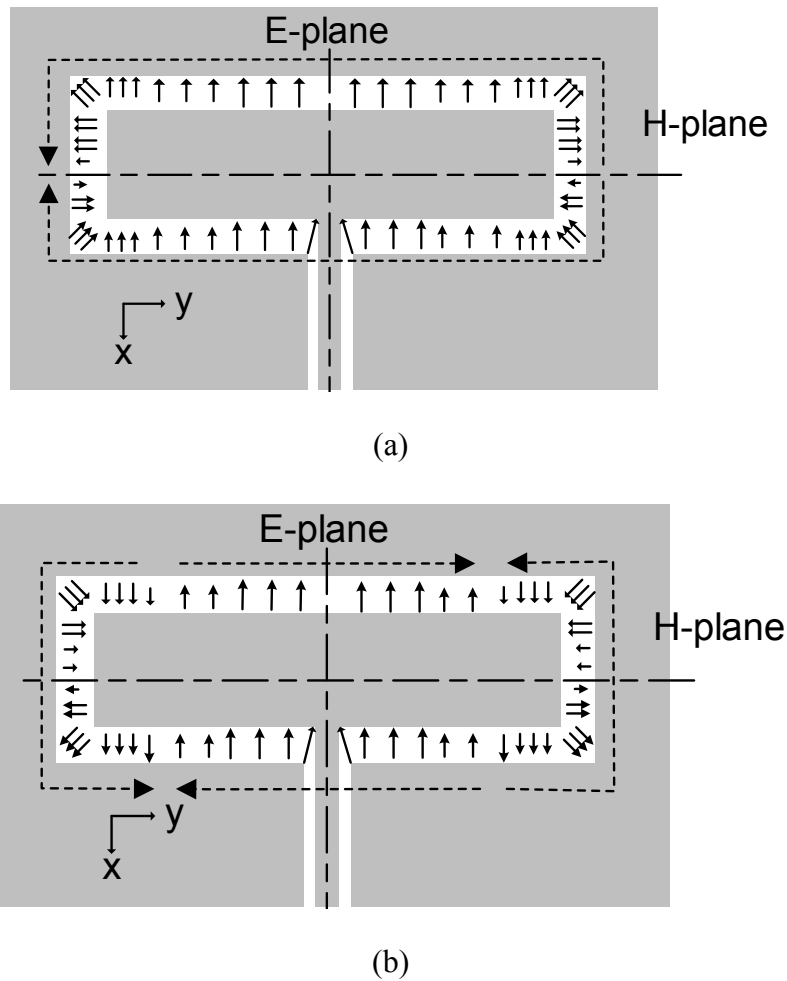


Figure 6.4: Illustration of E-field field distributions in the slot region of a rectangular -ring slot antenna: (a) the first resonant mode; and (b) the second resonant mode.

Fig. 6.4 illustrates the first and second resonant-mode equivalent electric field distributions of the rectangular ring slot antenna, which were sketched according to the results simulated using Ansoft High Frequency Structure Simulator (HFSSTM). The half-guided-wavelength routes of the magnetic currents are denoted by the short-dashed lines drawn beside the magnetic-current distributions. For the first resonant mode, the lower-side half-guided-wavelength route is slightly shorter than the upper-side one because of the shunt capacitance introduced by the feeding line.

As evidenced by the electric field distribution shown in Fig. 6.4(a), the horizontal electric field distribution is asymmetrical. However, the vertical electric field distribution is symmetrical along the horizontal direction. As a result, the rectangular ring slot antenna is linearly polarized. The E and H-planes are defined in Fig. 6.4. For the second resonant mode, there exist four half-wavelength routes for the magnetic currents, among which the one passing the feeding position has the shortest length. As shown by the electrical field distribution, it is identical in terms of orientation to that in the first mode.

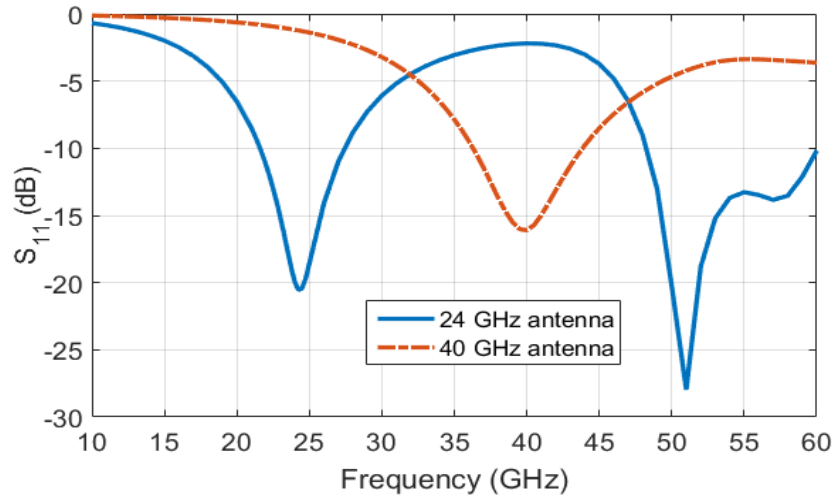


Figure 6.5: Reflection coefficient $|S_{11}|$ (dB) of the rectangular slot antennas at 24 GHz ($L_a=1.78$ mm, $L_b=0.89$ mm, $S=0.04$ mm, $W_{CPW}=0.05$ mm, $S_{CPW}=0.02$ mm, $L_{CPW}=0.16$ mm) and 40 GHz ($L_a=1.32$ mm, $L_b=0.43$ mm, $S=0.04$ mm, $W_{CPW}=0.05$ mm, $S_{CPW}=0.02$ mm, $L_{CPW}=0.39$ mm).

To validate the design, S-parameters of the proposed antennas (24 and 40 GHz) were simulated using Ansoft HFSS, as shown in Fig. 6.5. The bandwidths for a 10-dB reflection coefficient are 5.86 GHz (18.19 %) for the 24 GHz band and 11.87 GHz (21.29%) around the

corresponding harmonic frequency (48 GHz). However, a resonance around 57 GHz appears, corresponding to the resonance of the dipole slot antenna with a CPW-fed structure and La arm (as illustrated in Fig. 6.4(a)). The desired stop-band for this first antenna clearly appears around 40 GHz. For the second antenna, designed at 40 GHz, the bandwidth for a 10-dB reflection coefficient is 7.56 GHz (21.29%). These results suggest that the proposed antenna has exceptional quality factors and selectivity. The antennas cover the desired bandwidths around the two frequencies. The selectivity for each one may be increased by reducing their respective slot width S (as depicted in Fig. 6.3).

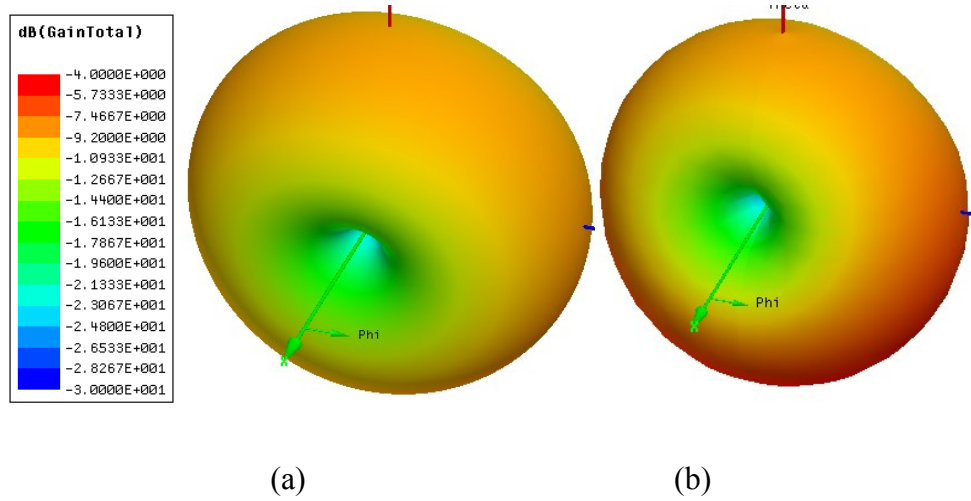


Figure 6.6: Simulated 3D radiation patterns of the dual-band rectangular slot antenna: (a) 24 GHz, (b) 40 GHz.

The 3D radiation patterns of the proposed antennas are shown in Fig. 6.6. For the 24 GHz antenna, the radiation in the E-plane (xz plane) is quasi-isotropic with a variation of 2dB in the level (2 dB of cross-polarization level) achieving -8 dBi of gain. The 3-dB beam width over the H-plane (yz plane) is about 65 degree. For the 40 GHz antenna, the 3-dB beam widths are 360 (quasi-isotropic) and 60 degree in the E-plane (xz plane) and H-plane (yz plane). For the 40 GHz antenna, the cross polarization level is about 20 dB with a gain of -5 dBi. The two frequencies share a very similar pattern with different gain (the same gain aperture efficiency) and they have the same polarization planes.

6.2.2 Dual-Frequency Co-centered Slot Antenna

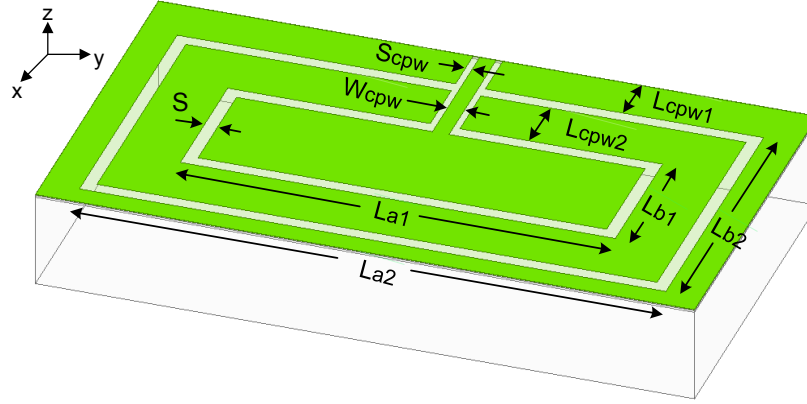


Figure 6.7: Illustration of the proposed dual-band rectangular slot antenna on CMOS process.

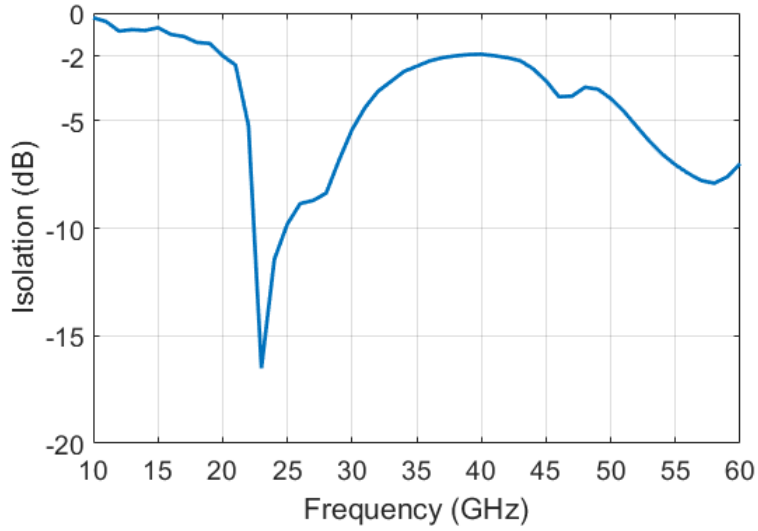
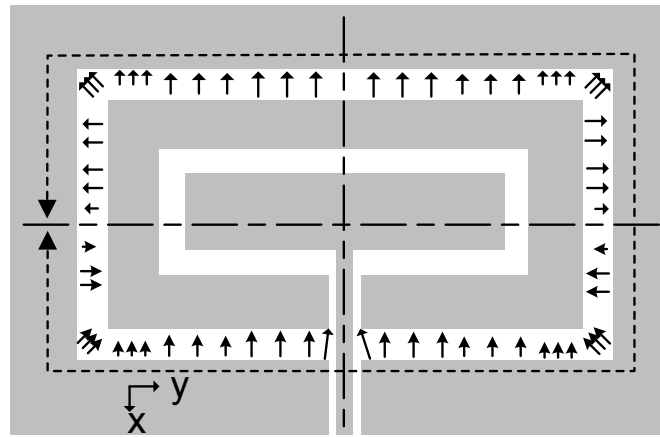


Figure 6.8: Transmission from the common input port to the 40 GHz rectangular slot.

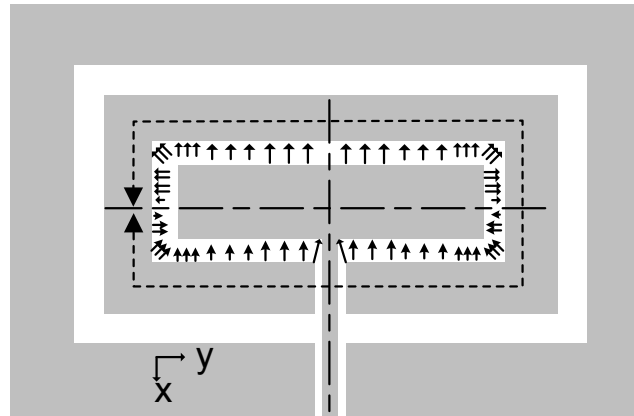
The geometries of the proposed CPW-fed dual-frequency rectangular-ring slot antennas are shown in Fig. 6.7. The outer slot loop perimeter is used to fix the operating lower frequency and the inner one fixes the higher band.

By adjusting the widths of the slots and the length of the arm, at the first band (24 GHz) all the energy is radiated. At the higher band (40 GHz) the energy is directed to the inner loop of the

proposed antenna. As demonstrated in Fig. 6.8, the energy from the external port to a virtual port defined at the input of the inner rectangular slot is small at 24 GHz, whereas the same figure indicates a coupling of 2 dB at 40 GHz. This demonstrates a good isolation of the 24 GHz antenna from a 40 GHz excitation at the external port, necessary for a dual-band operation. (Losses at this frequency represent 80 % of this value). It implies also that both antennas can be excited with a good impedance matching. Moreover, a small shift of both resonant frequencies (e.g. 21.5 GHz instead of 24 GHz, as indicated from Fig. 6.8) is justified by the interaction between the two slots.



(a)



(b)

Figure 6.9: E-field field distributions in the slot region of a rectangular slot antenna: (a) the first resonant mode; and (b) the second resonant mode.

Fig. 6.9 shows a sketched representation of the electric-field distribution for the CPW-fed dual-frequency rectangular-ring slot antenna, based on HFSS simulation results. Using this electromagnetic simulator, design parameters for both antennas were optimized. Since each resonant point relates to one parameter exclusively, parameters for each rectangular slot are optimized at a time to place the two frequencies at the anticipated points to meet different requirements. In the last steps, adjusting the frequencies and matching the input impedance were achieved by the tuning of the width of the two slots.

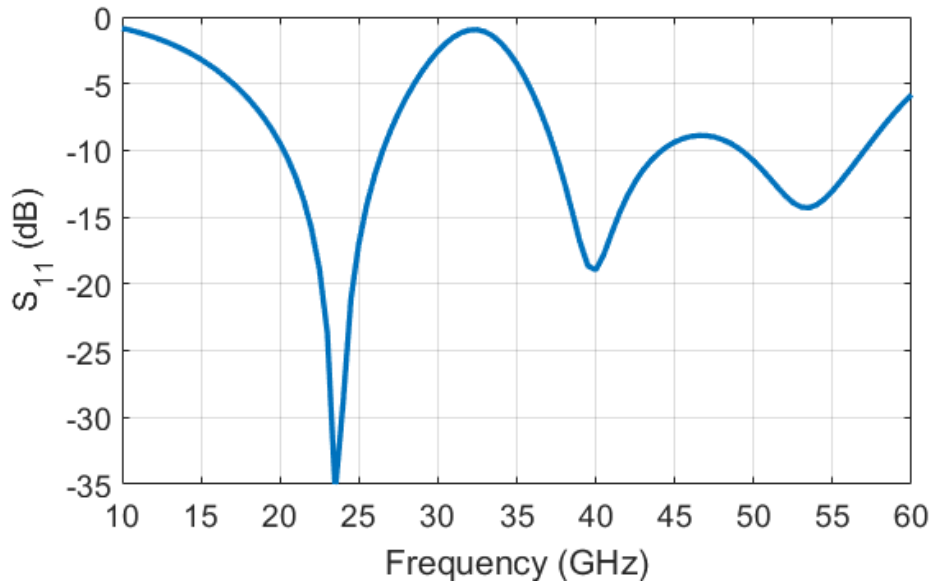


Figure 6.10: Reflection coefficient $|S_{11}|$ (dB) of the dual-band rectangular slot antenna ($L_{a1}=1.78$ mm, $L_{b1}=0.89$ mm, $L_{a2}=1.32$ mm, $L_{b2}=0.43$ mm, $S=0.04$ mm, $W_{CPW}=0.05$ mm, $S_{CPW}=0.02$ mm, $L_{CPW1}=0.16$ mm, $L_{CPW2}=0.19$ mm).

To validate the design procedure, S-parameters of the proposed antenna were simulated with HFSS. The bandwidths for a 10-dB reflection coefficient are 6.3 GHz (15.42%) and 6.8 GHz (16.6%) for the 24 GHz and 40 GHz antennas respectively, as shown in Fig .6.10.

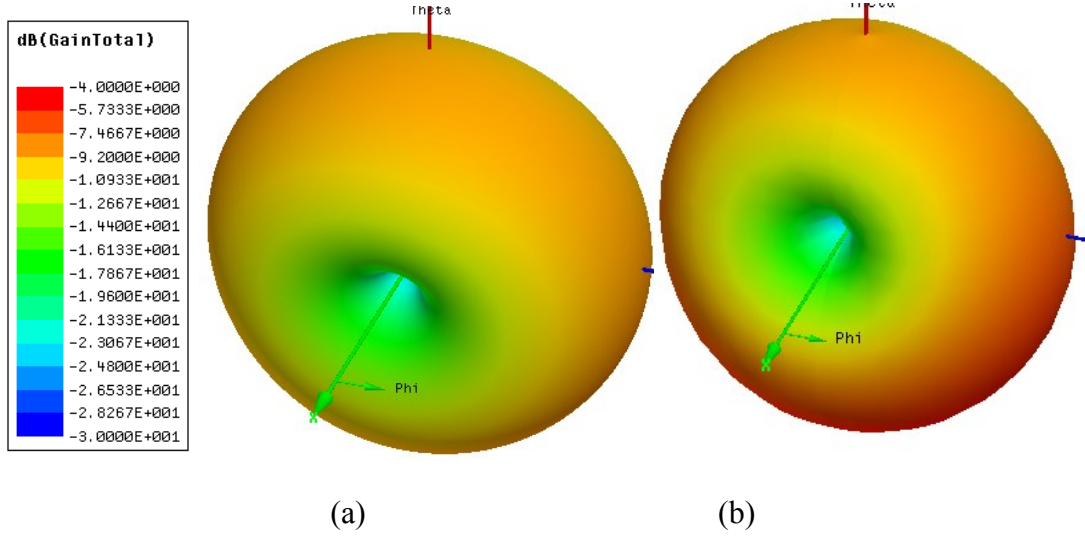


Figure 6.11: Simulated 3D radiation patterns of the dual-band rectangular slot antenna: (a) 24 GHz, (b) 40 GHz.

The radiation patterns of the proposed antenna are shown in Fig. 6.11 for the two frequencies. The gain, the 3-dB beam widths in the E-plane (xz plane) and H-plane (yz plane) are almost the same as in the case of the two separate antennas, with a small reduction in the case of the 24 GHz antenna. To obtain the proper resonance frequencies, the areas were reduced, while the perimeters were kept constant. The cross polarization level is about 38 and 25 dB for the 24 GHz and 40 GHz bands, respectively.

6.3 DRA-Loaded, Dual-Frequency, Co-centered Slot Antenna

The gain achieved by the dual-frequency antenna is not sufficient to cover the required MMID functionalities and ranges. A gain enhancement mechanism should be used to overcome this limit. Different off-chip gain enhancement methods combined with CMOS antennas have been proposed in the literature, for example, artificial dielectric layer (ADL) in [78] and stacked dielectric resonators (DRs) in [82]. Our proposed technique combines a slot antenna and a dielectric resonator antenna (DRA) to effectively increase the gain without compromising miniaturization,

nor efficiency. In our DR-slot hybrid antenna structure, the two radiating resonators (DRA and rectangular slot resonator) are tightly stacked together, offering more flexibility and direct compatibility with different mounting surfaces.

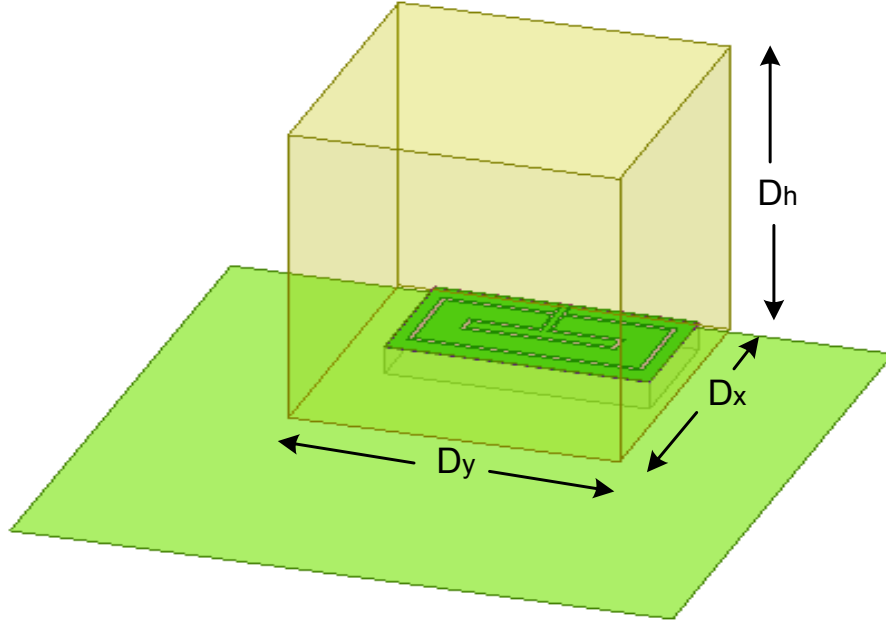


Figure 6.12: Geometry of the proposed DRA.

As shown in Fig. 6.12, a rectangular dielectric resonator antenna of dimensions $D_x \times D_y \times D_h$ is placed on a large metallic (PEC) ground plane. The high relative permittivity material $\epsilon_r=9.6$ is used. Mainly, this high permittivity substrate reduces the effect of the bulk silicon substrate on the gain. The coupling level can be adjusted through the positioning of the DRA above the slot antenna ring. The coupling behavior of the slot ring is similar to that of the coaxial probe, but the rectangular slot antenna structure offers the advantage of being nonobtrusive [83]. The dielectric block is generally centered on the coupling slot, and the slot centered above the under-passing microstrip feed line as in [83] and [84]. In [85], a slot-coupled rectangular DRA design was presented, wherein the dielectric resonator has a square base, but it is markedly offset with respect to the coupling slot. The dual-band rectangular slot used allows a coupling of the field to the DRA mode in a non-centered configuration (offset in x direction).

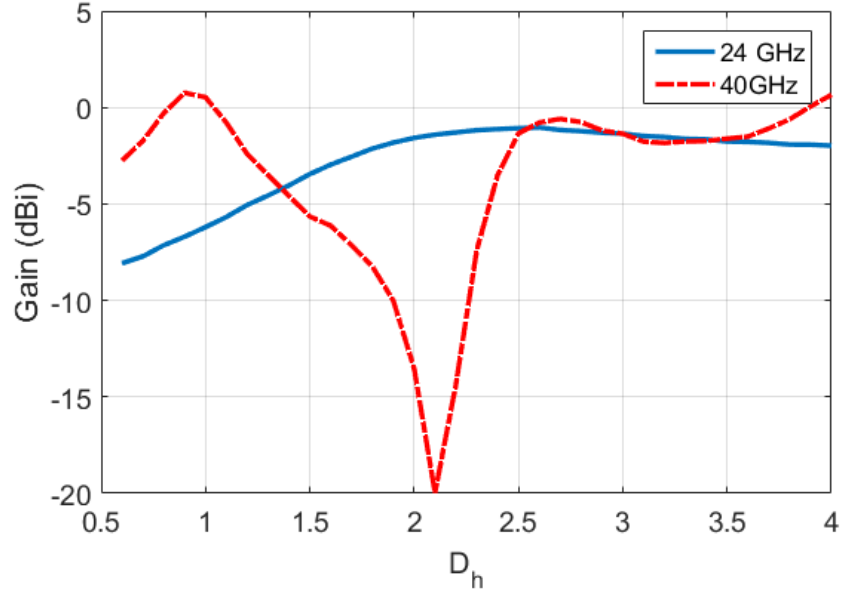


Figure 6.13: Gain .vs. DR thickness D_h .

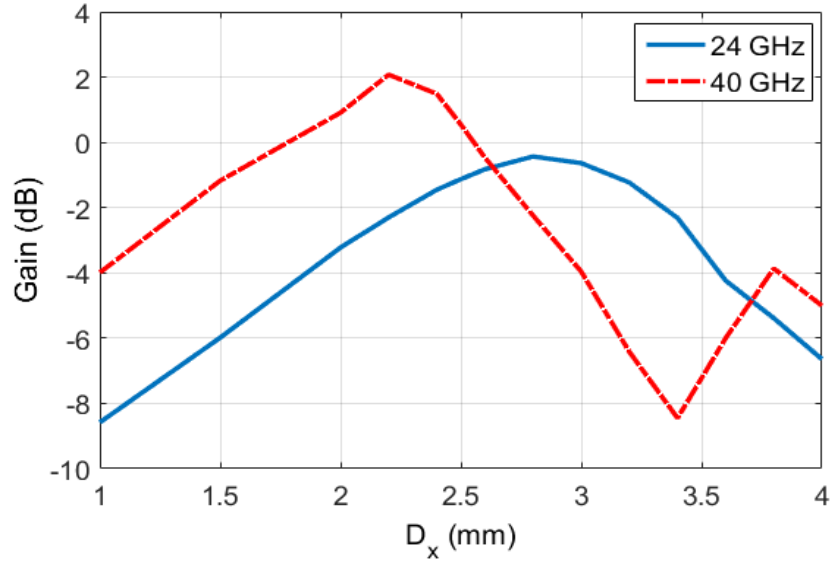


Figure 6.14: Gain .vs. DR dimension D_x .

As shown in Fig. 6.13, the peak of the gain for the 24 GHz band is achieved with a thickness $D_h=2.5$ mm. For the 40 GHz band, the gain peak is achieved with D_h around 1. In both cases, the probe is exciting the TE_{111} fundamental mode of the rectangular DRA. At $D_h=2.75$ mm, the 40 GHz antenna shows another gain maximum. The effect of parameter D_x on the gain is plotted in

Fig. 6.14. For the 24 GHz band, the gain reaches the maximum at $D_x=2.75$ mm and for the 40 GHz band at $D_x=2.2$ mm. As per the system-level analysis provided in the Introduction section, a 0 dBi gain is required at 40 GHz, while there is a more flexibility at 24 GHz, (i.e. from -6 to -1 dBi). Therefore, the gray zone in Fig. 6.14 defines a possible trade-off to achieve the two constraints.

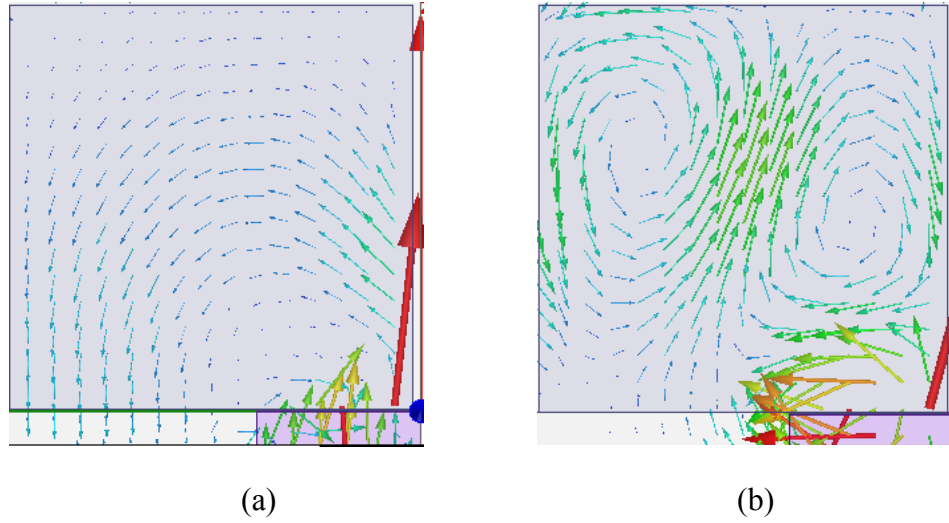


Figure 6.15: Electric field distribution of the proposed antenna: (a) 24 GHz, (b) 40 GHz.

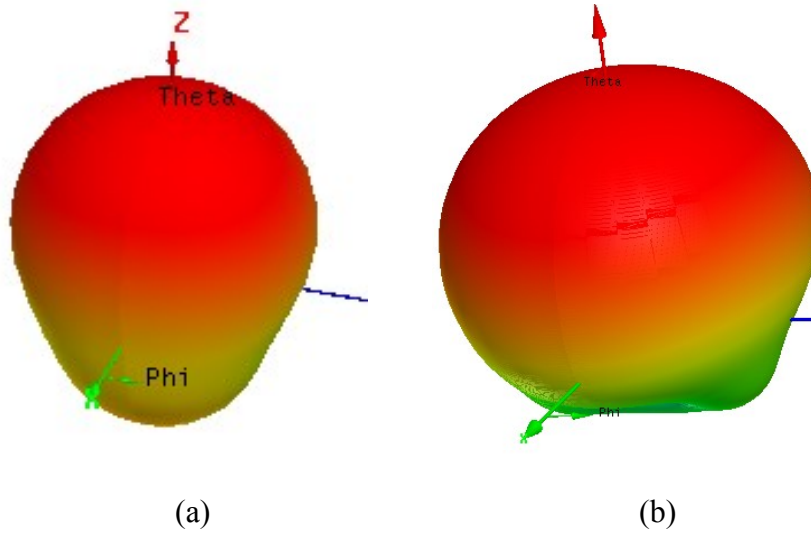


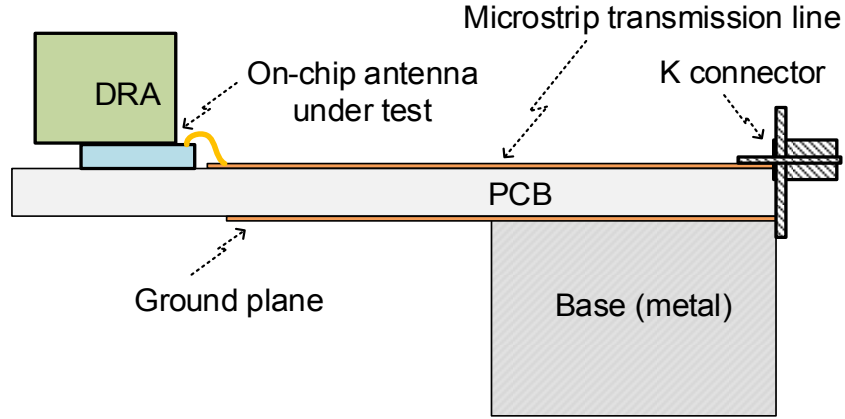
Figure 6.16: Simulated 3D radiation patterns of the dual-band rectangular slot antenna with DRA:
(a) 24 GHz, (b) 40 GHz.

The inner electric field distributions for the two resonant frequencies are illustrated in Fig. 6.15. The TE_{111} -like mode of the full-size DR is excited at the lower frequency of 24 GHz. Fig. 6.15 (b) shows that a TE_{121} -like mode, which operates at a frequency close to the upper band at 40 GHz, and is attributed to the full-size DR physical and electrical characteristics.

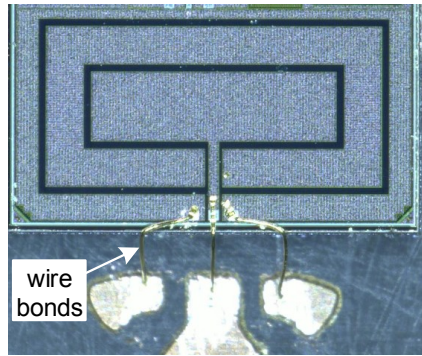
The radiation patterns of the proposed antenna are shown in Fig. 6.16. Clearly, the proposed antenna transfers from omnidirectional radiation to unidirectional radiation. As these results also show, with the addition of the DRA, the peak gain increases from -8 dBi to 0 dBi in the 24 GHz band, and to 1 dBi in the 40 GHz band. The front-to-back ratio is about 10 dB and 18 dB, respectively, and the cross polarization at 50 dB.

6.4 Antenna Measurements

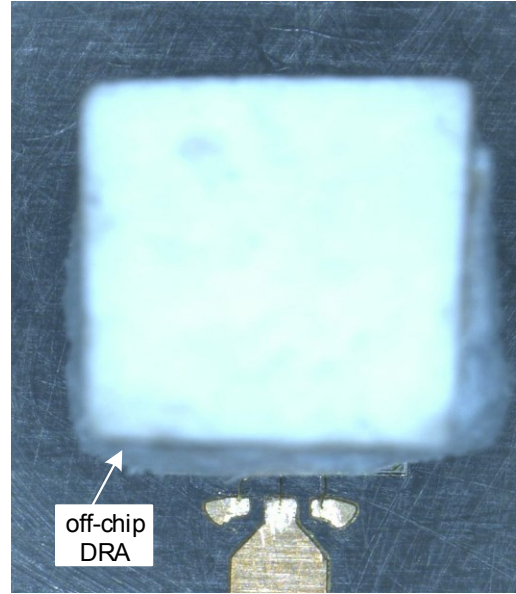
The antenna prototype was fabricated using a standard 65-nm bulk CMOS process and tested to validate the antenna properties. The antenna has an area of $2 \times 1 \text{ mm}^2$ including the bond pads. Unlike other proposed on-chip antennas where measurements are generally carried out on-wafer, Fig. 6.17 (a) shows our measurement setup, intended for measurements with a complete test assembly. The on-chip antenna under test is mounted on a PCB. A K-connector interfaces with a 50 ohm microstrip line that is connected to the on-chip antenna. This setup allows characterizing the on-chip antenna using a network analyzer in an anechoic chamber. The antenna was connected to the microstrip line using a wire-bonding technique realized in our Poly-Grames Research Center. The DR is manually mounted on the chip using non-conductive epoxy glue, with a careful alignment thanks to reference marks on the PCB. The PCB and the on-chip antenna are supported by a metallic base and, to minimize the effect of this metallic base, the antenna is mounted at 7 mm away from it. Fig. 6.17(b) and (c) show the microphotograph of the fabricated antenna with and without DR, respectively. The resonator has dimensions $2.5 \times 2.5 \times 2.5 \text{ mm}^3$ on a square metallic ground plane of dimensions $5 \text{ mm} \times 5 \text{ mm}$. Underneath the ground plane is a thin dielectric substrate of relative permittivity $\epsilon_r = 2.9$ and thickness $d = 0.5 \text{ mm}$.



(a)



(b)



(c)

Figure 6.17: Radiation measurement setup of the fabricated on-chip dual-band slot antenna ($L_a=1.78$ mm, $L_b=0.89$ mm, $S=0.04$ mm, $W_{CPW}=0.05$ mm, $S_{CPW}=0.02$ mm, $L_{CPW}=0.16$ mm) and 40 GHz ($L_a=1.32$ mm, $L_b=0.43$ mm, $S=0.04$ mm, $W_{CPW}=0.05$ mm, $S_{CPW}=0.02$ mm, $L_{CPW}=0.39$ m) (a) block diagram; (b) die microphotograph of the fabricated antenna without DR; (c) antenna with DR.

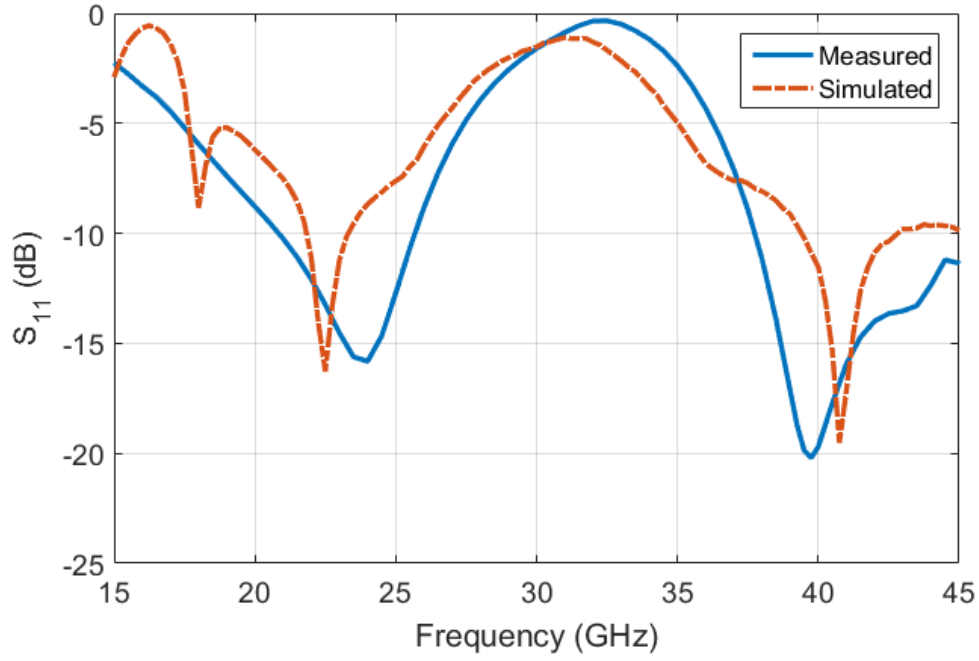
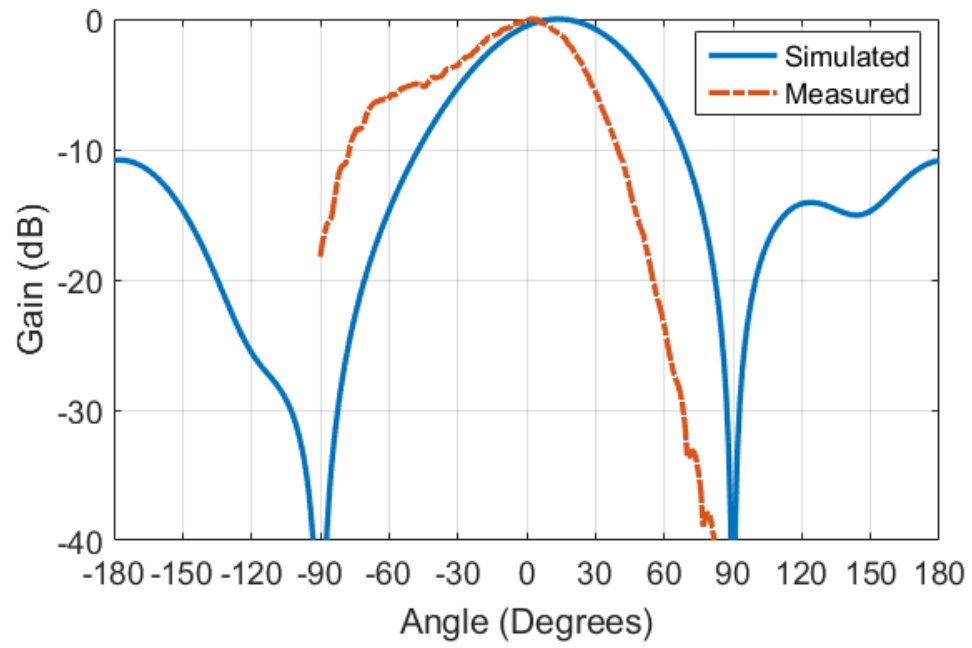
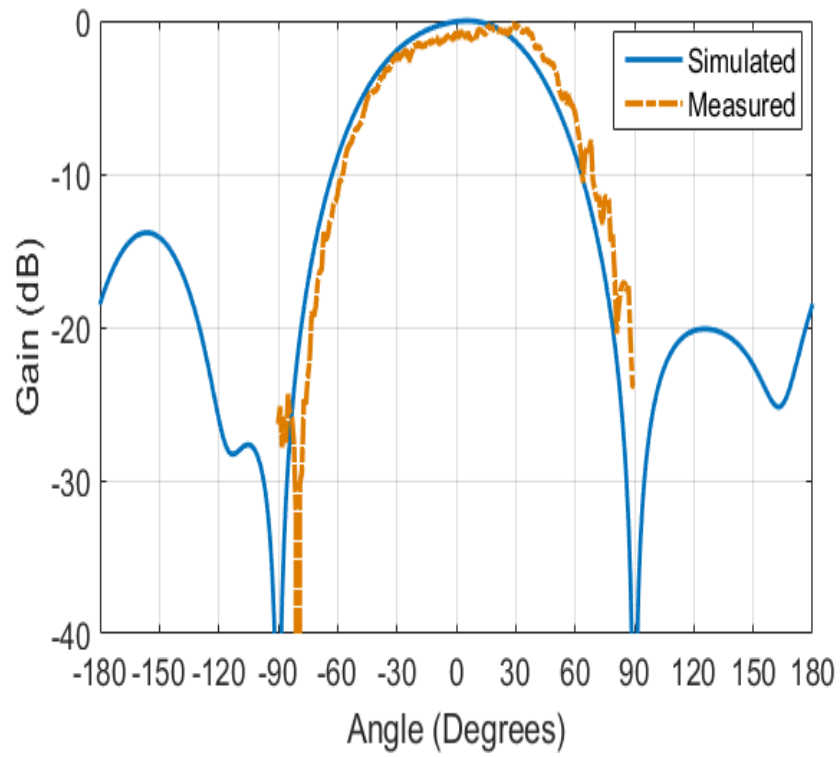


Figure 6.18: Reflection coefficient $|S_{11}|$ (dB) of the antenna (simulated and measured).

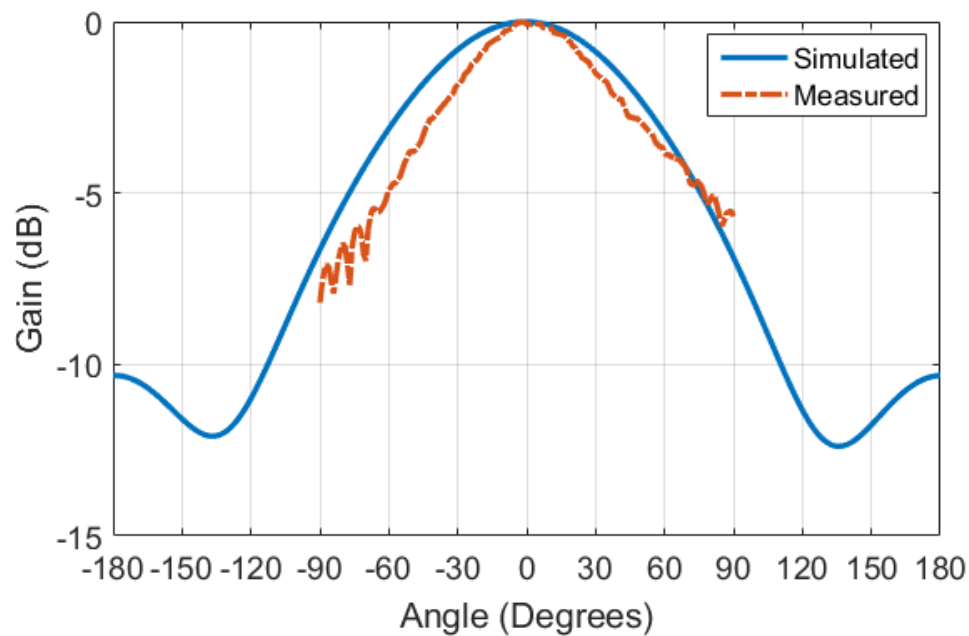
Simulated and measured return loss values of the proposed antenna are plotted against frequency in Fig. 6.18. It is observed that the antenna resonates at two distinct frequencies, 24 and 40 GHz with bandwidths of 23 % (20.5-25.5 GHz) and 17 % (38-45 GHz), respectively. Small shifts are observed at 24 GHz (down) and at 40 GHz (up). Note that the K-connector used is intended for measurements up to 40 GHz, whereas our measurements extend to beyond 45 GHz.



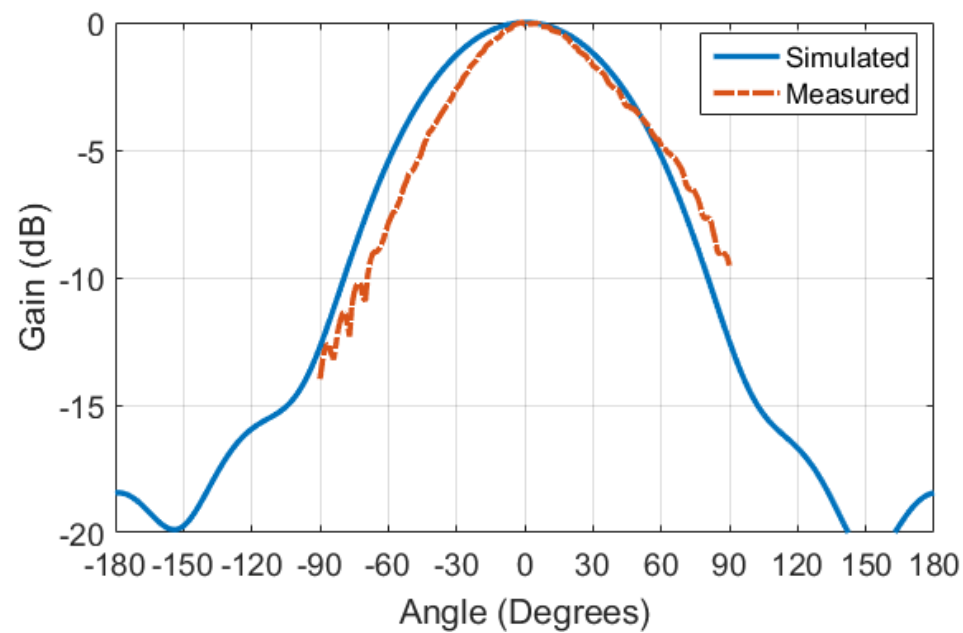
(a)



(b)



(c)



(d)

Figure 6.19: Measured and simulated radiation patterns (a) H-plane 24 GHz, (b) H-plane 40 GHz, (c) E-plane 24 GHz, (d) E-plane 40 GHz.

The radiation patterns of the proposed antenna are shown in Fig. 6.19. Simulated and measured radiating results are quite similar, and show that the antenna radiation patterns are successfully converted from omnidirectional-like radiation to unidirectional radiation, as explained in the preceding section. For the 24 GHz resonance, the 3-dB beam widths are 120 and 65 degree in the E-plane (xz plane) and H-plane (yz plane) measurements and 90 and 50 degree in the measured counterparts. For the 40 GHz resonance, the simulated 3-dB beamwidth are 90 and 80 degree in the E-plane (yz plane) and H-plane (xz plane), respectively (74 and 80 in the measurement). The measured radiation patterns are not as symmetric as the simulated ones, with a small shift in the 0 degree direction especially for the 24 GHz frequency. The measured peak gain is about -1 dBi for the 24 GHz band, and in the 40 GHz band, the antenna peak gain is about 0 dBi. Besides, Front-to-Back Ratio (FBR) at 24 GHz is enhanced from 10.4 dB to 17.5 dB as shown in the simulation. Our anechoic chamber facility covers from -90 to 90 degree.

6.5 Conclusion

In this paper, an on-chip dual-frequency rectangular slot antenna, suitable for a self-powered, single-die, active MMID tag has been proposed and demonstrated. The antenna was implemented using a 65-nm standard CMOS technology. In addition to a thoughtful design, analysis and optimization, the DRA sizing and the location of the feeding point are identified as key factors that enhance the radiation efficiency and the gain in both frequency bands of interest. The proposed on-chip antenna achieves a measured gain of -1 dBi at 24 GHz with a bandwidth of 19 %, 0 dBi at 40 GHz with a bandwidth of 20 %, and a radiation efficiency of 41 % and 31 %, at 24 GHz and 40 GHz, respectively. This supports and contributes to demonstrating the feasibility of a single CMOS-die MMID tag solution proposed in this work (Fig. 6.1).

CHAPTER 7 GENERAL DISCUSSION

Through the above-presented research achievements, this thesis presents innovative techniques which allow propelling the MMID technology in the front line of future wireless sensing, tracking, and communicating systems which are being discussed and developed worldwide. As part of the RFID evolution, the emerging mm-wave identification and the developed techniques enable new technological possibilities, such as a large number of different codes that can be ‘written’ on a tag, location sensing through narrow-beam antennas, and so on. They allow smaller hardware size, larger available bandwidth, longer bit streams, and higher spatial resolution. Moreover, the MMID concept is also compatible with future applications of mm-wave technology in wireless communications such as 5G and IoT platforms, especially information sharing of sensor networks and functional interplay among wireless functionalities. It is expected that 5G will be one of the core wireless infrastructure for IoT and future sensor communicator-combined smart systems.

MMID technology is evolving to wirelessly connect human to physical things in real time, and vice versa. Therefore, MMID will be one of the key enabling technologies in the IoT revolution. One example of the MMID-based technologies integrated in the IoT scheme is smart home. In a smart home, different information devices and various household applications communicate with each other, thereby forming a ubiquitous home network system, in order to help its residents to have more secure, efficient, productive, comfortable, and ergonomic live. MMID tags will be attached to consumable items (food packaging, clothes, etc.) and also household machinery (refrigerator, washing machine, etc.) will be equipped with an MMID reader. The MMID reader-enabled refrigerator, for example, can list out all the MMID tagged items inside the refrigerator and sends out reminders to handle certain groceries. Moreover, in the healthcare context, a similar list will be generated and biometrics adjusted according to real-time data from health-monitoring sensors. Smart home with MMID tags will be capable of managing energy-related functions, building control, and maintenance issues. A sensor tag could detect problems, trigger an alert, and provide information data to the homeowner on how to fix them. Such examples are just some of many MMID-enabled applications that would become common in a smart home. The MMID system proposed in this thesis goes beyond the stereotype of a homeowner who can monitor his

house on a smartphone and verify the status of interior devices such as security alarm or heating system. In parallel, wearable and no-contact healthcare MMID devices can monitor resident blood pressure, heart rate, and other metrics (posture, activity, ECG, breathing...) and transmit data to the resident smartphone for self-use or to inform doctors/emergency personnel as part of a medical tele-monitoring system.

The extensive use of the MMID technology will involve a significant number of MMID sensors and tags. Sometimes, these MMID tags will need to be miniaturized, deployed in specific locations, which may require power to be wirelessly transmitted and efficiently harvested without resorting to laborious system maintenance and tedious battery replacement, and will need to rely on highly-secured data, low-cost, etc. The fully-integrated, high-data-rate, battery-free, yet active MMID system presented in this thesis has been demonstrated to be a solution to address the aforementioned factors which, prior to this work, were impeding a widespread adoption of the new generation of millimeter-wave identification technology on single-chip.

The operating range of the presented MMID system is essentially limited by the rectifier's sensitivity (the minimum incident power that the rectifier is able to convert into DC), which is mainly dictated by the threshold voltage of the rectifying transistors. Therefore, any improvement in the rectifier's sensitivity directly increases communication range. It is worth mentioning that the output of the rectifier is far from being a stable power supply due to the presence of spurious frequencies in the rectified voltage. Indeed, in real application scenarios such as the single-chip MMID tag presented in this thesis, a low-dropout voltage regulator is mandatory to provide a constant and stable DC power supply.

Antennas presented in chapter 5 were mainly chosen based on the feeding available at the CMOS die. U-shaped dipole antenna which offers a differential mode is connected to the differential rectifier for power harvesting. The antenna is folded in order to minimize the overall tag size. For down-link and up-link communications, two orthogonally polarized (about -30 dB of isolation) ring-slot antennas are used at 40-GHz. The ring-slot antenna with CPW feeding network fits well with the CPW connectivity available on the die. Antennas were designed using HFSS, taking into account the chip input/output parasitics and wire-bonds that connect antennas to the chip as well. Only simulation results for both folded dipole and ring-slot antennas are presented, with a quasi-infinite ground plane since the ground plane size of the entire system (the ceramic base) is much larger than the size of the antennas. The selectivity of the antennas was

experimentally verified and the antennas work perfectly at the designed frequencies (24 and 40-GHz). At these frequency bands, characteristics of the used ceramic substrate are quite well known and accurate. It is worthwhile noting, however, that the MMID system as presented in this thesis operates in a full-duplex mode, therefore requires two orthogonal antennas for data communication. However, by appropriately modifying the tag architecture and adding a low-power active circulator, a single antenna such as the on-chip rectangular slot antenna presented in chapter 6 would be used for both communications in a full-duplex mode. The rectangular slot antenna was mainly chosen because it offers both dual-frequency and dual-polarization possibilities.

A key to achieving accurate and good result performances (especially at these millimeter-wave bands) is optimizing the chip layout. The layout optimization is threefold: (1) In order to minimize losses associated to parasitic capacitances, the integrated NMOS transistors are imbedded in a deep n-well; distances between drain, polysilicon gate, and source contacts are increased; as well as the distances between metal interconnections for sidewall parasitic capacitances. (2) Multiple fingers and double gate connections with multiple contacts per side are used to lower gate resistance. (3) The top and thicker metal layer is used for longer interconnections and the inductors to minimize substrate losses, and therefore enhance the quality factor. In addition, distances between signal paths and the inductors are maximized to increase isolation and prevent loading effect that lowers both inductor's value and quality factor.

CHAPTER 8 CONCLUSION AND FUTURE WORKS

In this chapter, we briefly summarize our main achievements during the course of this thesis. There exist, however, some pending questions and extensions to the work presented in this thesis. In this regard, we also suggest some areas in which further research could be conducted.

8.1 Conclusion

It is worth reminding that the new generation of MMID technology developed in this thesis aims to lead to a high-data-rate single-chip transponder solution, a fully-integrated MMID tag without any external component whatsoever. Therefore, the components developed throughout the thesis are demonstrated using a 65-nm standard CMOS process, a technology of choice because of its low-cost, high frequency operation, low-power consumption, and high integration capability. This results in lower cost and smaller transponders as well, which are key barriers for a widespread adoption of the new MMID technology.

Chapter 1 and 2 review key notions of RFID technology, discusses wireless power harvesting using CMOS circuits platform, introduces millimeter-wave identification technology, and highlights motivation and the contributions made in this thesis.

Since the main objective in this thesis is to come out with a wirelessly self-powered MMID technology, in chapter 3, we firstly proposed a novel MMID reader-tag system for batteryless, yet active tags on single-chip that addresses the underlying technical challenges of self-powered RFIDs operating at millimeter-wave frequencies. Secondly, we provided a thorough study and a comprehensive analysis of mm-wave power harvesting using CMOS circuits, a key circuit block to the successful implementation of such proposed MMID system. Conventional CMOS rectifier techniques that have worked quite well at low frequencies suffer from higher losses at mm-wave frequencies. We proposed a differentially-driven cross-coupled mm-wave-to-DC rectifier with the highest ever achieved performances in terms of power conversion efficiency in such mm-wave bands. We proposed and analytically demonstrated that the effect of threshold voltage, leakage current, and the excessive losses associated to the excessive parasitic elements which are the main factors negatively impacting the rectifier's power conversion efficiency especially at mm-wave

bands, could be handled through proper components (transistors and capacitors) sizing and layout optimization. Based on both simulation and experimental results, we demonstrated that the proposed rectifier can efficiently harvest sufficient DC power (get rid of battery) using a low-cost and well-known commercial CMOS technology.

Since energy can now wirelessly be harvested even at mm-wave bands as demonstrated in chapter 3, in chapter 4, in particular, we proposed and extensively studied a novel injection-locked, zero-IF self-oscillating mixer (SOM) which acts as an ultra-low-power mm-wave transceiver that could rely only on the rectified DC power. We analyzed conversion gains for both SOM's receiving and transmitting mode. We analytically demonstrated that conversion gain highly depends on the SOM's circuit design parameters, DC power consumption, and the modulation index of the injection-locking signal regardless its input power level. We also investigated the impact of the injected signal on the SOM, and we showed that a mismatch between the carrier frequency of the injected signal and the SOM's natural oscillation frequency greatly affects the down-converted baseband signal as well as the transmitted (up-converted) signal. The obtained performances (simulation and experimental results) confirmed the analytical results, and justified the potential use of the proposed SOM for an extremely-low-power consumption mm-wave CMOS transceiver such as what is required in self-powered active MMIDs.

In chapter 5, we mainly focused on proposing and investigating the feasibility of a single MMID tag chip (an all-in-one solution). Among various single-chip solution techniques, we chose the antenna-in-package (AiP) based solution which shows significant miniaturization capability and acceptable implementation complexity. We developed and implemented on a single-die an MMID tag transceiver with the capability of wirelessly harvesting and providing energy to the tag (self-powered). In order to tackle the assembly challenge between the die and the developed off-chip antennas (AiP concept), we proposed and experimentally demonstrated that an optimized wire bond still works quite well even at mm-wave bands. Experimental measurements were carried-out in free-space, and we demonstrated that the tag wirelessly collected its energy, received data, and transmitted back its data at mm-wave frequencies for all communications. The novel proposed, single-chip MMID tag is low-cost (it is self-contained and does not require any maintenance), miniature (therefore enabling novel applications), has a high data-rate communication capability (could potentially be used in a data streaming communication system), and has an energy autonomy (it is powered by the harvested energy).

Motivated by the fact that the antenna-in-package based solution discussed in chapter 5 suffers from packaging parasitics and chip-to-package interconnection losses, in chapter 6, we proposed and investigated the single-die solution where antennas are also integrated on the same bulk silicon substrate with other MMID tag's circuit blocks. First of all, on the system level point of view, we proposed and showed that the single-antenna solution in the tag as well as in the reader side tackles the energy transfer efficiency and the accuracy of line of sight between the reader's and the tag's antennas especially in a such multi-frequency and short-range reader-tag MMID system. Secondly, on the tag side, we mainly focused on proposing and demonstrating a size-reduced on-chip, dual-frequency rectangular slot antenna, implemented on a standard bulk silicon substrate. Given the nature of the CMOS process, the on-chip antenna lies between a lossy silicon substrate and the air which drastically affects the antenna radiation efficiency. We, therefore, proposed and showed that by loading the antenna with an optimized dielectric resonator greatly enhanced the antenna's radiation pattern and efficiency for both frequency bands. Through the obtained experimental and simulation results, which are in a good agreement, we demonstrated the feasibility of a single-die (a CMOS-only) and pinless MMID tag. The proposed single-die tag is a low-cost and compact (miniature) solution with no external components nor packaging whatsoever.

8.2 Future works

We have made an effort to address the issues of millimeter-wave identification and we have studied the feasibility of a high-data-rate, fully-integrated, and active μ RFID technology. Nonetheless, more research and development activities are required to prompt new applications and a massive adoption of this MMID technology.

1. Contrary to the proposed MMID system in this thesis, in a majority of applications, it is not possible to wait until the tag is in proximity of the interrogator before it can collect the power required for the sensor to work. The tag therefore needs its own internal power source. Therefore, energy harvesting approaches dealing with mixed techniques that combine different energy sources (RF, kinetic, and others), would be an interesting topic to explore.

2. Since the initial work of studying and demonstrating the feasibility of a high-data-rate, single-chip, active RFID tag that operates at millimeter-wave frequencies is already done in this thesis, we may now envision the sensing and detection of a variety of physical parameters. In the next decade, an increased emergence of micro and nano-sensor materials that implement novel functionalities are expected, thanks to cost-effective fabrications. The main problem lies in the amount of energy necessary for the sensors to work properly. By appropriately modifying the tag architecture and tackling the underlying energy challenge, sensors or other devices such as memories could be integrated and this represents a synergistic research framework that will yield added value.
3. The use of an RF-oriented technology that includes zero- V_{th} (threshold voltage) with RF model transistors, lesser leakage current, and lesser substrate losses such as the SOI (Substrate On-Insulator) CMOS technology would enhance the rectifier's sensitivity (communication range), power consumption for the mm-wave transceiver, and the on-chip antenna's efficiency.

REFERENCES

- [1] T. S. Rappaport, "Millimeter wave mobile communications for 5G cellular: It will work!," *IEEE Access*, vol. 1, no. 1, pp. 335-349, 2013.
- [2] P. Bhartia, K. V. S. Rao, and R. S. Tomar, Millimeter-wave microstrip and printed circuit antennas. Artech House, 1991.
- [3] P. Pursula et al., "60-GHz Millimeter-Wave Identification Reader on 90-nm CMOS and LTCC," *IEEE Trans. Microw. Theory Techn.*, vol. 59, no. 4, Apr. 2011.
- [4] D. M. Dobkin, "The RF in RFID: Passive UHF RFID in Practice," Elsevier & Newnes 2008.
- [5] A. Giry, J.-M. Fournier, and M. Pons, "A 1.9 GHz low voltage CMOS power amplifier for medium power RF applications," *IEEE Radio Freq. Integr. Circuits (RFIC) Symp., Dig.*, pp. 121-124, 2000.
- [6] S. R. M. Baghaei-Nejad, K. Mohammadpour-Aghdam, G. A. E. Vandebosch, L. Zheng, and G. Gielen, "Far-Field On-Chip Antennas Monolithically Integrated in a Wireless-Powered 5.8-GHz Downlink/UWB Uplink RFID Tag in 0.18- μ m Standard CMOS," *IEEE J. Solid-State Circuits*, vol. 45, no. 9, pp. 1746–1758, Sept. 2010.
- [7] L. Hanil and S. Mohammadi, "A Subthreshold Low Phase Noise CMOS LC VCO for Ultra Low Power Applications," *IEEE Microw. Wireless Lett.*, vol. 17, pp. 796-798, 2007.
- [8] C. Yao and W. Hsia, "A -21.2-dBm Dual-Channel UHF Passive CMOS RFID Tag Design," *IEEE Trans. Circuits Syst. I, Reg. Papers*, vol. 61, no. 4, pp. 1269-1279, Apr. 2014.
- [9] G. Gosset and D. Flandre, "A Very High Efficiency Ultra-Low-Power 13.56MHz Voltage Rectifier in 150nm SOI CMOS," *IEEE Radio Freq. Integr. Technology (RFIT) Symp.*, pp. 347-350, 2009.
- [10] J. A. Hagerty and Z. Popovic, "An Experimental and Theoretical Characterization of A Broadband Arbitrarily-Polarized Rectenna Array," in *Microw. Symp. Dig., IEEE MTT-S International*, vol.3, pp. 1855-1858, 2001.
- [11] S. Hashemi, et al., "Fully-Integrated Low-Voltage High-Efficiency CMOS Rectifier for Wirelessly Powered Devices," in *Circuits and Systems and TAISA Conference, NEWCAS-TAISA '09. Joint IEEE North-East Workshop on*, pp. 1-4, 2009.

- [12] A. Shameli, A. Safarian, A. Rofougan, M. Rofougaran, and F. De Flaviis, "Power Harvester Design for Passive UHF RFID Tag Using a Voltage Boosting Technique," *IEEE Trans. Microw. Theory Techn.*, vol. 55, no. 6, pp. 1089–1096, Jun. 2007.
- [13] N. Soltani and Y. Fei, "A High-Gain Power-Matching Technique for Efficient Radio-Frequency Power Harvest of Passive Wireless Microsystems," *IEEE Transactions on, Circuits and Systems I: Regular Papers*, vol. 57, pp. 2685-2695, 2010.
- [14] T. Umeda, H. Yoshida, S. Sekine, Y. Fujita, T. Suzuki, and S. Otaka, "A 950-MHz rectifier circuit for sensor network tags with 10-m distance," *IEEE J. Solid-State Circuits*, vol. 41, no. 1, pp. 35–41, Jan. 2006.
- [15] K. Kotani, A. Sasaki, and T. Ito, "High-Efficiency Differential-Drive CMOS Rectifier for UHF RFIDs," *IEEE J. Solid-State Circuits*, vol. 44, no. 11, pp. 3011–3018, Nov. 2009.
- [16] P. T. Theilmann, C. D. Presti, D. Kelly, and P. M. Asbeck, "Near Zero Turn-on Voltage High-Efficiency UHF RFID Rectifier in Silicon-on-Sapphire CMOS," in *Proc. IEEE Radio Frequency Integrated Circuits Symposium (RFIC)*, Anaheim, CA, May 23-25, 2010, pp. 105-108.
- [17] L. Triet, M. Karti, and S. F. Terri, "Efficient Far-Field Radio Frequency Power Conversion System for Passively Powered Sensor Networks," in *Custom Integrated Circuits Conference, 2006. CICC '06. IEEE*, 2006, pp. 293-296.
- [18] Y. Jun, K. Wing-Hung, and T. Chi-Ying, "Analysis and Design Strategy of UHF Micro-Power CMOS Rectifiers for Micro-Sensor and RFID Applications," *IEEE Trans. Circuits and Systems I: Regular Papers*, vol. 54, pp. 153-166, 2007.
- [19] P. Pursula, T. Vähä-Heikkilä, A. Müller, D. Neculoiu, G. Konstantinidis, A. Oja, and J. Tuovinen, "Millimeter-Wave Identification, A New Short-Range Radio System for Low-Power High Data-Rate Applications," *IEEE Trans. Microw. Theory Tech.*, vol. 56, no. 10, pp. 2221–2228, Oct. 2008.
- [20] S. Preradovic, N. Karmakar, "Chipless millimeter wave identification (MMID) tag at 30 GHz," *Microwave Conference (EuMC), 2011 41st European*, pp.123-126, 10-13 Oct. 2011.
- [21] N. C. Karmakar and P. Chow Kay, "mm-wave chipless RFID tag for low-cost item tagging," *Asia-Pacific Microwave Conference Proceedings (APMC)*, pp. 1462-1465, 2011.

- [22] J. Li, T. Djerfai, F. Ren and K. Wu, "Chipless Substrate Integrated Waveguide Tag Using Time-Domain Reflectometry Technique for Millimeter-Wave Identification (MMID)", *European Microwave Conference*, London, UK, pp.1-4, 2016.
- [23] P. Pursula, F. Donzelli, and H. Seppä, "Passive RFID at Millimeter-Waves," *IEEE Trans. Microw. Theory Techn.*, vol. 59, no. 8, Aug. 2011.
- [24] S. Pellerano, J. Alvarado, and Y. Palaskas, "A mm-wave power harvesting RFID tag in 90 nm CMOS," *IEEE J. Solid-State Circuits*, vol. 45, no. 8, Aug. 2010.
- [25] P. Koert and J. T. Cha, "Millimeter wave technology for space power beaming," *IEEE Trans. Microw. Theory Techn.*, vol. 40, no. 6, pp. 1251-1258, Jun. 1992.
- [26] T. W. Yoo and K. Chang, "Theoretical and experimental development of 10 and 35 GHz rectennas," *IEEE Trans. Microw. Theory Techn.*, vol. 40, no. 6, pp. 1259-1266, Jun. 1992.
- [27] J. O. McSpadden, T. Yoo, and K. Chang, "Theoretical and experimental investigation of a rectenna element for microwave power transmission," *IEEE Trans. Microw. Theory Techn.*, vol. 40, no. 12, pp. 2359-2366, Dec. 1992.
- [28] Y. J. Ren, M. Y. Li, and K. Chang, "35 GHz rectifying antenna for wireless power transmission," *Electron. Lett.*, vol. 43, no. 11, pp. 602-603, May. 2007.
- [29] K. Hatano, N. Shinohara, T. Mitani, K. Nishikawa, T. Seki, and K. Hiraga, "Development of Class-F Load Rectennas," *Microwave Workshop Series on Innovative Wireless Power Transmission: Technology, Systems, and Applications (IMWS)*, 2011 *IEEE MTT-S International*, pp. 251-254, May 2011.
- [30] M. Tiebout, H. Wohlmuth, and W. Simburger, "A 1V 51 GHz fully-integrated VCO in 0.12 μm CMOS," in *Int. Solid-State Circuits Conf. Tech. Dig.*, pp. 300-301, Feb. 2002.
- [31] H.-K. Chiou and I.-S. Chen, "High-Efficiency Dual-Band On-Chip Rectenna for 35- and 94-GHz Wireless Power Transmission in 0.13- μm CMOS Technology," *IEEE Trans. Microw. Theory Techn.*, vol. 58, no. 12, Dec. 2010.
- [32] S. Farzeen, G. Ren, and C. Chen, "An ultra-low power ring oscillator for passive UHF RFID transponders," *Circuits and Systems, 53rd International Midwest Symposium*, pp. 558-561, 2010.
- [33] U. Karthaus and M. Fisher, "Fully integrated passive UHF RFID transponder IC with 16.7- μW minimum RF input power," *IEEE J. Solid-State Circuits*, vol. 38, no. 10, pp. 1602–1608, Oct. 2003.

- [34] J.-P. Curty, N. Joehl, C. Dehollain, and M. J. Declercq, "Remotely powered addressable UHF RFID integrated system," *IEEE J. Solid-State Circuits*, vol. 40, no. 11, pp. 2193–2202, Nov. 2005.
- [35] J. Essel, D. Brenk, J. Heidrich, R. Weigel, and D. Kissinger, "Large-Signal Measurements and Nonlinear Characterization of an Analog Frontend for Passive UHF CMOS RFID Transponders," *IEEE Trans. Microw. Theory Techn.*, vol. 61, no. 2, Feb. 2013.
- [36] Y. Yuan, W. Jie, S. Yin, and F. F. Dai, "A Fully Integrated 900-MHz Passive RFID Transponder Front End With Novel Zero-Threshold RF-DC Rectifier", *IEEE Trans. Ind. Electron.*, vol. 56, no. 7, pp. 2317-2325, Jul. 2009.
- [37] M. Brandl, J. Grabner, K. Keller, F. Seifert, J. Nicolics, S. Grabner, and G. Grabner, "A Low-Cost Wireless Sensor System and Its Application in Dental Retainers," *IEEE-J. Sensors*, vol. 9, no. 3, pp. 255-262, Mar. 2009.
- [38] L. Yang, L. J. Martin, D. Staiculescu, C. P. Wong, and M. M. Tentzeris, "Conformal Magnetic Composite RFID for Wearable RF and Bio-Monitoring Applications," *IEEE Trans. Microw. Theory Techn.*, vol. 56, no. 12, pp. 3223-3230, Dec. 2008.
- [39] S. Amendola, R. Lodato, S. Manzari, C. Occhiuzzi, and G. Marrocco, "RFID Tchnology for IoT-Based Personal Healthcare in Smart Spaces," *IEEE-J. Internet of Things*, vol. 1, no. 2, pp. 144-152, Apr. 2014.
- [40] A. Zaric, C. C. Caruz, A. M. de Matos, M. R. da Silva, J. R. Costa, and C. A. Fernandes, "RFID-based Smart Blood Stock System," *IEEE Antenna and Propagation Magazine*, vol. 57, no. 2, pp. 54-65, Apr. 2015.
- [41] P. burasa, N. G. Constantin, and K. Wu, "High-Efficiency Wideband Rectifier for Single-Chip Batteryless Active Millimeter-Wave Identification (MMID) Tag in 65-nm Bulk CMOS Technology," *IEEE Trans. Microw. Theory Techn.*, vol. 62, no. 4, pp. 1005-1011, Apr. 2014.
- [42] J. W Lee, N. D. Phan, D. H. Thai Vo, and V. H. Duong, "A Fully Integrated EPC Gen-2 UHF-Band Passive Tag IC Using an Efficient Power Management Technique," *IEEE Trans. Industrial Electronics*, vol.61, no. 6, Jun. 2014.
- [43] J. Y. Kim and W. Y. Choi, "30 GHz Self-Oscillating Mixer for Self-Heterodyne Receiver Application," *IEEE Microw. Wireless Lett.*, vol. 20, no. 6, Jun. 2010.

- [44] A. Liscidini, A. Mazzanti, R. Tonietto, L. Vandi, P. Andreani, and R. Castello, "Single-stage low-power quadrature RF receiver front-end: The LMV cell," *IEEE J. Solid-State Circuits*, vol. 41, no. 12, pp. 2832–2841, Dec. 2006.
- [45] H. K. S. Stanley and S. E. Carlos, "A Low-Noise Self-Oscillating Mixer Using a Balanced VCO Load," *IEEE Trans. Circuits Syst. I, Reg. Papers*, vol. 58, no. 8, pp. 1705–1711, Aug. 2011.
- [46] B. R. Jackson and C. E. Saavedra, "A dual-band self-oscillating mixer for C-band and X-band applications," *IEEE Trans. Microw. Theory Techn.*, vol. 58, no. 2, pp. 318–323, Feb. 2010.
- [47] P. Burasa, N. G. Constantin, and K. Wu, "Low-Power Injection-Locked Zero-IF Self-Oscillating Mixer for Self-Powered Millimeter-Wave Identification (MMID) Active Tag in 65-nm CMOS," *IEEE Radio Freq. Integrated Circuits Symp.*, Phoenix, AZ, USA, May 17–19, 2015.
- [48] B. Razavi, "A Study of Injection Locking and Pulling in Oscillators," *IEEE J. Solid-State Circuits*, vol. 39, no. 9, pp. 1415–1424, Sept. 2004.
- [49] I. Ali, A. Banerjee, A. Mukherjee, and B. N. Biswas, "Study of Injection Locking With Amplitude Perturbation and Its Effect on Pulling of Oscillator," *IEEE Trans. Circuits Syst. I, Reg. Papers*, vol. 59, no. 1, pp. 137–147, Jan. 2012.
- [50] E. Hegazi, H. Sjolund, and Asad A. Abidi, "A Filtering Technique to Lower LC Oscillator Phase Noise," *IEEE J. Solid-State Circuits*, vol. 36, no. 12, pp. 1921–1930, Dec. 2001.
- [51] T. Djerafi, K. Wu, A. Marque, and A. Ghiotto, "Chipless substrate waveguide tag for millimeter wave identification," *IEEE Millimeter waves (GSM) Global Symp.*, Montreal, QC, Canada, May 25–27, 2015.
- [52] P. Burasa, N. G. Constantin, and K. Wu, "Low-Power Injection-Locked Zero-IF Self-Oscillating Mixer for High Gbit/s Data-Rate Battery-Free Active μ RFID Tag at Millimeter-Wave Frequencies in 65-nm CMOS," *IEEE Trans. Microw. Theory Techn.*, vol. 64, no. 4, pp. 1055–1065, Apr. 2016.
- [53] Y. P. Zhang and Duixian Liu, "Antenna-on-Chip and Antenna-in-Package Solutions to Highly Integrated Millimeter-Wave Devices for Wireless Communications," *IEEE Trans. Microw. Theory Techn.*, vol. 57, no. 10, Oct. 2009.

- [54] C. Karnfelt, P. Hallbjorner, H. Zirath, and A. Alping, "High gain active microstrip antenna for 60-GHz WLAN/WPAN applications," *IEEE Trans. Microw. Theory Techn.*, vol. 54, no. 6, pp. 2593–2603, Jun. 2006.
- [55] A. Jerng and C. G. Sodini, "The impact of device type and sizing on phase noise mechanisms," *IEEE J. Solid-State Circuits*, vol. 40, no. 2, pp. 360–369, Feb. 2005.
- [56] S. Levantino, C. Samori, A. Zanchi, and A. L. Lacaita, "AM-to-PM conversion in varactor-tuned oscillators," *IEEE Trans. Circuits Syst. II, Analog Digit. Signal Process.*, vol. 49, no. 7, pp. 509–513, Jul. 2002.
- [57] Chia-Chin Liu and Chunhong Chen, "An Ultra-Low Power Voltage Regulator for RFID Application," *Circuits and Systems (MWSCAS), 2013 IEEE 56th International Midwest Symposium*.
- [58] M. Rebeiz, "Millimeter-wave and terahertz integrated circuit antennas," *Proc. IEEE*, vol. 80, no. 11, pp. 1748–1770, Nov. 1992.
- [59] R. Lampe, "Design formulas for an asymmetric coplanar strip folded dipole," *IEEE Trans. Antennas Propag.*, vol. AP-33, no. 9, pp. 1028–1031, Sep. 1985.
- [60] S. Raman and G. M. Rebeiz, "Single- and dual-polarized millimeter-wave slot-ring antennas," *IEEE Trans. Antennas Propag.*, vol. 44, no. 11, pp. 1438–1444, Nov. 1996.
- [61] G. Q. Luo, Z. F. Hu, L. X. Dong, and L. L. Sun, "Planar slot antenna backed by substrate integrated waveguide cavity," *IEEE Antennas Wireless Propag. Lett.*, vol. 7, pp. 236–239, Aug. 2008.
- [62] C. Koverman, "Next-Generation Connected Support in the Age of IoT: It's time to get proactive about customer support," *IEEE Consumer Electronics Magazine*, vol. 5, no. 1, pp. 69–73, Jan. 2016.
- [63] V. Moreno, M. A. Zamora and A. F. Skarmeta, "A Low-Cost Indoor Localization System for Energy Sustainability in Smart Buildings," *IEEE Sensors Journal*, vol. 16, no. 9, pp. 3246–3262, May, 2016.
- [64] K. Wu, P. Burasa, T. Djerafi, and N. Constantin, "Millimeter-wave identification for future sensing, tracking, positioning and communicating systems," *IEEE Millimeter waves (GSMM) Global Symp. & ESA workshop on millimeter-wave technique. and applications*, Espoo, Finland, June 6–8, 2016.

- [65] P. Burasa, T. Djerafi, N. G. Constantin, and K. Wu, "High-Data-Rate Single-Chip Battery-Free Active Millimeter-Wave Identification Tag in 65-nm CMOS Technology," *IEEE Trans. Microw. Theory Techn.*, vol. 64, no.7, pp.2294-2303, Jul. 2016.
- [66] T. Maeda et al., "A Low-Power Dual-Band Triple-Mode WLAN CMOS Transceiver," *IEEE J. Solid-State Circuits*, vol. 41, no. 11, pp. 2481–2490, Nov. 2006.
- [67] M. Zargari et al., "A Single-Chip Dual-Band Tri-Mode CMOS Transceiver for IEEE 802.11a/b/g Wireless LAN," *IEEE J. Solid-State Circuits*, vol. 39, no. 12, pp. 2239–2249, Dec. 2004.
- [68] Jie-Huang Huang, Jin-Wei Wu, Yi-Lin Chiou and C. F. Jou, "A 24/60GHz dual-band millimeter-wave on-chip monopole antenna fabricated with a 0.13- μ m CMOS technology," *Antenna Technology, 2009. iWAT 2009. IEEE International Workshop*, Santa Monica, CA, 2009, pp. 1-4
- [69] G. Chi, B. Li and D. Qi, "A dual-frequency antenna fed by CPW," *Proc. IEEE Antennas Propag. Soc. Int. Symp.*, pp. 459-462, 2005
- [70] Horng-Dean Chen and Hong-Twu Chen, "A CPW-fed dual-frequency monopole antenna," *IEEE Trans. Antennas Propag.*, vol. 52, no. 4, pp. 978-982, April 2004.
- [71] Jin-Sen Chen, "Dual-frequency annular-ring slot antennas fed by CPW feed and microstrip line feed," *IEEE Trans. Antennas Propag.*, vol. 53, no. 1, pp. 569-573, Jan. 2005.
- [72] G. C Wang and J. D. Xu, "Novel application of CPW in antenna design for dual-frequency operation," *Progress in Electromagn. Research Symp.*, Cambridge, USA, July 5-8, 2010.
- [73] A.-P. Saghati, J.-S. Batra, J. Kameoka and K. Entesari, "Miniature and reconfigurable CPW folded slot antennas employing liquid-metal capacitive loading," *IEEE Trans. Antennas Propag.*, vol. 63, no. 9, pp. 3798-3807, Sept. 2015.
- [74] J. Xu, Z. -N. Chen and X. Qing, "CPW center-fed single-layer SIW slot antenna array for automotive radars," *IEEE Trans. Antennas Propag.*, vol. 62, no. 9, pp. 4528-4536, Sep. 2014.
- [75] A. Mehdipour, K. M. Aghdam, R. Faraji-Dana and M. Kashani-Khatib, "A novel coplanar waveguide-fed slot antenna for ultrawideband applications," *IEEE Trans. Antennas Propag.*, vol. 56, no. 12, pp. 3857-3862, Dec. 2008.
- [76] W.-S. Chen and K.-L. Wong, "Dual-frequency operation of a coplanar waveguide-fed dual-slot loop antenna," *Microw. Opt. Technol. Lett.*, vol. 30, pp. 38–40, Jul. 2001.

- [77] P. Shiji and C. Filippo, "Design of a CMOS on-chip slot antenna with extremely flat cavity at 140 GHz," *IEEE Antennas Wireless Propag. Lett.*, vol. 10, pp. 827-830, Jul. 2011.
- [78] B. Adel et al., "Back radiation reduction of 60 GHz CMOS slot antenna-on-chip (AoC) using artificial dielectric layer (ADL) for area reuse," *Radio Science Meeting Joint AP-S Symp.*, Memphis, TN, July 6-11, 2014.
- [79] Guo Qing Luo, Lin Qi Wu, and Xiao Hong Zhang, "An AMC Backed Folded Dipole Slot Antenna Based on CMOS Process," *International Journal Antennas Propag.*, vol. 2013, Article ID 351956, 4 pages, 2013.
- [80] J. Coonrod, B. Rautio, "Comparing Microstrip and CPW Performance," *Microwave Journal*, Jul. 2012.
- [81] D. Titz, F. B. Abdeljelil, S. Jan, F. Ferrero, C. Luxery, P. Brachet and G. Jacquemod, "Design and characterization of CMOS on-chip antennas for 60 GHz communications," *Radio-engineering Journal*, vol. 21, no. 1, pp. 324-331, Apr. 2012.
- [82] D. Hou, Y. Z. Xiong, W. L. Goh, S. Hu, W. Hong and M. Madhian, "130-GHz On-Chip Meander Slot Antennas With Stacked Dielectric Resonators in Standard CMOS Technology," *IEEE Trans. Antennas Propag.*, vol. 60, no. 9, pp. 4102-4109, Sept. 2012.
- [83] R. Kranenburg, S. A. Long and J. T. Williams, "Coplanar Waveguide Excitation of Dielectric- Resonator Antennas," *IEEE Trans. Antennas Propag.*, vol. 39, no. 1, pp. 119-122, Jan. 1991.
- [84] T. H. Chang and J. F. Kiang, "Dual-band split dielectric resonator antenna," *IEEE Trans. Antennas Propag.*, vol. 55, no. 11, pp. 3155-3162, Nov. 2007.
- [85] A. Buerkle, K. Sarabandi and H. Mosallaei, "Compact slot and dielectric resonator antenna with dual-resonance, broadband characteristics," *IEEE Trans. Antennas Propag.*, vol. 53, no. 3, pp. 1020-1027, Mar. 2005.

APPENDIX A – LIST OF PUBLICATIONS

Journal Paper Publications:

- [1] P. Burasa, N. G. Constantin, and K. Wu, “High-Efficiency Wideband Rectifier for Single-Chip Batteryless Active Millimeter-Wave Identification (MMID) Tag in 65-nm Bulk CMOS Technology,” *IEEE Trans. Microw. Theory Techn.*, vol. 62, no. 4, pp. 1005-1011, Apr. 2014.
- [2] P. Burasa, N. G. Constantin, and K. Wu, “Low-Power Injection-Locked Zero-IF Self-Oscillating Mixer for High Gbit/s Data-Rate Battery-Free Active μ RFID Tag at Millimeter-Wave Frequencies in 65-nm CMOS,” *IEEE Trans. Microw. Theory Techn.*, vol. 64, no. 4, pp. 1055-1065, Apr. 2016.
- [3] P. Burasa, T. Djerafi, N. G. Constantin, and K. Wu, “High-Data-Rate Single-Chip Battery-Free Active Millimeter-Wave Identification Tag in 65-nm CMOS Technology,” *IEEE Trans. Microw. Theory Techn.*, vol. 64, no. 7, pp. 2294-2303, Jul. 2016.
- [4] P. Burasa, T. Djerafi, N. G. Constantin, and K. Wu, “On-Chip Dual-Band Rectangular Slot Antenna for Single-Die Millimeter-Wave Identification Tag in Standard CMOS Technology,” *IEEE Trans. Antennas Propag.*, Oct. 2016.(Submitted).

Conference Publications:

- [5] P. Burasa, N. G. Constantin, and K. Wu, “Low-Power Injection-Locked Zero-IF Self-Oscillating Mixer for Self-Powered Millimeter-Wave Identification (MMID) Active Tag in 65-nm CMOS,” *IEEE Radio Freq. Integr. Circuits (RFIC) Symp.*, Phoenix, AZ, USA, May 17-19, 2015, pp. 259-262.
- [6] K. Wu, P. Burasa, T. Djerafi, and N. G. Constantin, “Millimeter-Wave Identification for Future Sensing, Tracking, Positioning, and Communicating Systems,” *IEEE Global Symp. Millimeter Waves (GSMM) & ESA Workshop*, Espoo, Finland, June 6-8, 2016.

Workshops:

- [7] K. Wu, P. Burasa, S. Hemour, and S. Ladan, “Millimeter-Wave Power Harvesting From CMOS Circuits to Diode Platforms,” *IEEE Radio Frequency Integrated Circuits (RFIC) Workshop*, San Francisco, CA, USA, May 22-27, 2016.